SMART GRID OPERATIONAL STRATEGIES FOR POWER DISTEIBUTION SYSTEMS WITH LARGE PENETRATION OF DISTRIBUTED ENERGY RESOURCES

by

AHMADREZA MALEKPOUR

B.S., Shiraz University, 2002
M.S., Shiraz University, 2006

AN ABSTRACT OF A DISSERTATION

submitted in partial fulfillment of the requirements for the degree

DOCTOR OF PHILOSOPHY

Department of Electrical and Computer Engineering
College of Engineering

KANSAS STATE UNIVERSITY
Manhattan, Kansas

2016

Abstract

Power distribution systems are transitioning from traditional centralized-control distribution grids to the modern distribution grids that are more customer-interactive and include microgrids (MGs) as well as various unpredictable and multi-scale distributed energy resources (DERs). However, power fueled by renewable DERs such as wind and solar is highly variable and high penetration of renewable DERs in distribution system may potentially degrade the grid reliability and power quality. Moreover, the growth of generation sources will increase the number of variables and cause scalability concerns for distribution system operators (DSOs) in handling optimization problems. Further, with development of MGs, DSO and MG may have different owners and schedule renewable and non-renewable DERs based on their own economic rules and policies while secure and economic operation of the entire system is necessary. The widespread integration of wind and solar and deployment of MGs in distribution system make the task of distribution system operation management quite challenging especially from the viewpoint of variability, scalability, and multi-authority operation management. This research develops unique models and methodologies to overcome such issues and make distribution grid operation, optimization and control more robust against renewable intermittency, intractability, and operation complexity.

The objectives of this research are as follows: 1) to develop a three-phase unbalanced large-scale distribution system to serve as a benchmark for studying challenges related to integration of DERs, such as scalability concerns in optimization problems, incremental power losses, voltage rise, voltage fluctuations, volt/var control, and operation management; 2) to develop a novel hierarchical and multilevel decentralized optimization for power loss minimization via optimal reactive power provisioning of rooftop PVs which addresses the

scalability issues with widespread DER integration in large-scale networks; 3) to develop a dynamic operational scheme for residential PV smart inverters to mitigate the fluctuations from rooftop PV integration under all-weather-condition (fully sunny, overcast and transient cloudy days) while increasing network efficiency in terms of power losses, and number of load tap changer (LTC) operation; 4) to develop a stochastic energy management model for multi-authority distribution system operating under uncertainty from load and wind generation, which is able to precisely account interactions between DSO and MGs.

SMART GRID OPERATIONAL STRATEGIES FOR POWER DISTEIBUTION SYSTEMS WITH LARGE PENETRATION OF DISTRIBUTED ENERGY RESOURCES

by

AHMADREZA MALEKPOUR

B.S., Shiraz University, 2002
M.S., Shiraz University, 2006

AN ABSTRACT OF A DISSERTATION

submitted in partial fulfillment of the requirements for the degree

DOCTOR OF PHILOSOPHY

Department of Electrical and Computer Engineering
College of Engineering

KANSAS STATE UNIVERSITY
Manhattan, Kansas

2016

Approved by:

Major Professor
Dr. Anil ahwa

Copyright

Abstract

Power distribution systems are transitioning from traditional centralized-control distribution grids to the modern distribution grids that are more customer-interactive and include microgrids (MGs) as well as various unpredictable and multi-scale distributed energy resources (DERs). However, power fueled by renewable DERs such as wind and solar is highly variable and high penetration of renewable DERs in distribution system may potentially degrade the grid reliability and power quality. Moreover, the growth of generation sources will increase the number of variables and cause scalability concerns for distribution system operators (DSOs) in handling optimization problems. Further, with development of MGs, DSO and MG may have different owners and schedule renewable and non-renewable DERs based on their own economic rules and policies while secure and economic operation of the entire system is necessary. The widespread integration of wind and solar and deployment of MGs in distribution system make the task of distribution system operation management quite challenging especially from the viewpoint of variability, scalability, and multi-authority operation management. This research develops unique models and methodologies to overcome such issues and make distribution grid operation, optimization and control more robust against renewable intermittency, intractability, and operation complexity.

The objectives of this research are as follows: 1) to develop a three-phase unbalanced large-scale distribution system to serve as a benchmark for studying challenges related to integration of DERs, such as scalability concerns in optimization problems, incremental power losses, voltage rise, voltage fluctuations, volt/var control, and operation management; 2) to develop a novel hierarchical and multilevel decentralized optimization for power loss minimization via optimal reactive power provisioning of rooftop PVs which addresses the

scalability issues with widespread DER integration in large-scale networks; 3) to develop a dynamic operational scheme for residential PV smart inverters to mitigate the fluctuations from rooftop PV integration under all-weather-condition (fully sunny, overcast and transient cloudy days) while increasing network efficiency in terms of power losses, and number of load tap changer (LTC) operation; 4) to develop a stochastic energy management model for multi-authority distribution system operating under uncertainty from load and wind generation, which is able to precisely account interactions between DSO and MGs.

Table of Contents

List of Figures

List of Tables

Acknowledgements

First and most, I thank my advisor, Dr. Anil Pahwa, for his guidance and advice, and for patience and endless encouragement throughout my doctoral research. It has been a great privilege for me to work under his supervision. He was not only my academic advisor, but one of the best and kindest persons I have ever seen in my life. I thank my committee members, Dr. Noel Schulz, Dr. Bala Natarajan, Dr. Sanjoy Das, and Dr. Scott DeLoach, for their constructive comments and insightful questions. I've loved every moment; I could not have wished for a better experience.

I am grateful to those who worked beside me on a multi-year project, including Mohammad Faqiry, Shafiul Alam, and especially Denise Case.

I owe a deep debt of gratitude to my family who encouraged and supported me throughout this journey, from my mother to my wonderful sisters and brothers and their families. I could not have done it without you. Thank you!

Dedication

I would like to dedicate this dissertation to my wife, Elahe. Without her love, and support, the lifelong journey into enlightenment would yield little meaning. She brings immeasurable happiness to all the days of my life. I will be forever grateful for her help, understanding, and patience.

Chapter 1 - Introduction

1.1 From Today's to Future Power Grids

Today's electric power grids evolved from local grids that grew and became interconnected over decades for economic and reliability purposes. Following the first power grid installation in Massachusetts in 1886 [1], alternating current (AC) power grids became very large, mature and highly interconnected in developed countries by the 1960s. In this large grid, the power stations were typically located close to fossil fuel reserves. Much of these fossil-fired power stations were facilities which contributed high levels of pollution and were by necessity located far from cities. High voltage transmission lines were installed to carry power from large power stations to major load centers and then distribute power to commercial, industrial and residential areas via lower voltage distribution lines as shown in Figure 1.1. The number of power stations increased in response to load growth from the 1970s through the 1990s. In some areas, however, change was abrupt and the gap between demand and supply, especially at peak load hours, resulted in power outages and/or poor power quality and reliability. Since that time, power grids have matured and dependence on electricity for heating, cooling, communication, banking, lighting, transportation, entertainment, and industry has continued to grow; consumers today are demanding higher levels of reliability and power quality.

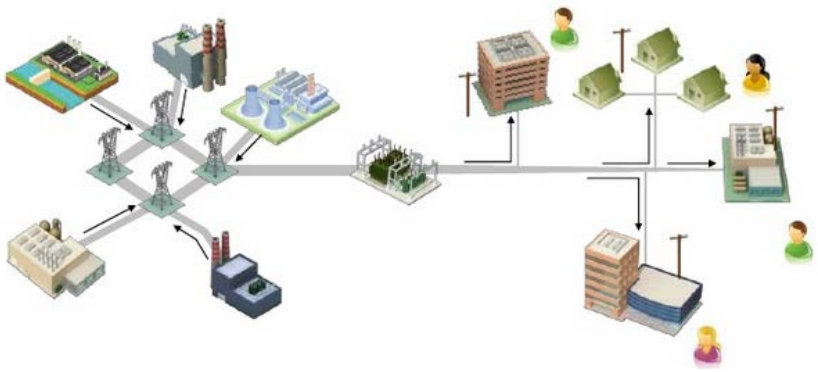

Figure 1.1 Traditional electric grid [2]

Extensive scientific research has been conducted to resolve limitations and reduce operational costs of the electrical grid. With development in technology, the concept of smart grid has emerged which refers to the use of advanced sensing, communication, and cyber technologies and improved algorithms to increase the efficiency and reliability of the electric grid. The smart grid represents a transition from outdated, centralized, producer-controlled grid to one that is more customer-interactive and incorporates smart meters, electric vehicles, smart appliances, and renewable energy resources as shown in Figure 1.2. To this end, one major focus is replacing carbon-intensive energy sources with renewable energy resources, leading to increased use of green sources such as solar and wind power.

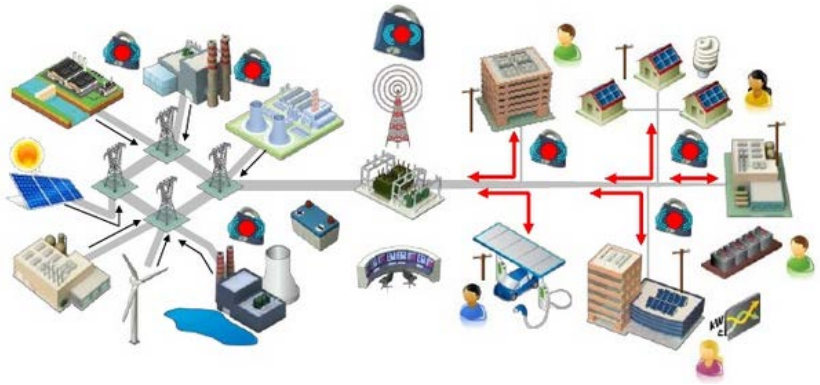

Figure 1.2 Future electric grids [2]

Solar power is an emerging form of energy because it is readily available and environmentally friendly. Rooftop solar generation is expected to reach significant market share due to downward trend in solar module prices and state or federal subsidy programs to promote the use of renewables. According to the International Energy Agency (IEA) solar photovoltaic (PV) roadmap, PV could reach 11% of global electricity production and contribute to reduction of 2.3 gigatonnes carbon dioxide (CO2) emissions per year by 2050 [3].

Technology improvements and decreased prices of solar panels have caused increased interest from utilities and end users regarding PV generation. Several projects in the United States are attempting to identify new ways to increase the penetration of solar generation in distribution systems [4] , [5].

However, many utilities have faced issues related to maintaining proper voltage because the current system cannot handle large penetration of solar generation. As shown in Figure 1.3 [6], rapid irradiance changes on a partly cloudy day causes severe fluctuations in PV power output.

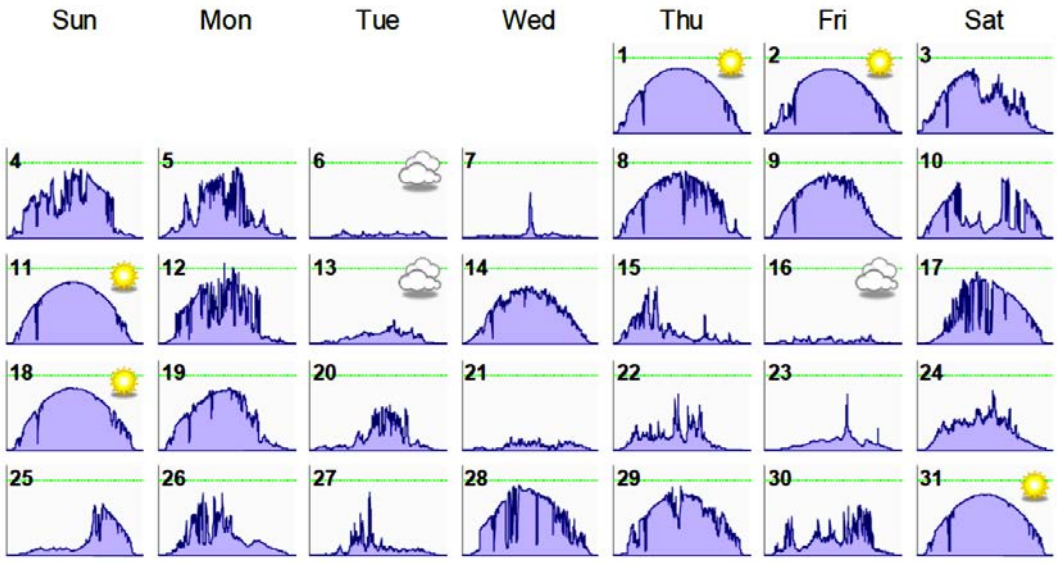

Figure 1.3 PV variability [6]

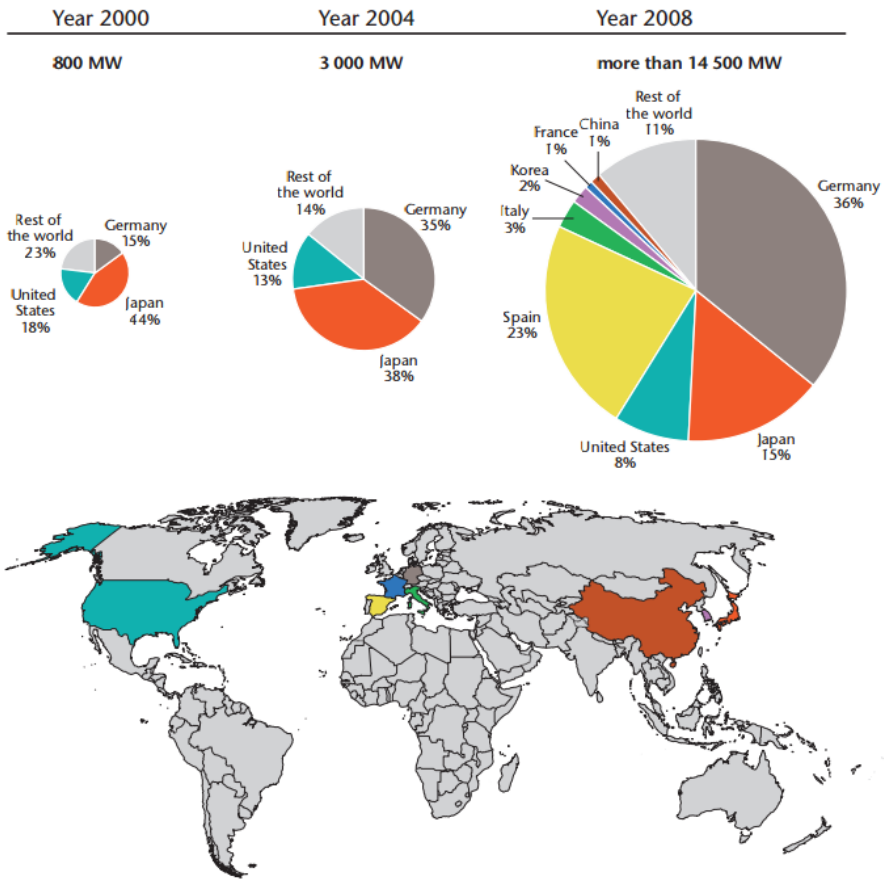

Figure 1.4 Solar PV installed capacities in leading countries [3]

Driven by advances in technology and mass production, wind power is becoming affordable option for energy generation. Governments in many regions offer tax incentives to encourage wind-energy development and make wind energy competitive with energy from fossil-fired power plants leading to a dramatic increase in investments in wind power and wind-turbine technology. The IEA wind roadmap projects that 18% of global electricity will come from wind power by 2050, thereby reducing 4.8 gigatonnes of CO2 per year [7].

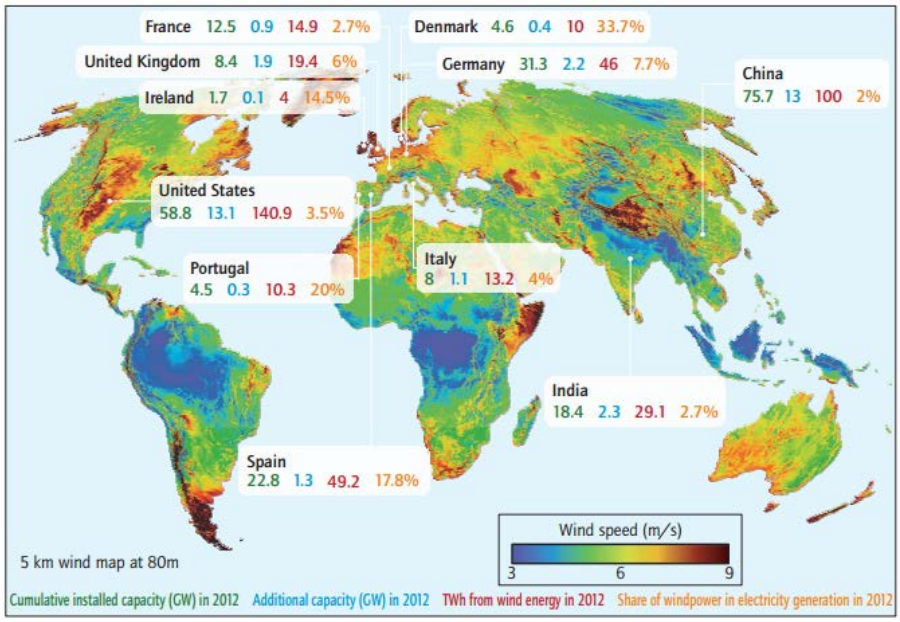

Figure 1.5 Global wind map, installed capacity, and production for lead countries [7]

Renewable energy sources such as wind and solar, however, are highly variable and require sophisticated control systems to facilitate their integration into power grids. Since the variability of renewable sources could decrease the grid reliability, the industry has a great need for new technologies and control strategies to achieve maximum benefits from the integration of intermittent renewable energy sources.

This motivates us to incorporate a class of advanced technology and new methodologies to address the challenging variability of renewables, and facilitate a cost-effective replacement for traditional grid infrastructure while providing equal or improved levels of power quality and reliability.

1.2 Research Motivation and Problem Statement

The electric power grid is transitioning from a system that relies on centralized and polluting sources of power to a sustainable, flexible network that incorporates massive distributed energy resources (DER), such as small distributed generators (DG), storage devices, combined heat and power plants, wind generators (WGs) and rooftop solar PVs. The new paradigm places DERs near load centers in distribution systems to provide consumers with a diverse energy mix, involve customers in energy management, and

increase the penetration level of renewables. This brings about the concept of microgrid (MG) [8], in which clusters of DGs, loads, and the distribution grid infrastructure operate as a single entity. In order to provide a reliable, cost-effective foundation for future modern grids, MGs can be designed to sell excess power back to the grid in grid-connected mode or operate autonomously in islanded mode.

However, one of the barriers for these advances is that the existing power distribution systems were not designed to accommodate high levels of DER penetration while sustaining high levels of reliability and/or power quality. Some major obstacles for DER integration into distribution system are summarized as follows:

- Power distribution systems are composed of unbalanced three-phase and single-phase feeders and laterals [9]. Although, the distribution systems are unbalanced, this level of unbalance typically has been small and thus analysis considering balanced system has yielded satisfactory results. In fact, a majority of DER integration studies have used a balanced single-phase network model of the primary distribution system. However, future distribution systems will deploy numerous smart devices, such as smart meters, smart inverters, rooftop solar PVs, battery storage, and electric vehicles into homes located at the secondary level. This deployment will require large-scale network modeling, an increased number of variables, and subsequent scalability concerns in solving optimization problems. In addition, deployment of single-phase DERs could worsen the imbalance and increase power losses in power distribution system. If DERs come to play a significant role in the future, power distribution system optimization studies and modeling using the current single phase network models and optimization technique fail to provide fast and accurate solutions.
- Certain types of DER, such as wind and solar generation, are variable and uncertain from hourly and sub-hourly to second-by-second time frames. In order to fully realize the value

of DERs in all time frames and weather conditions, various modes of operation and variability/uncertainty modeling should be taken into account while leveraging the real and reactive power capabilities of the emerging smart inverters. For example, a high level of PV penetration imposes voltage fluctuation issues on electricity networks due to solar variability, especially on intermittent cloudy days. The output power of PV tends to follow solar irradiance almost instantaneously, and fast moving clouds could cause rapid variation in power and voltage in low voltage distribution systems. Thus, ad-hoc integration of renewable DERs with active/reactive power injection capability may increase risks associated with design and operation and result in voltage violation for a phase or three phase voltage imbalance at a bus, thereby jeopardizing expected benefits from renewables.

- Traditionally, a single decision maker integrates and solves optimization problems in pursuit of the entire system objective [10]. In such a centralized decision-making environment, problem information, cost parameters, objectives, and decision authority are given to the distribution system operator (DSO). However, with MG development, the DSO and MGs operate independently to optimize their objectives. In addition, they have access only to local information, which they partially share with each other. Furthermore, it is well known that the power outputs from closely located DERs, such as WGs, can be highly correlated and such a correlation may have a very significant impact on power flow and subsequently the grid operation. Therefore, energy management in future distribution systems is an emerging challenge considering multi-authority energy management models, information privacy, and multiple DER scheduling under uncertainty and correlations among WGs.

Although high levels of DER integration will also cause potential protection issues due to reduction in reach of relay, potential change in coordination of fuse, circuit breaker and recloser [11],

overloading of feeders and substation transformer (thermal issues), and backflow of power to the transmission system [12], these issues are outside the scope of this research.

This research specifically attempted to address the above challenges by implementing innovative approaches for distribution system operation, optimization and control. The research focused on studies related to integration of unpredictable and multi-scale DERs. The following applications were include 1) power loss minimization, volt/var control, and voltage fluctuation control studies with consideration of single–phase DGs, and rooftop PV integration, and 2) multi-MG energy management under wind uncertainty. Previous attempts to resolve DER integration challenges in the context of applications of this research are discussed in the following section.

1.3 Literature Review

This section is divided into four sub-sections to cover the previous works related to the topic presented in this dissertation.

1.3.1 Loss minimization with DER Integration

One of the fundamental operating requirements of a power distribution system is volt/var control, with the primary purpose of improving voltage profiles along the feeder and reducing real power losses under all loading conditions. Considering growth of DG in the United States [13] and expected global increase in wind and solar integration [3] and [7], well-coordinated control of DER will significantly mitigate the issues and provide volt/var support.

According to the Energy Information Administration (EIA), electricity transmission and distribution losses average approximately 7% in the United States (e.g., 262.72 billion kilowatt-hours in 2012) [14], [15]. Approximately 4% of losses are incurred at medium- and low-voltage distribution systems, representing billions of dollars wasted annually. Therefore, the study of power losses is crucial for DSOs.

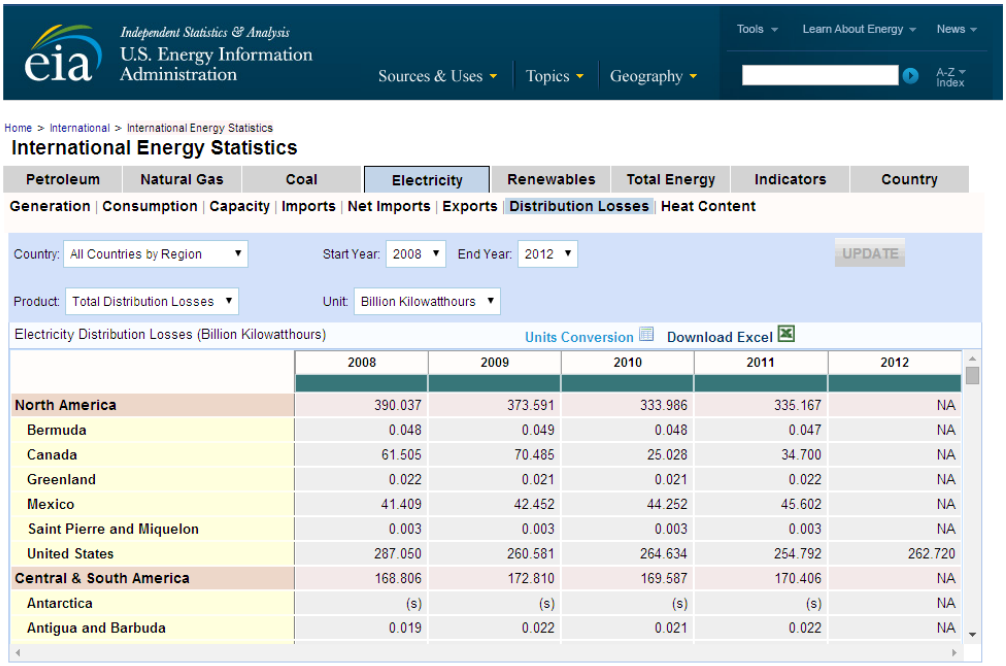

	2008	2009	2010	2011	2012
North America	390.037	373.591	333.986	335.167	NA
Bermuda	0.048	0.049	0.048	0.047	NA
Canada	61.505	70.485	25.028	34.700	NA
Greenland	0.022	0.021	0.021	0.022	NA
Mexico	41.409	42.452	44.252	45.602	NA
Saint Pierre and Miquelon	0.003	0.003	0.003	0.003	NA
United States	287.050	260.581	264.634	254.792	262.720
Central & South America	168.806	172.810	169.587	170.406	NA
Antarctica	(s)	(s)	(s)	(s)	NA
Antigua and Barbuda	0.019	0.022	0.021	0.022	NA

Figure 1.6 Average electricity transmission and distribution losses in the United States.

Distribution systems are lagging behind generation and transmission systems in terms of availability of real-time information and level of automation. As a result, most distribution system operation and planning methods have relied on heuristics and archived information. However, with growing interest in smart grid, utilities are addressing this issue in order to fill the gap via deployment of advanced metering infrastructure (AMI), integrated communications infrastructure, meter data management, and automation in distribution systems [16], [17], [18].

Literature review shows opportunities for power loss reduction via PV integration into distribution systems depending on penetration level and reactive power control strategy [19], [20], [21], [22]. In the literature, DER control schemes are classified into three categories: centralized [23], [24], [25], [26], [27], [28], distributed (or decentralized) [29], [30], [31], [32], and local [33], [34], [35], [36], [37], [38], [39], [40], [41]. Centralized and decentralized approaches are based on optimal power flow (OPF) techniques, while local approaches are based primarily on local DG active and/or reactive power control. In [24], mixed integer linear programming was used to formulate volt/var optimization including transformer load tap changers (LTC), switchable capacitors, and reactive power of DGs. In [25], the LTC and step voltage

regulators (SVRs) were used to find optimal voltage in distribution systems based on centralized control. Optimal management of reactive power by controlling inverters of PV units was proposed in [26]. Probabilistic volt/var control was studied in [27] considering uncertainty associated with renewable DGs. In [28], a comprehensive centralized approach was presented for voltage constraint management in active distribution grid. In [29], a distributed automatic voltage control was introduced for voltage rise mitigation due to DG integration into distribution systems. Decentralized control of DG for voltage and thermal constraint management was presented in [30]. Combined local and remote voltage and reactive power control in the presence of induction DG machines was presented in [31]. In [32], an automatic distributed voltage control algorithm based on sensitivity approach was used to control node voltages that regulate reactive power injected by DGs.

A majority of researchers have used a balanced network model to solve the volt/var control problem [23]-[32]. However, power distribution systems are unbalanced in nature composed of unbalanced three phase and single phase feeders and laterals serving customers through unbalanced line configurations with different phase loading levels [9]. In this regard, [42] proposed a three phase OPF to determine the LTC and capacitor setting in power distribution system. In [43], a three phase OPF to mitigate the voltage unbalance is developed. In [44], three-phase OPF is introduced to solve the volt/var control problem where the goal was to minimize reactive power of DG units while satisfying operational constraints.

Several approaches have been proposed to develop distributed algorithms for OPF and/or controlling DERs. The available literature includes node to node message passing among neighboring PVs [33], alternating direction multiplier method (ADMM) for DER control in small-scale single-phase or primary distribution networks [34], [35], hierarchical optimization for DER control without coordination formulation between the levels [36], [37], master-slave control for islanded operation of microgrids [38], and two-level leader/follower control of plug-in electric vehicles [39], [40]. These

optimization problems have been solved under different yet simple assumptions such as not including primary and/or secondary level networks, considering balanced load with conventional DG units operating at unity power factor. Recently, authors of [41] presented a centralized/local OPF for control of PV inverters in a small-scale three-phase semi-unbalanced secondary network. However, reactive power consumption by loads was not included, and the simulations were done under the assumption that all households have the same PV generation capacity.

1.3.2 Reactive Power and Voltage Control with Rooftop PVs Integration

Large penetration of PV systems present challenging power quality issues, such as incremental power losses, voltage violation, and voltage fluctuation for distribution system operators. Worldwide interest in rooftop PV installation has created the need for additional network regulations in order to achieve safe and reliable operation of low voltage (LV) grids. Although previous version of IEEE Std. 1547 [45] prohibited reactive power support by DG in LV grids, a recently published amendment [46] and standards issued in Germany [47] and Italy [48] specify DG reactive power control strategies in order to maintain power quality levels or provide ancillary services for the LV network.

Several PV inverter reactive power control methods have been proposed, including $cos\varphi(P)$, $Q(V)$, and $Q(V)/P(V)$ strategies [49], [50]. In the $cos\varphi(P)$ strategy, inverter feed-in power is monitored; once the power exceeds a predetermined limit, the PV inverter starts to absorb reactive power at a constant rate. Load tap-changer (LTC) control and $cos\varphi(P)$ strategies for PV inverters were used in [20] to limit voltage rise. Location-dependent $cos\varphi(P)$ characteristics were proposed in [49] and [51] to mitigate voltage rise and reduce power losses. In the $Q(V)$ strategy, a droop characteristic based on inverter bus voltage was used to calculate PV inverter reactive power. Application of the $Q(V)$ control strategy was described in [49] and [52] for overvoltage prevention control of PV generators in microgrids. The $Q(V)/P(V)$ strategy was proposed to mitigate voltage rise when reactive power control alone is

inefficient. The $Q(V)/P(V)$ method combines active power curtailment with the $Q(V)$ method. Referring to the literature, voltage rise caused by reversed power during low demand and high PV generation is known as primary network constraints that limit PV penetration in distribution systems [53]. An online overvoltage prevention control strategy based on active power limit prediction was proposed in [54]. However, the concept is suitable only for microgrids since identification of the system Thevenin equivalent is the foundation of the algorithm. Reference [55] discussed use of droop-based active power curtailment for overvoltage prevention in radial LV feeders, while $Q(V)$ and $Q(V)/P(V)$ strategies and autonomous LTC operation were used in [50] to assess cost-benefit analysis of local control strategies.

Detrimental effects associated with high levels of PV integration are not limited to voltage rise. Power generation of rooftop PV can have large fluctuations due to rapid variations in solar irradiance on intermittent cloudy days. For example, cloud cover can rapidly reduce solar power generation, increase flow of power from the grid, and potentially cause voltage drop problems. Recently, PV system studies during intermittent cloud movement have gained increasing attention. In [56], Distribution Static Synchronous Compensator (DSTATCOM) was used to damp impacts associated with residential PV power fluctuation on the LTC operation. Reference [57] presented inverter reactive power control for rooftop PV integration that requires detailed historical load demand and PV output profile for each household. Moreover, inverter night-mode operation for DSTATCOM was assumed. Although night-mode operation is under research and development for solar farms [58], its suitability for house-level PV has not yet been demonstrated. Studies in [59] and [60] proposed storage batteries to suppress the effect of large penetration of PV on power transients. However, cost-effective battery technologies able to compensate for unexpected PV power fluctuations are still under development [61].

1.3.3 Networked-MGs Energy Management with Correlated Wind Generators

Several approaches have been proposed for single MG energy management and/or DG control without considering interaction with the DSO. Available literature includes central controller for profit

maximization with multiple DGs [62], optimal dispatch of DGs for energy management [63], [64], combined network reconfiguration and DG dispatch schemes [65], renewable DG and plug-in electric vehicle (PEV) scheduling [66], and generation scheduling and demand side management based on multi-agent system (MAS) [67].

Although these approaches have been proposed for single DSO/MG energy management, strategies for coordination of MGs and DSO are limited. For example, MAS-based generation scheduling and supply–demand mismatch control of multiple MGs are proposed in [68], [69]. The study in [70] proposed a local and suboptimal energy consumption scheduling for connected MGs in which the network operator performs scheduling scheme for several MGs with known average demand while considering demand of neighboring areas as a random variable. Decentralized energy management for networked MGs was presented in [71] and uncertainties from renewables and load demand were modeled by scenarios generated from Monte Carlo simulations (MCS), followed by a scenario reduction method. The study in [72] presented a leader-follower strategy for energy management of multi-MGs via bi-level programming, in which the upper level is modeled as a gas-fired generator and an energy service provider manages the DG generation mix of several MGs in the lower level. This approach converts the bi-level model to an equivalent one-level problem, thereby avoiding consideration of interactions between the two decision-making levels. In [73], interaction of MGs with a distribution system was successfully modeled via implementation of a system of systems framework. However, uncertainties from renewable generators and load demand were not considered. In [74], a Markov decision process was used to minimize the generation cost of MGs; however, centralized information shared among MGs was used to generate decentralized control signals for coordination of multi-MGs.

Despite deterministic approaches that have been proposed to solve multi-MG energy management in the presence of DGs, no technical literature is available to tackle the problem under correlated input uncertainties such as those created by the intermittent nature of renewable DGs. MCS is an option for

uncertainty analysis, but it can be computationally intensive, especially in problems in which the main optimization algorithm is solved based on distributed methods.

1.4 Contributions of This Dissertation

This research is focused on providing novel strategies to facilitate the transition from the current power distribution grids to smart power distribution grids via integration of wind and solar power, operation of multiple self-governed MG systems, improving grid efficiency and operational costs, and reducing power losses. The major contributions of this dissertation are summarized as follows:

1.4.1 Addressing Scalability Issues with DER Integration in Large-Scale Networks

- Development of a three-phase unbalanced large-scale distribution system in which a three-layered architecture including primary feeders, lateral feeders, and secondary feeders are modeled from substation transformer all the way down to the house level. The developed system serves as an open source benchmark test feeder for researchers and engineers in the electric power community to study challenges related to integration of DERs, such as scalability concerns in optimization problems, incremental power losses, voltage rise, voltage fluctuations, volt/var control, and operation management.
- Development of a novel hierarchical and multilevel decentralized OPF for power loss minimization via optimal reactive power scheduling of rooftop PVs with consideration of operational constraints in primary and secondary distribution network. Results from the developed benchmark demonstrated 37.44% and 23.74% reduction in power losses compared to the fixed power factor and local control methods.
- Development of a sequential coordination strategy to ensure convergence of the proposed distributed loss minimization scheme in large-scale networks. The centralized approach

took several hours to solve the large-scale system, but proposed approach with sequential coordination strategy solved the loss minimization problem in 355 seconds (about 6 min).

- Development of a parallelized coordination strategy which significantly reduced the computational complexity of the developed formulation and made it favorable in large-scale networks. Significant reduction in execution time (118 seconds) was demonstrated with slight accuracy loss compared to the sequential approach (max absolute error 3.6%).

These contributions are discussed in detail in Chapters 2 and 3, and appeared in the following articles:

[75] A. R. Malekpour, A. Pahwa, “Radial Test Feeder Including Primary and Secondary Distribution Network,” North American Power Symposium (NAPS), North Carolina, Charlotte, October 2015.

[76] A. Pahwa, S. A. DeLoach, B. Natarajan, S. Das, A. R. Malekpour, Md. Shafiul Alam, and Denise M. Case, “Goal-Based Holonic Multiagent System for Operation of Power Distribution Systems,” IEEE Transactions on Smart Grid, 2015.

[77] A. R. Malekpour, A. Pahwa, “Distributed Volt/Var Control in Unbalanced Distribution Systems with Distributed Generations”, IEEE Symp. on Computational Intelligence Applications in Smart Grid, Orlando, 2014.

[78] A. R. Malekpour, A. Pahwa, B. Natarajan, “Hierarchical Architecture for Integration of Rooftop PV in Smart Distribution Systems” IEEE Transactions on Smart Grid, 2016.

1.4.2 Improving Efficiency and Damping Variability in Smart Distribution Systems with High Level of Rooftop PV Penetration

- Proposal of three states of operation (normal, fluctuating and contingency states) for PV inverters based on solar irradiance variation and voltage measurement at the interconnection point.
- Specify operational goals and derive required reactive power to meet the goals for each state. In the normal state, the scheme is designed to provide loss reduction support while continuing to support load demand when irradiance changes slowly. In the fluctuating state, reactive power is modulated in order to mitigate voltage fluctuations caused by transient cloud movement. The control offers reactive power support to mitigate voltage violation defined for the contingency state.
- Introduce a reactive power ramp rate limiter to prevent additional voltage fluctuations due to reactive power variation caused by switching between states.
- Proposal of a coordination strategy to switch control between states and manage interaction between fast PV inverter controllers and slow LTC for voltage regulation.
- Quantify the impact of high penetration of rooftop PV on the developed benchmark test feeder under all-weather-conditions via performance metrics including maximum voltage deviation (MVD) from nominal voltage limits, total power losses, total number of LTC tap operations and bus voltage fluctuation index (VFI).

These contributions are discussed in detail in Chapter 4, and are either under review appeared in the following articles:

[21] A. R. Malekpour, A. Pahwa, “Reactive Power and Voltage Control in Distribution Systems with Photovoltaic Generation” in Proc. 44th North American Power Symposium (NAPS), Urbana-Champaign, September 9-11, 2012.

[19] A. R. Malekpour, A. Pahwa, S. Das, “Inverter-based Var Control in Low Voltage Distribution Systems with Rooftop Solar PV,” in Proc. 45th North American Power Symposium (NAPS), Manhattan, Kansas, Sep., 2013.

[79] A. R. Malekpour, A. Pahwa, “A Dynamic Operational Scheme for Residential PV Smart Inverters,” IEEE Transactions on Smart Grid, 2016.

1.4.3 Networked-MGs Energy Management with Correlated Wind Generators

- Propose a linear approximation model to separate optimization problems in DSO and MGs.
- Propose a distributed and parallel processing method with minimal information interchanged between DSO and MGs. Results demonstrated significant reduction in computational complexity.
- Development of a probabilistic power flow method to handle uncertainties in load and wind generators using the point estimate method (PEM).
- Develop a stochastic energy management model for multi-authority distribution systems operating under uncertainty from load and wind generation that can account for statistical correlations between stochastic inputs while precisely representing interactions between entities.

These contributions are discussed in detail in Chapter 5, and are under review in the following article:

[80] A. R. Malekpour, A. Pahwa, “Stochastic Energy Management in Distribution Systems incorporating Multi-Microgrids and Correlated Wind Generators”, submitted, IEEE Transactions on Power Systems.

1.5 Dissertation Outline

Chapter 2 describes development of the large-scale three-phase unbalanced distribution network test case, considering primary and secondary level distribution systems. Chapter 3 introduces the development of hierarchical optimization and two methods with sequential and parallelized distributed coordination scheme for loss minimization with large penetration of rooftop PV in large-scale networks. The dynamic PV inverter reactive power control scheme is presented in Chapter 4, and the multi-authority energy management model that incorporates multi-MGs under correlated WGs is introduced in Chapter 5. Chapter 6 summarizes the work, and offers conclusions and recommendations for future research.

Chapter 2 - Development of Large-Scale Test Feeder Benchmark

This chapter describes development of a three-phase unbalanced distribution network test case from substation transformer all the way down to the house level in order to leverage integration and coordination of rooftop PV generators. The developed test feeder is applicable for studying challenges of DER integration into distribution systems.

2.1 Background

With a paradigm shift towards smart grids, future power distribution systems will be more complex due to massive deployment of rooftop PVs, battery storage, electric vehicles, and other DER devices at the residential level. This requires analysis with a detailed network model in order to capture benefits from DERs and provide insight into control and management of distribution systems. The Test Feeders Working Group of the IEEE PES Distribution System Analysis Subcommittee has published several test feeders for analysis of unbalanced three-phase radial distribution feeders based on primary distribution network [81]. A test feeder was recently developed that considered primary and secondary networks without an elaborate house level model [82]. However, in order to leverage the integration and coordination of rooftop PV generators, a three-phase unbalanced distribution network test case from substation transformer all the way down to the house level with detailed primary and secondary circuit model in necessary. This chapter describes development of such test feeder that can serve as a benchmark for studying challenges of rooftop PV, house level battery storage [83], and electric vehicles integration [40], [39], such as energy efficiency and power losses analysis, voltage rise prevention [83], voltage fluctuations mitigation [19], [84], volt/var control [27], [21], [85], [25], [26], [77], and optimal operation management of DER [76].

2.2 Network Description and Modeling

The developed radial distribution test feeder including both primary and secondary distribution networks consists of 559 nodes. The nodes are distributed in 1-, 2-, and 3-phase bus locations. The system consists of 559 nodes with 144, 144, 160 homes in phases A, B, and C, respectively.

2.2.1 Three-Phase Primary System Description

The IEEE 37 node test system [81] is used to model three-phase primary feeders. The original IEEE 37 node test feeder is a three-wire delta that operates at a nominal voltage of 4.8 kV with unbalanced loading and underground line segments. A single line diagram of the primary feeder model is shown in Figure 2.1.

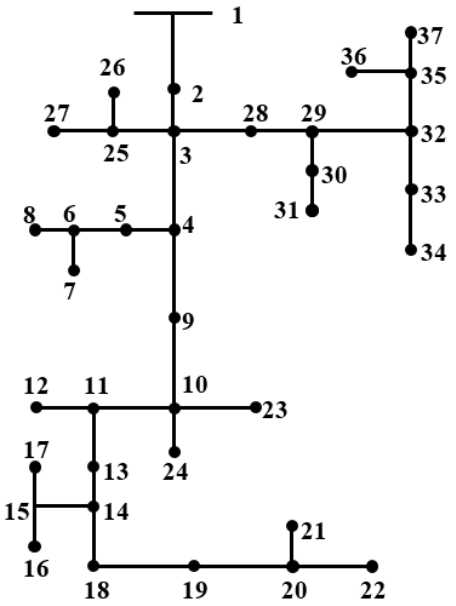

Figure 2.1 Primary distribution system.

In this study, the load is modified to achieve a less unbalanced network; therefore the imbalance in the network typically originates from placement of rooftop PVs, battery storage, and electric vehicles on different phases of the three-phase system. Moreover, part of the load on node 2 is moved to node 24, resulting in increased power losses in the network and making the test feeder a good case study for power

loss minimization and reduction studies. All loads are assumed to be star connected and comprised of residential customers on each feeder. Aggregated load data for the primary feeder are provided in Section 2.3, Table 2.1. Aggregated loads were used to determine the number of homes to place in each phase of the secondary network.

2.2.2 Lateral Feeders Description

Lateral feeders are directly connected to the primary feeder and operate at the same voltage. Based on the specified load type (1-, 2-, or 3-phase load) for a generic node in the primary feeder, 1-, 2-, or 3-phase lateral feeders are tapped from the primary feeder. Lateral feeders typically route power to a community of houses via wooden poles. Figure 2.2 shows a lateral feeder distributing power to seven clusters of houses. In order to simplify the model, all pole to pole lateral feeder lines are wired with #1 overhead conductor, and the distance between poles are set to 250 ft to represent the typical distance between houses in the United States. Overhead lateral conductor data are provided in Section 2.3, Table 2.2.

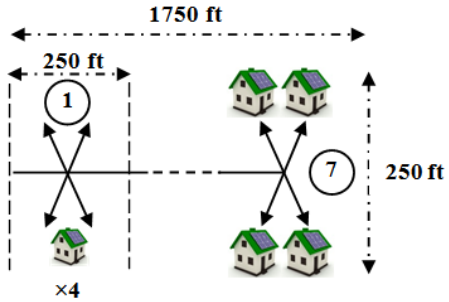

Figure 2.2 Lateral feeder modeling.

2.2.3 Secondary System Description

In the secondary distribution network, short line-segments branch off pole-mounted transformers and distribute energy to a neighborhood. For simplicity and without loss of generality, each pole distributes energy via a pole-mounted transformer to a neighborhood consisting of four homes (i.e., four service drops per transformer are considered as shown in Figure 2.3). The pole-mounted transformer is

modeled as a single-phase center-tapped transformer [86]. Each home is connected to the secondary circuit of a single-phase transformer through triplex overhead drop cable 4/0 AAC [87] of length 90 ft. Detailed data are provided in Section 2.3, Table 2.3.

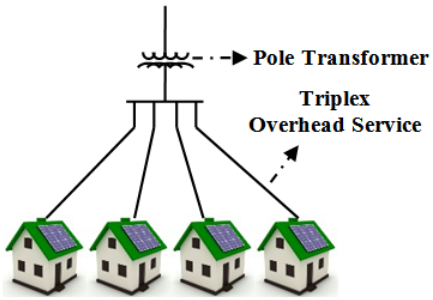

Figure 2.3 Secondary feeder modeling.

2.2.4 Load Model

Home wiring is typically 120 or 240 volts, and in most households, lighting and small appliances are on 15 or 20 amps circuits, while large appliances are on 50 amps circuits [88]. Therefore, at full load, the customer requires 50 × 240 = 12 kW. However, not all customers simultaneously run all electrical equipment and most households rarely exceed half the capacity of their service rating. Therefore, n this study, 25 kVA single-phase pole-mounted transformers are considered to serve a group of four homes. Pole-mounted transformer data are provided in Table 2.4. The total number of pole-mounted transformers at each feeder can be calculated based on primary feeder nodal load requirements. For example, bus 31 has 85 kW load (Table 2.1), so the total numbers of pole-mounted transformers on lateral feeders downstream of this bus are 85/25 = 3.4, rounded to four transformers. Figure 2.4 shows a portion of the test feeder in which the extended lateral feeder is modeled via a line branching out of primary feeder node 31 (i.e., from node 38 to 41) and corresponding pole-mounted transformers and clusters of houses (i.e., from node 42 to 46). Conductor data used to extend the primary network is presented in Section 2.3. Phase impedance and admittance matrices corresponding to feeder laterals, triplex overhead drop cable, pole-mounted transformers, and test feeder line segment data are provided in the Appendix A.

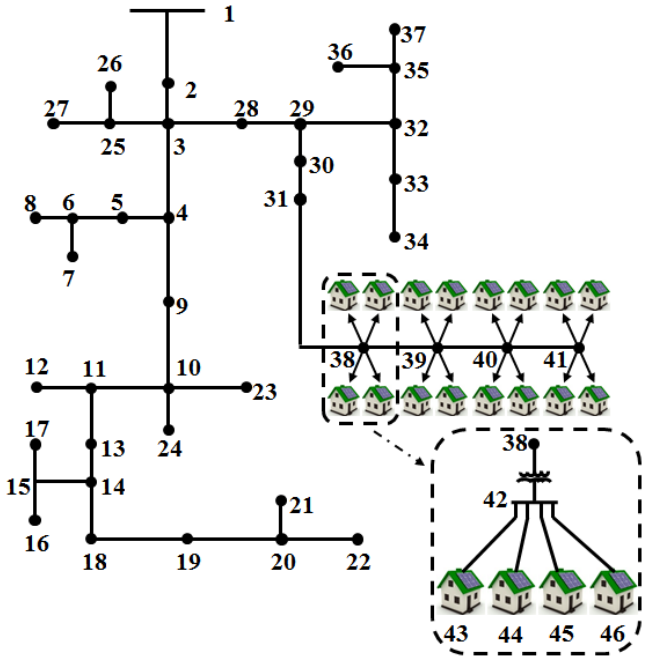

Figure 2.4 Test feeder with primary feeders, lateral feeders and secondary network.

2.3 System Data

This section presents the complete data to model the test feeder.

Table 2.1 Aggregated primary system load data.

Node	Ph-1	Ph-1	Ph-2	Ph-2	Ph-3	Ph-3
	kW	kVAr	kW	kVAr	kW	kVAr
2	84	44	84	44	84	38
5	0	0	0	0	42	21
6	42	21	0	0	0	0
7	42	21	42	21	42	21
8	42	21	0	0	0	0
9	0	0	0	0	85	40
12	0	0	0	0	42	21
13	85	40	0	0	0	0
14	0	0	0	0	42	21
16	0	0	0	0	85	40
17	0	0	42	21	0	0

18	140	70	0	0	0	0
19	126	62	0	0	0	0
21	0	0	85	40	0	0
22	0	0	0	0	42	21
23	0	0	85	40	0	0
24	126	66	126	66	126	57
26	0	0	0	0	85	40
27	8	4	85	40	0	0
28	0	0	0	0	85	40
30	17	8	21	10	0	0
31	85	40	0	0	0	0
34	0	0	42	21	0	0
36	0	0	140	70	21	10
37	0	0	42	21	0	0
Total	797	397	794	394	866	410

Table 2.2 Overhead lateral conductor data.

Type of conductor	GMR	Diam. (inch)	Ampacity (A)	60 Hz (Ohms/mile)	
				resistance	reactance
#1	0.00418	5	200	1.3873	1.6033

Table 2.3 Trilex overhead service drop cable data.

Type of conductor	60 Hz resistance (Ohms/1000 ft)			Inductive reactance (Ohms/1000 ft)
	25◦C	50◦C	75◦C	X1
Triplex	0.4227	0.4645	0.5064	0.0268

Note: Soil (RHO) Resistivity is 100 and resistance in 50◦C is used.

Table 2.4 Pole mounted transformer data.

Type	kVA	Voltage	%R	%X
Single-phase center-tapped	25	4.8kV-120/240V	1.6	2.3

Customer data was extracted from eGauge website [89] which provides real household consumption and PV generation data (open to public) from daily to 1-minute resolution in Excel format. Load reactive power can be defined in proportion to the real load connected to the same bus with a power factor of 0.9 lagging. Typical home consumption and PV generation from 6/4/2015 6:15 pm to 6/5/2015 6:15 pm are shown in Figure 2.5.

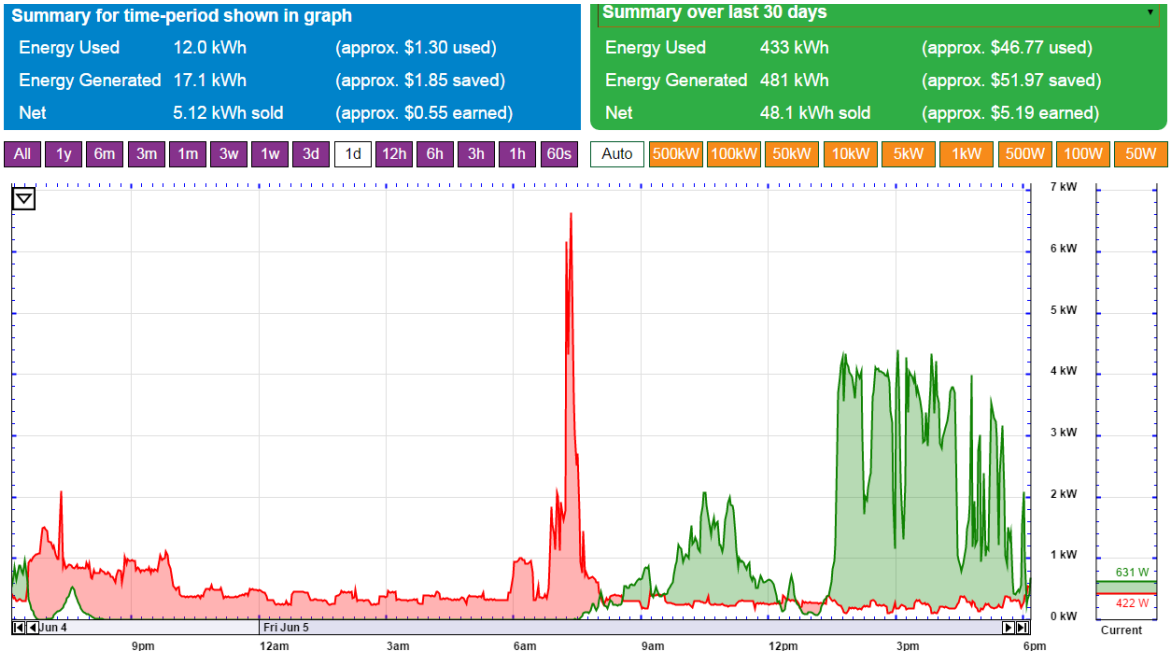

Figure 2.5 Typical home consumption and PV generation.

Various home load data were extracted from the eGauge website and homes were placed in phases A, B, C to maintain the unbalanced characteristic of the system. Distribution of homes in phases A, B, and C and their corresponding locations are listed in the Appendix A where random selection is utilized in order to place a home at a specific node.

PV generation in second-by-second resolution is obtained from NREL data measured in Hawaii [90]. PV-enabled homes are selected randomly for each phase with 50% having rooftop PV. PV generation size at each home is also randomly calculated based on roulette wheel selection with PV size

to peak load ratio (ρ) and a probability distribution function presented in Table 2.5. However, the proposed methodology is applicable to any other method for PV size selection.

Table 2.5 PV size to peak load ratio (ρ) and probability distribution.

ρ	0.25	0.5	0.75	1	1.5	2
Probability	0.09	0.28	0.28	0.28	0.05	0.02

2.4 Summary

In this chapter, a three-phase unbalanced test case was developed with consideration of primary and secondary level distribution systems. Detailed primary feeders, lateral feeders, and secondary feeders were described in order to build a network consisting of 559 nodes. Researchers can use the developed benchmark test system for analysis and resolve issues associated with integration of rooftop PVs and DER devices in existing unbalanced networks, such as incremental power losses, voltage violations, voltage fluctuations, volt/var control and other power quality concerns.

Chapter 3 - Hierarchical Architecture for Integration of DER in Smart Distribution Systems

This chapter initially provides the background and formulation for centralized OPF for loss minimization in distribution systems, including DERs, followed by description of the development of a hierarchical and multilevel decentralized power loss minimization scheme by leveraging the reactive power capability of DERs in the large-scale unbalanced distribution system developed in Chapter 2. The aim is to find optimal reactive power scheduling of DERs considering operational constraints in primary and secondary networks. This chapter primarily focuses on rooftop PV integration, although intermittency due to cloud transients is an issue with solar PV. This chapter addresses fully sunny conditions.

3.1 Background on OPF

Traditionally, the loss minimization problem including rooftop PVs is formulated as a nonlinear centralized OPF problem in order to minimize power losses subject to a set of equality and inequality constraints. The goal is to determine the reactive power injection of PV inverters while satisfying operational and security constraints. Mathematically, OPF for loss minimization with rooftop PVs can be expressed as (3.1). Minimize

$$f = \frac{1}{2}\sum_{i}\sum_{j,i\neq j} P_{ij}^{abc} + P_{ji}^{abc} \tag{3.1}$$

subject to the following equality and inequality constraints.

- Three phase distribution power flow equations:

$$P_i^{abc} = \sum_{i=1}^{N} V_i^{abc} V_j^{abc} Y_{ij}^{abc} \cos(\theta_{ij}^{abc} - \delta_i^{abc} + \delta_j^{abc}) \tag{3.2}$$

$$Q_i^{abc} = \sum_{i=1}^{N} V_i^{abc} V_j^{abc} Y_{ij}^{abc} \sin(\theta_{ij}^{abc} - \delta_i^{abc} + \delta_j^{abc}) \tag{3.3}$$

$$P_i^{abc} = P_{Gi}^{abc} - P_{Li}^{abc} \tag{3.4}$$

$$Q_i^{abc} = Q_{Gi}^{abc} - Q_{Li}^{abc} \tag{3.5}$$

- Bus voltage limits:

$$V_i^{min} \leq V_i^{abc} \leq V_i^{max} \tag{3.6}$$

- Distribution line limits:

$$P_{ij}^{abc} \leq P_{ij}^{max} \tag{3.7}$$

- Reactive power limits of rooftop PVs:

$$Q_{Gi}^{min} \leq Q_{Gi}^{abc} \leq Q_{Gi}^{max} \tag{3.8}$$

- Phase imbalance limits:

$$\varepsilon_\delta \frac{2\pi}{3} \leq \delta_i^b - \delta_i^a \tag{3.9}$$

$$\varepsilon_\delta \frac{2\pi}{3} \leq \delta_i^c - \delta_i^b \tag{3.10}$$

$$\varepsilon_\delta \frac{2\pi}{3} < \delta_i^c - (\delta_i^a + \frac{2\pi}{3}) \tag{3.11}$$

$$\delta_i^a < \delta_i^b < \delta_i^c \tag{3.12}$$

where f is the objective function; N is the number of buses; P_i^{abc}, Q_i^{abc} are three phase active and reactive power injected at bus *i*; V_i^{abc} is three phase voltage magnitude at bus *i*; Y_{ij}^{abc} is three phase magnitude of (*i*, *j*) element of Y_{Bus} admittance matrix; θ_{ij}^{abc} is three phase angle of (*i*, *j*) element of Y_{Bus} admittance matrix; δ_i^{abc} is three phase angle of voltage at bus *i*; V^{max}, V^{min} are max and min voltage magnitude; P_{ij}^{max} is maximum active power flow in line *ij*; P_{ij}^{abc} is three phase active power flow in line *ij*; $P_{Gi}^{abc}, Q_{Gi}^{abc}$ are three phase active and reactive power injected at bus *i*; Q_{Gi}^{max} is the max reactive power generation of rooftop PV at bus *i*; $P_{Li}^{abc}, Q_{Li}^{abc}$ are three phase active and reactive power load demand at bus *i*; and ε_δ is phase imbalance tolerance. P_i^{abc}, Q_i^{abc} and $P_{Gi}^{abc}, Q_{Gi}^{abc}$ could be single-phase active/reactive power.

The presented centralized OPF formulation is a non-convex optimization problem. The branch and bound method could solve the problem and provide a global but computationally expensive solution. Moreover, with high proliferation of PVs in medium- and large-scale power distribution systems, solving centralized OPF requires significant investment in meters, communications, and control system infrastructure. A Taylor series expansion can be used to transform the problem to a convex form, thereby reducing the computational burden. A detailed description of conversion to convex form, solving the problem, and comparison of solutions with the branch and bound method is provided in [44]. However, near real-time applications requires faster algorithms in order to deal with the rapid load variations or intermittency in renewable generators. Subsection 3.2 and 3.3 describe the issues in detail and provide a mathematically distributed model to address concerns for solving the loss minimization problem with rooftop PVs in large-scale networks.

3.2 Grid Evolution and Requirements to Solve OPF

Future distribution systems will deploy numerous smart meters, smart inverters, and rooftop PVs into homes located at the secondary level of the distribution network. Consequently, handling optimization problems, especially in large-scale distribution systems based on a flat architecture, will cause dimensionality issues. Placing single-phase households on different phases of the three-phase system is a common utility practice to prevent voltage imbalance, utilities do not have jurisdiction over residents to dictate rooftop PV installation. Therefore, voltage imbalance due to unequal number and sizes of PV installations on the three phases requires attention during the optimization process in unbalanced networks. Overcoming these issues to fully capture the benefits of power distribution system optimization requires a new framework that includes primary and secondary distribution feeders [91]. Unlike the models considered in [33]-[41], this research treats reactive power as a vital resource for voltage regulation and loss reduction, as well as voltage imbalance correction while modeling the system with

primary and secondary feeders. Although the current contracts between the utility and rooftop PV owners only include tariffs for real power exchange, evolving standards and increased penetration of rooftop PV could change these tariffs. Hence in the future, rooftop PV interconnection tariff offered by the utility could include reactive power control standards and limits to meet utility needs, including authority to remotely reprogram the smart inverters [92]. The focus of this research is to leverage reactive power capabilities of smart inverters to minimize system losses without specifically designing new tariffs for reactive power.

Inherently, power distribution systems are highly distributed and hierarchical in structure, motivating use of the analytical target cascading (ATC) method in this research. ATC is tailored to solve hierarchically structured complex problems and has been successfully applied to complex multi-level systems such as automotive design [93], architectural design [94], multidiscipliplinary product development [95], [96], and unit scheduling [73]. These studies have demonstrated ATC scalability on large and computationally intensive case studies. Assumptions, requirements, formulations, and convergence properties of the loss minimization problem based on the ATC method are presented in the following subsection.

3.3 Hierarchical Loss Minimization Architecture

3.3.1 Power Distribution System as a Three-Level Hierarchy

Figure 3.1 shows the hierarchical physical connection of a distribution network described as a three-level network in which every level is a specific part of the network (i.e., primary feeder, lateral feeder, and secondary feeder levels). The primary feeder network represents three-phase primary feeders, and the lateral feeder network embodies single-phase lateral feeders that tap off the primary feeder. Level 3 of the network is represented by the secondary feeder network in which short line-segments branch off distribution transformers and distribute energy to a neighborhood consisting of groups of homes. Notice

that in this research we have used a three-level hierarchy to fit the structure of radial distribution systems in the United States, which comprise of primary main three-phase feeders, single-phase laterals, and distribution transformers with secondary systems connected to homes (see Figure 3.7 for details). However, for a system in another country, depending on topology, any numbers of layers in the hierarchy can be selected without changing the overall foundation of the work.

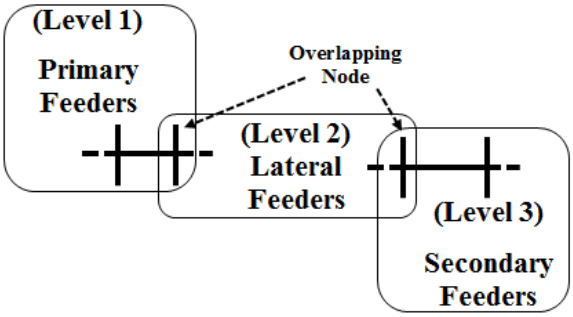

Figure 3.1 Hierarchical physical connection of distribution system

3.3.2 General Description of the ATC Method

Formulation of ATC requires that the entire physical network be decomposed hierarchically into sub-networks of decreasing order. Each sub-network within the hierarchy is then coupled to higher/lower level sub-networks via target and response variables. Targets are set by higher level sub-networks for its lower level sub-networks, while responses defined by lower level sub-networks state how close these targets can be met. A consistency constraint is formulated for target-response relationships between sub-networks and relaxed as a penalty function in the optimization problem of sub-networks. Once a sub-network is solved, targets and responses are exchanged with sub-networks in lower and higher levels. Optimal results are obtained through an iterative process until target and response consistency is achieved for all sub-networks.

Note that the ATC method is only guaranteed convergence for convex problems. However, in practical non-convex problems, the quadratic term of the penalty function used with ATC helps mitigate

non-convexity by acting as a local convexifier [97]. The ATC method has been applied to a series of non-convex problems [98], leading the authors to observe that it converged to appropriate solutions.

3.3.3 Hierarchical Loss Minimization Formulation

Assume a large-scale distribution system with a combined total M of primary feeder, lateral feeder, and secondary feeder networks. There is only one primary feeder network in level 1 and multiple lateral and secondary feeder sub-networks in levels 2 and 3. Lateral feeder level in the middle of the hierarchy is the most general which is linked to both higher and lower level networks. Therefore, this level is used to generalize optimization notation and formulation. Loss minimization for a generic sub-network j can be expressed as

$$\begin{aligned} &\min f_j\left(\bar{\mathrm{x}}_{\boldsymbol{j}}, y_{\boldsymbol{j}}\right) \\ &s.t.\ \mathbf{g}_j\left(\bar{\mathrm{x}}_j, y_j\right) = \mathbf{0} \\ &\mathbf{h}_j\left(\bar{\mathrm{x}}_j, y_j\right) \leq \mathbf{0} \end{aligned} \tag{3.13}$$

where $\bar{\mathbf{x}}_j$ is the set of local decision variables in sub-network j (active and reactive power generation of generation sources), and $\mathbf{y}$ represents coupling variables between the sub-network j and its higher level primary feeder network and its lower level secondary feeder sub-network m. f_j is the objective function (power losses in sub-network j or equivalently power injected into the network from higher level network), and $\mathbf{g}_j$ and $\mathbf{h}_j$ are vectors of equality constraints (power balance) and inequality constraints (voltage magnitude, voltage imbalance, branch flow, and generation limits), respectively.

The coupling variables $\boldsymbol{y}_j$ prevents problem (3.13) from being optimized independently from primary and secondary feeder networks. Therefore, two sets of target ($\mathbf{t}$) and response ($\mathbf{r}$) variables as copies of $\boldsymbol{y}_j$ are introduced to model the coupling variables between networks in primary, lateral, and secondary feeder levels. The decoupling principle in [99] is used, in which boundary between sub-networks are defined based on the overlapping buses connecting primary feeder, lateral feeder, and

secondary feeder sub-networks. Associated with each overlapping bus are power flows through the bus and the voltage and angle for the bus. In order to decouple sub-networks, overlapping buses are duplicated in the primary, lateral, and secondary feeder level sub-networks. As shown in Figure 3.2, the power flows through the overlapping buses are modeled as pseudo load (target) and pseudo generator (response) from the perspective of higher/lower level sub-networks. Furthermore, the voltage and angle for duplicated buses in higher level sub-network are passed to the sub-networks of lower order. These values (voltage and angle) are fixed in the OPF of lower level sub-network and used to set a fixed reference bus voltage and angle corresponding to the duplicated buses.

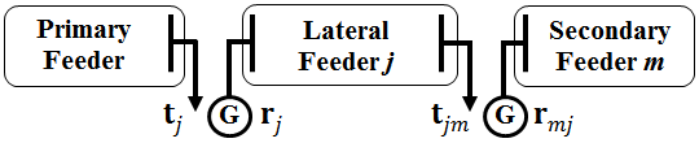

Figure 3.2 Modeling target and response variables.

In particular, $\mathbf{t}_j$ are targets that sub-network *j* receives from the primary feeder network, and $\mathbf{r}_j$ are responses computed by sub-network *j* to match targets from the primary feeder network. Sub-network *j* assigns targets $\mathbf{t}_{jm}$ to the secondary feeder sub-network *m* and receives response variables $\mathbf{r}_{mj}$. Note that sub-network *j* is linked to more than one secondary feeder sub-networks. Therefore, $\mathcal{T}_j$ is defined as the set of secondary feeder sub-networks for which sub-network *j* sets targets and receives responses.

Two sets of consistency constraints related to sub-network *j* are introduced to enforce line flow balance on tie-lines between sub-networks

$$\mathbf{t}_j - \mathbf{r}_j = 0 \tag{3.14}$$

$$\mathbf{t}_{jm} - \mathbf{r}_{mj} = 0, \quad m \in \mathcal{T}_j \tag{3.15}$$

Consistency constraints (3.14) and (3.15) are relaxed as penalty function π in problem (3.16), leading to decomposition of the optimization problem in sub-networks as

$$\min f_j(\tilde{\mathbf{x}}_j) + \pi(\mathbf{t}_j - \mathbf{r}_j) + \sum_{m \in \mathcal{T}_j} \pi(\mathbf{t}_{jm} - \mathbf{r}_{mj})$$

$$\text{s.t. } \mathbf{g}_j(\tilde{\mathbf{x}}_j) = \mathbf{0}$$
$$\mathbf{h}_j(\tilde{\mathbf{x}}_j) \leq \mathbf{0}$$
$$\tilde{\mathbf{x}}_j = [\bar{\mathbf{x}}_j, \mathbf{r}_j, \mathbf{t}_{jm}] \tag{3.16}$$

where $\mathbf{t}_j, \mathbf{r}_{mj}$ for $m \in \mathcal{T}_j$ are constants with respect to sub-network j.

Augmented Lagrangian function is used to model the penalty function because inclusion of linear and quadratic penalty terms improves the speed of convergence [97] and it is widely applied to real-world problems [96]. Therefore, the general form of (3.16) for sub-network j is modified as

$$\min f_j(\tilde{\mathbf{x}}_j) + \boldsymbol{\lambda}_j(\mathbf{t}_j - \mathbf{r}_j) + \left\|\mathbf{w}_j \circ (\mathbf{t}_j - \mathbf{r}_j)\right\|_2^2 + \sum_{m \in \mathcal{T}_j} \boldsymbol{\lambda}_m(\mathbf{t}_{jm} - \mathbf{r}_{mj}) + \left\|\mathbf{w}_m \circ (\mathbf{t}_{jm} - \mathbf{r}_{mj})\right\|_2^2 \tag{3.17}$$

where $\boldsymbol{\lambda}$ and $\mathbf{w}$ are Lagrangian multipliers associated with linear and quadratic terms, $\|\cdot\|_2^2$ represents the square of the l_2 norm, and the $\circ$ operation indicates component-wise multiplication of two vectors.

The optimization problem for sub-network j can be stated as follows: Given the set of targets from super-network and responses from sub-networks, determine local variables, responses to super-network and targets to sub-networks in order to find local variables that minimize the local objective function and inconsistency vector while meeting local equality and inequality constraints. Figure 3.3 shows target-response pairs and the information flow for solving the optimization problem of sub-network j.

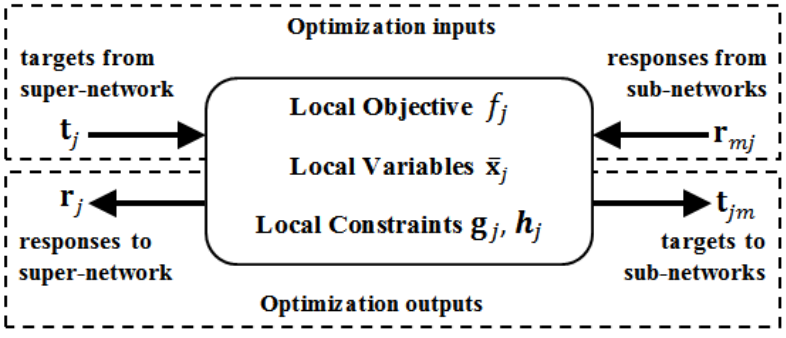

Figure 3.3 Information flow for loss minimization in sub-network j.

To clarify the notation in (3.17), subscripts *PF*, *LF*, and *SF* are introduced to indicate primary feeder, lateral feeder, and secondary feeder levels, respectively. Sub-network *j* in level *LF* is considered to receive the pseudo load demand $\mathbf{P}_{SF,m}^{y}$ from sub-networks and pseudo generation $\mathbf{P}_{PF,j}^{y}$ from the super-network as known input variables and to act as an autonomous network performing its own OPF. Sub-network *j* calculates the pseudo load $\mathbf{P}_{LF,j}^{y}$ and pseudo generation $\mathbf{P}_{LF,m}^{y}$ and passes them on to its super-network/sub-networks as output of the optimization, respectively. The devised model shown in Figure 3.3 and can be formulated as

$$\mathbf{t}_j = \mathbf{P}_{PF,j}^{y} \quad , \mathbf{r}_j = \mathbf{P}_{LF,j}^{y} \tag{3.18}$$

$$\mathbf{t}_{jm} = \mathbf{P}_{LF,jm}^{y} \quad , \mathbf{r}_{mj} = \mathbf{P}_{SF,mj}^{y} \tag{3.19}$$

where y denotes the ABC or A, B, or C phases.

Notice that the proposed approach is general enough to consider the connection of DG units in any level of the hierarchy. For example, a large-scale PV installation can be connected to the backbone of the system by locating the PV generator in the primary feeder network. In this case, reactive power generation of the PV generator will be included in the set of local variables of the primary feeder network. Since the focus of the paper is on rooftop PV integration, in what follows the PV connection to the home level (secondary feeders) will be studied.

3.4 Optimization Description in Decomposed Layers

Mathematical specifications for primary feeder, lateral feeder, and secondary feeder networks are formulated in this section. The optimization problem in each network is solved using the sequential convex programming (SCP) method presented in [44].

3.4.1 Primary Feeder Level Optimization

In the primary feeder level, three-phase OPF is run with the objective of minimizing power losses in the primary sub-network by incorporating full three-phase unbalanced line configurations and phase

loading levels. Decision variables are active and reactive power infeed from substation and target variables to the lower level networks (i.e., active and reactive power of all pseudo loads). Equality and inequality constraints include active and reactive power balance, maximum and minimum active and reactive power capability of pseudo generators, voltages, branch flows and voltage imbalance limits.

3.4.2 Lateral Feeder Level Optimization

Because the lateral feeder level is single-phase, single-phase OPF is used to minimize the power losses in the feeder level sub-networks. Single-phase equality constraints (active and reactive power flow) and inequality constraints (active and reactive power of pseudo generators, voltage, and branch flow limits) are incorporated and no voltage imbalance constraint is considered. Decision variables are response and target variables to and for the higher level and lower level networks (i.e., active and reactive power of the pseudo generator and all pseudo loads).

3.4.3 Secondary Feeder Level Optimization

In this level, decision variables are response variables to higher level networks (i.e., active and reactive power of the pseudo generator) and reactive power of all rooftop solar PVs in the secondary feeder network). Similar to the feeder level, this network is single-phase; therefore, single-phase OPF is to minimize the power losses used such that

$$\underline{QG}_{m,i}^{y} \leq QG_{m,i}^{y} \leq \overline{QG}_{m,i}^{y} \tag{3.20}$$

where $QG_{m,i}^{y}$ is reactive power generation of the ith rooftop PV in the secondary feeder network m, and $\underline{QG}_{m,i}^{y}$ and $\overline{QG}_{m,i}^{y}$ are maximum and minimum reactive power limits of ith rooftop solar PV, respectively. Similar to lateral feeder level, single phase equality and inequality constraints are imposed.

3.5 Solution Methodology

This section initially presents a coordination approach to sequentially and iteratively solve the proposed loss minimization problem, followed by presentation of a strategy for parallelizing the solution process. Finally, the implementation and convergence properties are described.

3.5.1 Coordination Algorithm

Sub-networks as presented in (3.17) are not separable due to the quadratic penalty term. Therefore, a sequential coordination strategy is applied to solve sub-networks through the hierarchy until target/response consistency is achieved. The following steps illustrate the proposed sequential coordination strategy to solve the loss minimization problem:

Step 1. Set counter $k = 0$. Initialize $\lambda^{(k)}$, $\mathrm{w}^{(k)}$, $\mathbf{P}_{PF,j}^{y,(0)}$ and $\mathbf{P}_{LF,jm}^{y,(0)}$.

Step 2. Use $\mathbf{P}_{LF,jm}^{y,(k)}$ as the input, solve sub-network $m, \forall j, \forall \mathrm{m} \in \mathcal{T}_j$ in the secondary feeder, and calculate $\mathbf{P}_{SF,mj}^{y,(k+1)}$ for the lateral feeder super-network.

Step 3. Use $\mathbf{P}_{SF,mj}^{y,(k+1)}$ calculated in Step 2 and $\mathbf{P}_{PF,j}^{y,(k)}$ as input, solve sub-network j, $\forall j$ in the lateral feeder level and calculate $\mathbf{P}_{LF,j}^{y,(k+1)}$ for the primary feeder network and $\mathbf{P}_{LF,jm}^{y,(k+1)}$ for the secondary feeder sub-networks.

Step 4. Use $\mathbf{P}_{LF,j}^{y,(k+1)}$, $\forall j$ calculated in Step 3 as input, solve primary feeder network and calculate $\mathbf{P}_{PF,j}^{y,(k+1)}$ for lateral feeder sub-networks.

Step 5. Check convergence criterion (3.21) to (3.23). If satisfied, the optimal solution is obtained and iteration is stopped; otherwise, go to Step 6.

$$\left|\mathbf{P}_{PF,j}^{y,(k+1)} - \mathbf{P}_{LF,j}^{y,(k+1)}\right| \leq \tau_1 \quad \forall j \tag{3.21}$$

$$\left|\mathbf{P}_{LF,jm}^{y,(k+1)} - \mathbf{P}_{SF,mj}^{y,(k+1)}\right| \leq \tau_1 \quad \forall j, \forall m \in \mathcal{T}_j \tag{3.22}$$

$$\frac{\left|f_j^{(k+1)} - f_j^{(k)}\right|}{f_j^{(k)}} \leq \tau_2 \quad \forall j \tag{3.23}$$

where τ_1 and τ_2 are consistency deviation tolerance.

Step 1. Set $k = k + 1$. Update penalty parameters; $\forall j, \forall m \in \mathcal{T}_j$ and return to Step 2.

$$\lambda_j^{y,(k+1)} = \lambda_j^{y,(k)} + 2\left(w_j^{\boldsymbol{y},(k)}\right)^2 \left(\mathbf{P}_{PF,j}^{y,(k)} - \mathbf{P}_{LF,j}^{y,(k)}\right) \tag{3.24}$$

$$\lambda_m^{y,(k+1)} = \lambda_m^{y,(k)} + 2\left(w_m^{\boldsymbol{y},(k)}\right)^2 \left(\mathbf{P}_{LF,jm}^{y,(k)} - \mathbf{P}_{SF,mj}^{y,(k)}\right) \tag{3.25}$$

$$w_j^{\boldsymbol{y},(k+1)} = \beta w_j^{\boldsymbol{y},(k)} \tag{3.26}$$

$$w_m^{\boldsymbol{y},(k+1)} = \beta w_m^{\boldsymbol{y},(k)}, \beta \geq 1 \tag{3.27}$$

In the above procedure, sub-problems through the hierarchy are dependent on shared coupling variables. For instance, when a primary/lateral feeder runs OPF, optimization problems in lateral/secondary feeders are idle. Therefore, the sequential coordination strategy imposes a high computational burden. Figure 3.4 shows the flowchart of the proposed parallelized coordination strategy. The next section proposes an effective strategy to parallelize the coordination process.

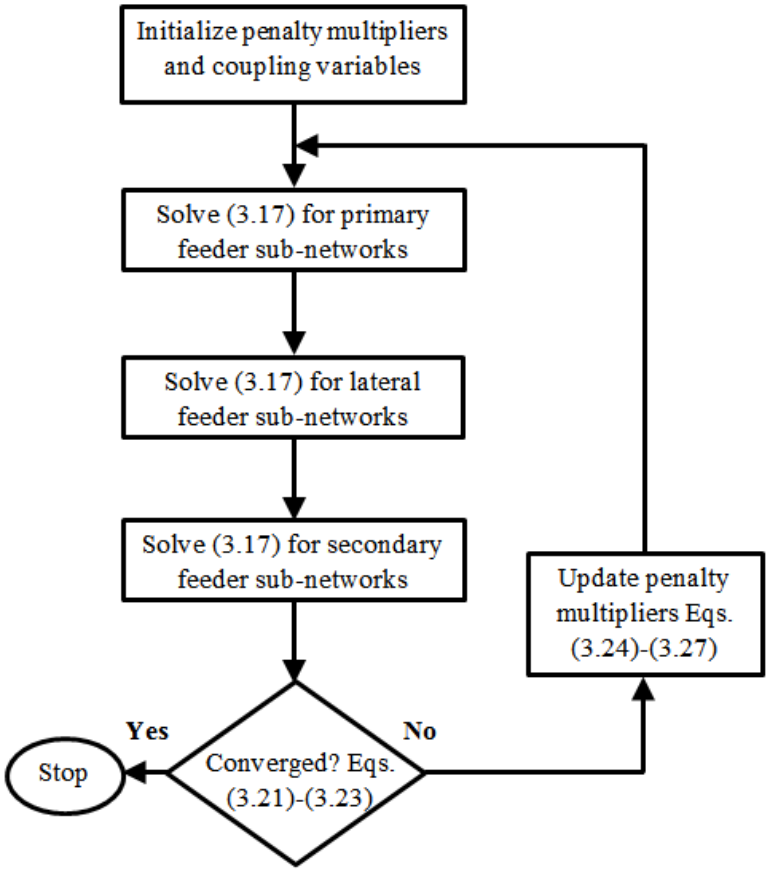

Figure 3.4 Flowchart of the proposed sequential coordination strategy

3.5.2 Parallelized Coordination Formulation

A strategy for parallelizing the coordination process is proposed by introducing a virtual feeder. The virtual feeder acts as a lossless grid without load, generation, or electrical infrastructure and coordinates the exchange of power between actual primary, lateral, and secondary feeder level networks. The virtual feeder decouples sub-networks by introducing new auxiliary variables in the formulation of sub-networks. The modified sub-networks at different levels are coupled only to this virtual feeder (i.e. no connection between sub-networks at different levels), thereby allowing their local optimization to be performed in parallel, as illustrated in Figure 3.5.

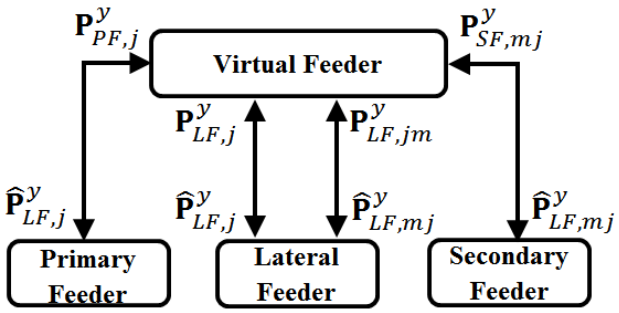

Figure 3.5 Target and response flow with auxiliary responses.

To this end, modeling auxiliary variables and formulating a master optimization problem for the virtual feeder is necessary. The couplings through target-response pairs ($P^{y}_{PF,j}$, $P^{y}_{LF,j}$) and ($P^{y}_{LF,jm}$, $P^{y}_{SF,mj}$) are removed by introducing auxiliary response variables $\widehat{P}^{y}_{LF,j}$ and $\widehat{P}^{y}_{LF,jm}$ as illustrated in Figure 3.5. $\widehat{P}^{y}_{LF,j}$ and $\widehat{P}^{y}_{LF,mj}$ model virtual coupling between actual primary, lateral and secondary levels and the virtual feeder.

Instead of directly exchanging responses and targets among sub-networks, consistency constraints (3.28) and (3.29) for sub-network *j* are redefined using the auxiliary variables as

$$\widehat{\mathbf{P}}^{y}_{LF,j} - \mathbf{P}^{y}_{LF,j} = \mathbf{0} \tag{3.28}$$

$$\widehat{\mathbf{P}}^{y}_{LF,mj} - \mathbf{P}^{y}_{LF,jm} = \mathbf{0}, \quad \forall m \in \mathcal{T}_j \tag{3.29}$$

The general optimization formulation in sub-network *j* suitable for parallel processing is given by

$$\min f_j(\tilde{\mathbf{x}}_j) + \boldsymbol{\lambda}_j\left(\widehat{\mathbf{P}}^{y}_{LF,j} - \mathbf{P}^{y}_{LF,j}\right) + \left\|\mathbf{w}_j \circ \left(\widehat{\mathbf{P}}^{y}_{LF,j} - \mathbf{P}^{y}_{LF,j}\right)\right\|_2^2 +$$

$$\sum_{m\in\mathcal{T}_j} \boldsymbol{\lambda}_m\left(\widehat{\mathbf{P}}^{y}_{LF,mj} - \mathbf{P}^{y}_{LF,jm}\right) + \left\|\mathbf{w}_m \circ \left(\widehat{\mathbf{P}}^{y}_{LF,mj} - \mathbf{P}^{y}_{LF,jm}\right)\right\|_2^2 \tag{3.30}$$

The virtual feeder receives original target and response variables from primary, lateral, and secondary feeder networks, minimizes the error in consistency constraints between auxiliary variables and the original target and response variables, determines the auxiliary variables, and sends them back to the actual feeders. Virtual feeder optimization is formulated as

$$\min \sum_{j=1}^{M} \boldsymbol{\lambda}_j (\widehat{\mathbf{P}}_{LF,j}^{y} - \mathbf{P}_{LF,j}^{y}) + \left\| \mathbf{w}_j \circ (\widehat{\mathbf{P}}_{LF,j}^{y} - \mathbf{P}_{LF,j}^{y}) \right\|_2^2 +$$

$$\sum_{m \in \mathcal{T}_j} \boldsymbol{\lambda}_m (\widehat{\mathbf{P}}_{LF,mj}^{y} - \mathbf{P}_{LF,jm}^{y}) + \left\| \mathbf{w}_m \circ (\widehat{\mathbf{P}}_{LF,mj}^{y} - \mathbf{P}_{LF,jm}^{y}) \right\|_2^2 \tag{3.31}$$

The virtual feeder acts as a power coordinator by enforcing constraints (3.28) and (3.29).

3.5.3 Implementation of the Proposed Parallelized Coordination Algorithm

The proposed power loss minimization algorithm consists of the following steps for parallel processing:

Step 1. Set k =0. Initialize λ, $\mathbf{w}$, $\widehat{\mathbf{P}}_{LF,j}^{y,(k)}$ and $\widehat{\mathbf{P}}_{LF,mj}^{y,(k)}$.

Step 2. Given $\widehat{\mathbf{P}}_{LF,j}^{y,(k)}$ and $\widehat{\mathbf{P}}_{LF,mj}^{y,(k)}$ from the virtual feeder, solve (3.30) for sub-network j, $\forall j, \forall m \in \mathcal{T}_j$ in parallel and calculate $\mathbf{P}_{PF,j}^{y}$, $\mathbf{P}_{LF,j}^{y}$, $\mathbf{P}_{LF,jm}^{y}$ and $\mathbf{P}_{SF,mj}^{y}$.

Step 3. Given $\mathbf{P}_{PF,j}^{y}$, $\mathbf{P}_{LF,j}^{y}$, $\mathbf{P}_{LF,jm}^{y}$ and $\mathbf{P}_{SF,mj}^{y}$ calculated in Step 2, solve (3.31) for the virtual feeder and calculate $\widehat{\mathbf{P}}_{LF,j}^{y,(k+1)}$ and $\widehat{\mathbf{P}}_{LF,mj}^{y,(k+1)}, \forall j, \forall m \in \mathcal{T}_j$.

Step 4. Check termination criteria (3.32) to (3.34). If,

$$\left| \widehat{\mathbf{P}}_{LF,j}^{y,(k+1)} - \mathbf{P}_{LF,j}^{y,(k+1)} \right| \leq \tau_1 \quad \forall j \tag{3.32}$$

$$\left| \widehat{\mathbf{P}}_{LF,mj}^{y,(k+1)} - \mathbf{P}_{LF,jm}^{y,(k+1)} \right| \leq \tau_1 \quad \forall j, \forall m \in \mathcal{T}_j \tag{3.33}$$

$$\frac{\left| f_j^{(k+1)} - f_j^{(k)} \right|}{f_j^{(k)}} \leq \tau_2 \qquad \forall j \tag{3.34}$$

stop; otherwise, go to Step 5.

Step 5. Set $k = k + 1$ and update the Lagrange multipliers defined in (3.35) to (3.38). Go to Step 2.

$$\lambda_j^{y,(k+1)} = \lambda_j^{y,(k)} + 2 \left(w_j^{y,(k)} \right)^2 \left(\widehat{\mathbf{P}}_{LF,j}^{y,(k+1)} - \mathbf{P}_{LF,j}^{y,(k+1)} \right) \tag{3.35}$$

$$\lambda_m^{y,(k+1)} = \lambda_m^{y,(k)} + 2\left(w_m^{y,(k)}\right)^2 \left(\widehat{\mathbf{P}}_{LF,mj}^{y,(k+1)} - \mathbf{P}_{LF,jm}^{y,(k+1)}\right) \quad (3.36)$$

$$w_j^{y,(k+1)} = \beta w_j^{y,(k)} \quad (3.37)$$

$$w_m^{y,(k+1)} = \beta w_m^{y,(k)}, \beta \geq 1 \quad (3.38)$$

Figure 3.6 shows the flowchart of the proposed parallelized coordination strategy.

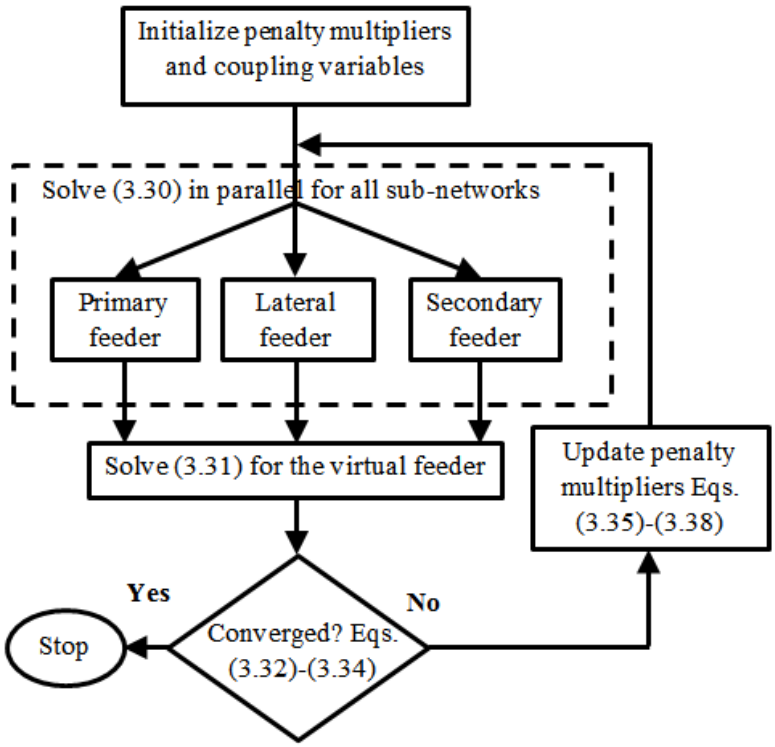

Figure 3.6 Flowchart of the proposed parallelized coordination strategy

3.5.4 Discussion On Convergence

The proposed sequential coordination algorithm relies on the hierarchical ATC method that addresses optimization problems with hierarchical structure using augmented Lagrange relaxation. Solutions of the proposed iterative algorithms have been shown to be Karush–Kuhn–Tucker points of the original nondecomposed optimization problem when the objective and constraint functions are convex [100], [101]. However, the presented OPF for each sub-network is a non-convex optimization problem.

To ensure convergence, the problem is converted to convex form via the SCP method described in the author's previous work [44], [102].

The proposed sequential coordination procedure terminates when all conditions (3.21) to (3.23) are satisfied. Conditions (3.21) and (3.22) indicate that the maximum consistency constraint violation must be less than τ_1 while constraint (3.23) ensures sufficient accuracy of results. Conditions (3.21) to (3.23) are complementary in an attempt to prevent premature convergence and non-consistent solutions by choosing significantly small values for τ_1 and τ_2. For the considered case study, empirical testing showed that convergence is efficiently attained with the choice of 10^{-3} for τ_1 and τ_2.

The parallelized coordination algorithm follows the convergence properties of the sequential coordination algorithm in a sense that its structure resembles a bi-level sequential formulation. The difference with the sequential formulation is that the higher level problem is an artifact of parallelization, whereas the lower level problem is associated with the actual networks.

3.6 Simulation Results

In this section, two small- and large-scale system, built based on IEEE 37 node test feeder, are used to investigate the performance of the proposed distributed algorithms for loss minimization using residential PV inverter capabilities. The studies were implemented on an Intel(R) Core(TM) i7, 3.4 GHz personal computer with 8 GB of RAM.

3.6.1 Network and Parameter Description

Figure 3.7 shows the modified IEEE 37 node test feeder where an extended network is modeled by lines branching out of primary feeder node 31 (i.e., from node 38 to 41). It is assumed that each distribution transformer distributes power to a neighborhood consisting of four homes. Using the same analogy, the network is extended for primary feeder node 34 (not shown in Figure 3.7). Characteristics of distribution transformers, overhead conductors and service drops are described in detail in [19]. The extended network consists of 73 nodes and 8 and 16 homes in phase A and B, respectively.

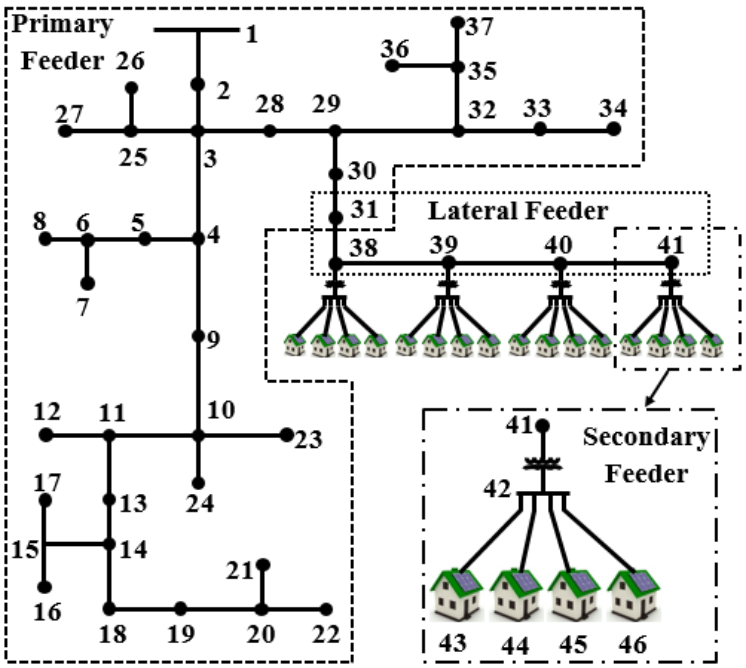

Figure 3.7 Illustration of the test feeder including multi-level feeders.

PV-enabled homes are selected randomly for each phase with 50% having rooftop PV. In particular, for the small-scale network, PV-enabled homes in the extended feeder are located at nodes 43, 45, 51, 54, 55, 56, 58, 59, 60, 61, 65, 70, 71, and 72. PV generation size at each home is randomly calculated based on roulette wheel selection with PV size to peak load ratio (ρ) and a probability distribution function presented in Table 3.1. However, the proposed methodology is applicable to any other method for PV size selection.

Table 3.1 PV size to peak load ratio (ρ) and probability distribution.

ρ	0.25	0.5	0.75	1	1.5	2
Probability	0.09	0.28	0.28	0.28	0.05	0.02

PV generation is obtained from NREL data measured in Hawaii [90]. Various home load data were extracted from the eGauge website [89] and homes were placed in phases A, B, and C to maintain the unbalanced characteristic of the system. It is assumed that inverters are oversized by 20% and capable of providing reactive power up to 0.8 power factor. Power factor of 0.9 lagging were assumed for load

reactive power. Accepted voltage range is set from 0.95 to 1.05 p.u. Initial values for λ and w are set to 0 and 1, while initial values for τ_1 and τ_2 are set to 10^{-3}.

3.6.2 Result of Sequential ATC vs. Centralized Approach

Table 3.2 shows the total active/reactive power losses, the total reactive power generation from PV inverters and the active/reactive power drawn from the substation (P_s and Q_s) using the centralized and distributed sequential approaches. It can be seen that results from the distributed sequential method are comparable with results obtained via the centralized method. Errors observed are 2.07%, 2.15%, 1.9%, 0.17% and 2.92% for total active power losses, total reactive power losses, total reactive power generation from the PV inverters, active power drawn from the substation, and reactive power drawn from substation, respectively.

Table 3.2 Results comparison for the sequential ATC and centralized approaches.

	Sequential ATC			Centralized		
	Phase A	Phase B	Phase C	Phase A	Phase B	Phase C
P_{loss} (kW)	6.597	3.469	4.7086	6.496	3.423	4.654
Q_{loss} (kvar)	2.570	1.174	1.5638	2.480	1.1658	1.5162
$\sum Q_g$ (kvar)	156.600	204.710	214.7800	159.800	202.300	218.670
P_s (kW)	384.600	360.360	435.2100	384.500	360.314	435.155
Q_s (kvar)	278.200	232.960	263.0700	276.31	235.362	259.132

Figure 3.8(a) and Figure 3.8(b) show the error evolution in active and the reactive power flowing through nodes 31, 38, 39, 40 and 41 by applying sequential approach. Optimum values were obtained after 5 iterations.

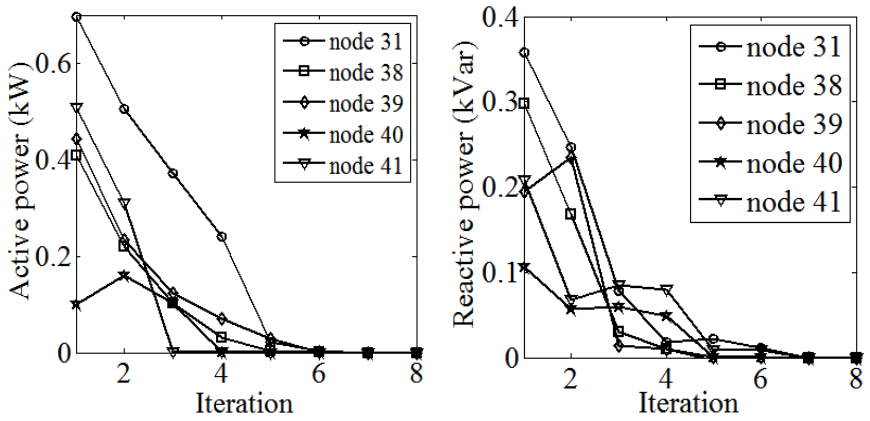

(a) **(b)**

Figure 3.8 Error evolution through nodes 31, 38, 39, 40 and 41 via sequential coordination approach

3.6.3 Sequential ATC vs. Other Methods of Reactive Power Control

In this section results from sequential ATC approach are compared with no control and a local control approach for reactive power injection.

For quantitative comparison, voltage imbalance (VI) for each bus *i* in phase *y* is defined as

$$VI_i^y = 100.\frac{|V_i^y - V_i^{ave}|}{V_i^{ave}} \tag{3.39}$$

where $V_i^{ave} = (V_i^A + V_i^B + V_i^C)/3$. Maximum voltage imbalance (MVI) is defined as the maximum VI value for all buses in the network.

1. No reactive power control

PV inverters have no reactive power control and they operate at unity power factor according to the practice recommended by the old version of IEEE Std. 1547 [103] for interconnection of distributed resources. An amendment recently issued allows reactive power injection [46].

2. Local reactive power injection control

Local PV inverter reactive power control strategy is used in which local load and generation measurements determine PV reactive power [19]. Using voltage drop formula and assuming that the R/X ratio is equal to 1, which is typical for lines in distribution system in the United States, yields

$$QG_{n,i}^{y} = QL_{n,i}^{y} + PL_{n,i}^{y} - PG_{n,i}^{y} \quad (3.40)$$

where $PL_{n,i}^{y}$, $QL_{n,i}^{y}$, and $PG_{n,i}^{y}$ are active and reactive power consumption and active power generation of the ith PV-enabled home in the secondary lateral network n, respectively. PV inverter reactive power calculated in (3.40) is subject to constraints imposed by (3.20). Note that any other value of R/X ratio, specific to a given network, can be used without affecting the algorithm.

Total active power losses, total reactive power losses, total reactive power generation from PV inverters, active and reactive power drawn from the distribution substation, and MVI observed from implementing no control and local control approaches are shown in Table 3.3. Application of local control results in lower total active and reactive power losses compared to the fixed power factor method and use of local rule (3.40) to inject reactive power significantly reduces reactive power drawn from the substation.

Table 3.3 Results from no control, and local control strategies for PV reactive power generation

	No Control			Local Control		
	Phase A	Phase B	Phase C	Phase A	Phase B	Phase C
P_{loss} (kW)	8.9744	6.6038	8.0388	8.6213	4.156	6.597
Q_{loss} (kvar)	3.2728	2.2107	2.7350	3.4458	1.299	2.570
$\sum Q_g$ (kvar)	0	0	0	65.8520	238.400	156.600
P_s (kW)	387.7740	364.3700	439.2150	387.1500	361.700	437.098
Q_s (kvar)	433.4970	436.8600	477.5270	368.0700	197.800	278.200
MVI (%)	6.67			4.89		

The sequential coordination approach presented in this research further reduces losses via optimal reactive power provisioning from PV inverters. In particular, active and reactive power losses decreased

37.44% and 35.41% compared to the fixed power factor method and 23.74% and 27.43% compared to the local control method. Improvements achieved via the sequential coordination approach utilized 25% more reactive power compared to the local control method. Moreover, active and reactive powers drawn from the substation are considerably reduced.

When the unity power factor method is utilized, MVI is 6.67, whereas MVI is 4.89 with the local control method (i.e. MVI is decreased 26.68%). MVI associated with the sequential coordination framework is 2.89, demonstrating that when the proposed strategy is implemented, the MVI value effectively decreased 56.67% and 40.9% compared to no control and local control methods, respectively.

Table 3.4 Results comparison for PV reactive power generation strategies via no control, local control, and sequential optimization.

	Sequential Optimized Control			Percent Improvements	
	Phase A	Phase B	Phase C	Optimized vs No Control	Optimized vs Local Control
P_{loss} (kW)	6.597	3.4690	4.7086	37.4408	23.7412
Q_{loss} (kvar)	2.570	1.1742	1.5638	35.4140	27.4348
$\sum Q_g$ (kvar)	156.600	204.7100	214.7800	N/A	-25.0054
P_s (kW)	384.600	360.3600	435.2100	0.9391	0.4872
Q_s (kvar)	278.200	232.9600	263.0700	42.5600	8.2742
MVI (%)	2.89			56.6700	40.90

* Except for the MVI, listed values represent the sum throughout the entire distribution system.

3.6.4 Result from Parallelized Coordination Algorithm

Results from hierarchical parallelized and sequential coordination strategies are compared in this section. Initial values for λ, w, τ_1 and τ_2 were set the same as Section 3.5.2. Table 3.5 shows total active and reactive power losses, total reactive power generation from PV inverters, and active and reactive power drawn from the substation (P_s and Q_s) using the sequential and parallelized approaches. Results from the parallelized method were comparable to sequential method results. Absolute errors are 0.49%

and, 0.37% for total active and reactive power losses, respectively, 0.36%, and 1.29% for active and reactive power drawn from the substation, respectively, and 3.6% for total reactive power generation from PV inverters. When the parallelized coordination strategy is implemented, MVI is 2.97, impliying 2.76% increase compared to the sequential coordination method.

Table 3.5 Results comparison for parallelized and sequential coordination approaches.

	Parallelized			Sequential		
	Phase A	Phase B	Phase C	Phase A	Phase B	Phase C
P_{loss} (kW)	6.685	3.452	4.798	6.597	3.4690	4.7086
Q_{loss} (kvar)	2.64	1.170	1.610	2.570	1.1742	1.5638
$\sum Q_g$ (kvar)	151.10	208.640	207.030	156.600	204.7100	214.7800
P_s (kW)	385.88	359.043	436.830	384.600	360.3600	435.2100
Q_s (kvar)	281.27	229.950	270.116	278.200	232.9600	263.0700
MVI (%)	2.97			2.89		

Figure 3.9 (a) and Figure 3.9(b) show active and reactive power through overlapping node 41 (connecting lateral and secondary feeders) via the parallelized coordination algorithm. The iterative process converged after 14 iterations in which powers flowing through node 31 from lateral, secondary, and virtual feeders' perspective are matched. Figure 3.9(c) and Figure 3.9(d) show the converged active and reactive power flowing through overlapping node 31 (connecting primary and lateral feeders) from primary, lateral, and virtual feeders' perspective. The virtual feeder minimizes the interaction errors between sub-networks in different levels.

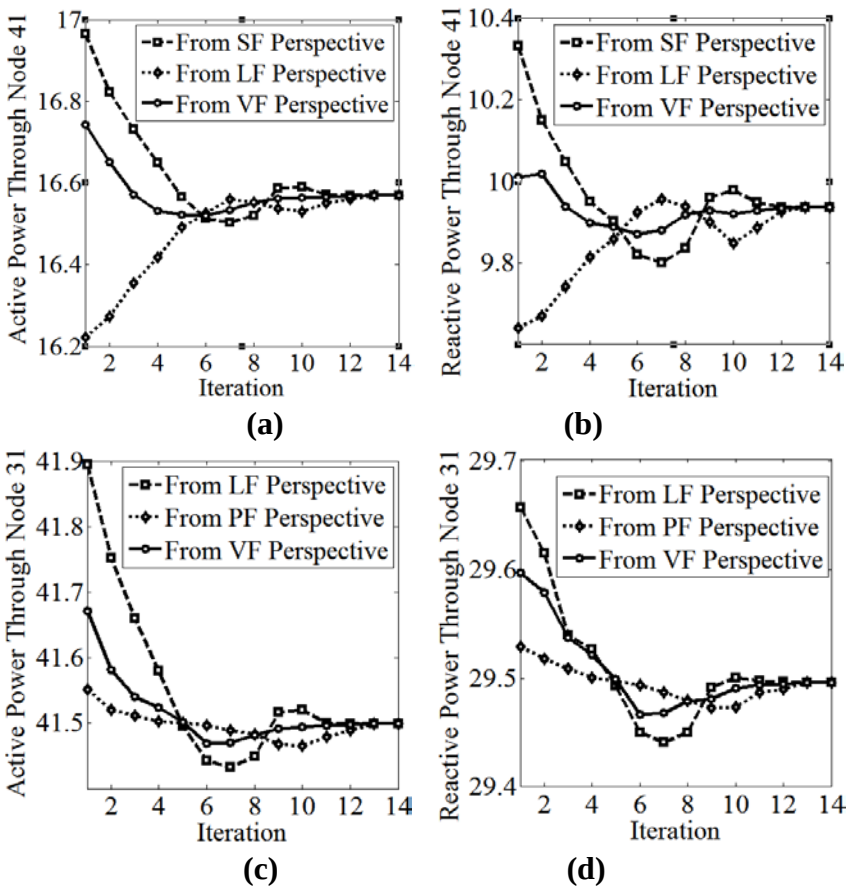

Figure 3.9 Power through overlapping nodes from primary, lateral, secondary and virtual feeder perspective, (a) active power through node 41, (b) reactive power through node 41, (c) active power through node 31, and (d) reactive power through node 31.

Execution times are 118 seconds (approximately 2 minutes) for the parallelized approach and 355 seconds (approximately 6 minutes) for the sequential approach, demonstrating significant reduction in execution time with slight accuracy loss for the parallelized approach compared to the sequential approach. Execution times for solving the large-scale network are much less than the 15-min. resolution commonly used for measuring customer demands and are suitable for the loss minimization approach presented in this research.

3.7 Summary

This chapter presented a three-level hierarchical architecture to improve the performance of large-scale unbalanced distribution systems with high rooftop PV penetration. Initially, a sequential

coordination strategy was introduced to solve the loss minimization problem via optimal reactive power generation scheduling of rooftop PVs. Numerical tests on the modified IEEE 37 node test feeder demonstrated that the proposed sequential approach is advantageous compared to the fixed power factor approach and simplified local control schemes. Furthermore, a parallelized coordination strategy was developed, and its validity and accuracy were tested against the sequential coordination model for solution accuracy and computational burden. Results highlighted significant reduction in execution time for loss minimization in large-scale unbalanced networks via implementation of the proposed parallelized coordination strategy. The results were promising and the method can possibly be scaled for even larger systems and other factors can be included in the optimization problem.

Chapter 4 - Dynamic Operational Scheme for Residential PV Smart Inverters

This chapter proposes a novel dynamic PV inverter reactive power control scheme to address adverse impacts while exploiting benefits related to high penetration of rooftop PV in various weather conditions. Simulation results on the developed test system in Chapter 2 demonstrate superior performance of the proposed control scheme compared to other reactive power control strategies.

4.1 Background on Reactive Power and Voltage Control Devices

Utilities have traditionally used load tap-changer (LTC) transformer, step voltage regulator (SVR), and capacitors for reactive power and voltage control in distribution systems, as shown in Figure 4.1. LTCs, located in distribution substations, are the most common devices to regulate voltage. LTCs are tap-changing autotransformers designed to regulate voltage if it violates preset limits. SVRs, also tap-changing autotransformers designed to regulate voltage, are typically located downstream of the substation. Capacitors, which are common reactive power compensators in distribution systems, can be found in substations and distribution feeders.

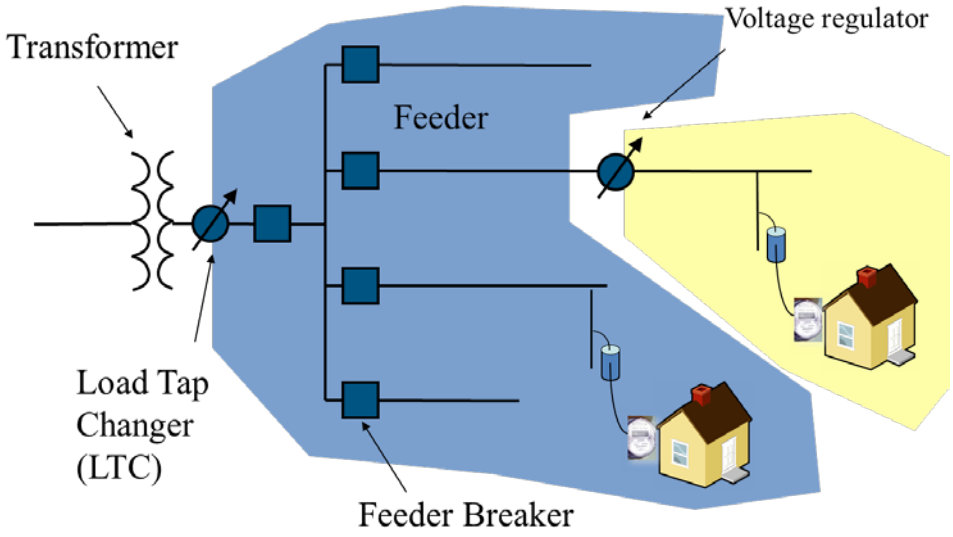

Figure 4.1 Voltage control devices in distribution system

LTC and SVR are designed to change positions a few times a day to regulate the voltage with respect to variations in the load. However, they are not equipped for fast responses to ramping behavior of solar PV. Moreover, transient cloud cover can rapidly reduce solar power generation, cause temporary voltage drop and tap changer cycling.

This necessitates new advanced design and faster controls to handle this phenomenon. Smart inverters are able to inject/absorb reactive power in milliseconds and mitigate the voltage fluctuations due to solar irradiance intermittency. Since PVs are connected to the grid through inverters, as shown in Figure 4.2, PVs are able to contribute in voltage and reactive power generation and guarantee the availability of power throughout the course of the year.

Figure 4.2 General configuration of PV, inverter, and the electric grid

Although PV systems are becoming increasingly competitive due to decreasing costs and improved technology, utilities are concerned that reliability of the current grid will be degraded with large-scale integration of rooftop PV. Literature review shows that the concern stems partly from lack of pilot studies to confirm capability of smart PV inverters in voltage support and lack of viable control schemes to mitigate voltage fluctuations and prevent interference with LTC transformer operation [104].

The above perceived technical limitation along with open discussions about control authority and necessary policy instruments for feed-in-tariff and potential protection issues are the primary reasons that annual PV contribution to electricity demand is less than 1% in the United States [3].

Subsection 4.2 presents available inverter reactive power control strategies and their functionalities that help increase understanding of the value of PV inverters.

4.2 Overview of Inverter Reactive Power Control Strategies

Worldwide interest in rooftop PV installation has created the need for additional network regulations in order to achieve safe and reliable operation of low voltage (LV) grid. Although previous version of IEEE 1547 Std. [45] prohibited reactive power support by distributed generation (DG) in LV grids, a recently published amendment [2] and standards issued in Germany [3] and Italy [4] specify DG reactive power control strategies in order to maintain power quality levels or provide ancillary services for the LV network. Inverter reactive power control strategies for LV grid operation are discussed in this Chapter.

4.2.1 Unity Power Factor with Limit on Active Power

In the unity power factor strategy, shown in Figure 4.3 (a), the PV inverter operates with no injection of reactive power into the grid in order to comply with the previous version of IEEE Std.1547 (i.e., distributed resources do not regulate voltage at the point of common coupling (PCC)). In some applications, a fixed limit (70%) on PV maximum active power generation (P_{max}) is enforced to prevent voltage rise from the installed PV systems without a utility remote control unit.

4.2.2 Cosφ(P) Control

The $cos\varphi(P)$ characteristic curve for the connection of generation units at low voltage is shown in Figure 4.3 (b). In order to mitigate voltage rise, a PV unit must operate in reactive power consumption mode when the feed-in active power exceeds a specified threshold (P_{th}). However, the approach does not actively regulate voltage at the PCC because unnecessary reactive power absorption increases line losses and degrades power quality due to voltage fluctuations caused by fast ramping of PV unit on intermittent cloudy days.

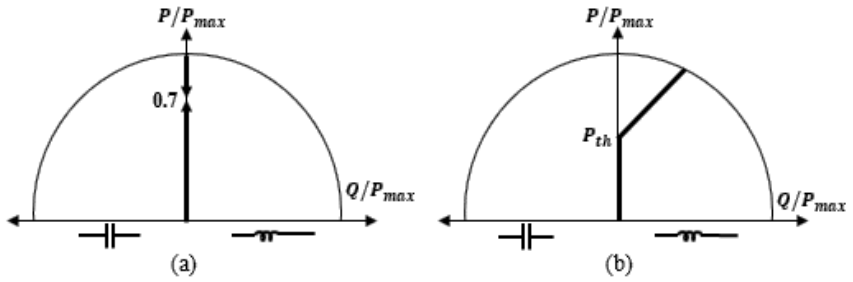

Figure 4.3 Schematic operational curve of PV inverter: (a) unity power factor method and (b) cosφ(P) method.

4.2.3 Q(V) Control

The $Q(V)$ control strategy determines PV inverter reactive power based on voltage at the PCC, as shown in Figure 4.4 (a). PV inverter absorbs/injects reactive power if its terminal voltage is higher or lower than the predefined upper/lower critical voltages, V_{cr}^{U} and V_{cr}^{L}, respectively. Voltage magnitudes at PV buses near the substation transformer typically are within the range; therefore, these PV inverters do not contribute in voltage regulation. Only PV inverters near the end of the feeder provide reactive power and voltage support, causing additional stress on these inverters. Because the controller is designed for voltage rise situations, it does not react to voltage fluctuations [5], [9].

4.2.4 Q(V)/P(V) Control

The $Q(V)/P(V)$ characteristic curve is shown in Figure 4.4 (b). The control strategy is similar to the $Q(V)$ method with the addition of an active power curtailment ($P_{curtail}$) feature for the PV inverter in case of voltage rise at the PCC. As a result, the approach could not accommodate reactive power support for power loss reduction or control voltage fluctuations.

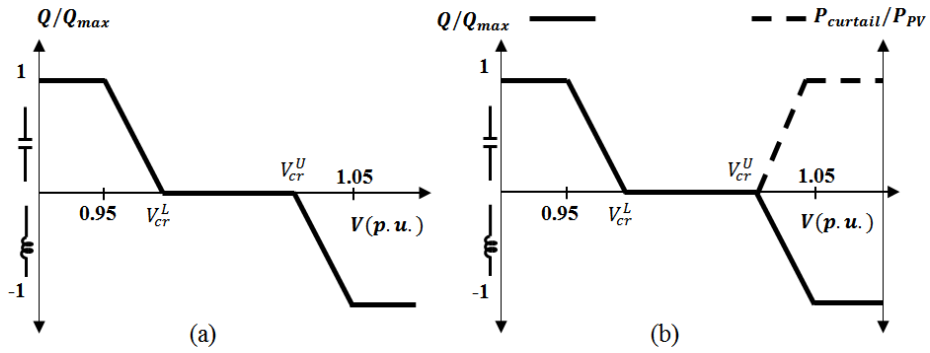

Figure 4.4 Schematic operational curve of PV inverter: (a) Q(V) method and (b) Q(V)/P(V) method.

4.3 Inverter Rating and Technical Requirements

In order to accommodate large penetration of PV in distribution systems, some utilities are attempting to mandate smart inverters for all new solar facilities within their service territories [7]. Smart inverters are equipped with a programmable logic controller (PLC) [105], [106] with extremely fast response times (milliseconds) [107] that enables many functionalities including reactive power provision, as a function of external setpoints [108]. Because the proposed control scheme has a time resolution of 1-second, the response time of the inverter was not explicitly included in formulation of the solution. If properly regulated, the PV inverter could act as an active control component to eliminate or mitigate feeder voltage variations while providing loss reduction and voltage quality support by dynamically provisioning reactive power at the area of greatest need, the customer site. Figure 4.5 illustrates smart PV inverter operation in a 2-quadrant P-Q plane. In the figure, the feasible operating space is enclosed by dashed straight lines that represent the total harmonic distortion (THD) limit [26] and inverter rating curve.

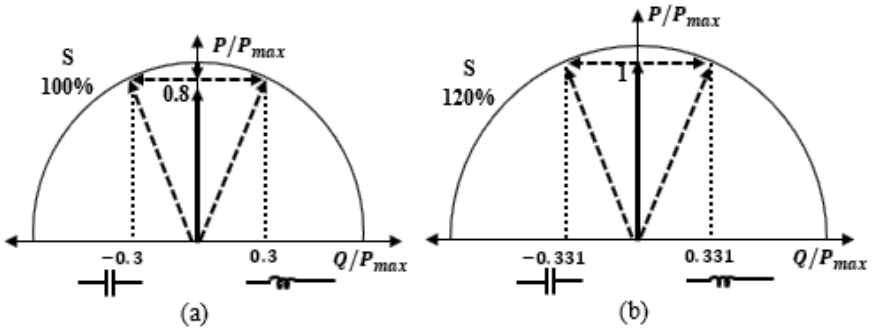

Figure 4.5 Operational area for standard and oversized PV inverter at 0.8 PF.

As shown in Figure 4.5 (a), rooftop PVs with standard-sized inverters must reduce a portion of real power generation in order to accommodate a reasonable amount of reactive power contribution near full active power. However, power reduction is not desirable because customers assign priority to active power generation. Moreover, if voltage rise or voltage drop occurs in the system, tangible capacity from PV inverters may be unavailable to provide higher levels of reactive power and voltage support. Therefore, oversized inverters can be used (Figure 4.5 (b)) to increase maximum reactive power available (Q_{PV}^{max}) at rated PV power (P_r) as

$$Q_{PV}^{max} = \sqrt{[(1+\gamma).S]^2 - P_r^2} \tag{4.1}$$

where γ is the inverter oversize factor. The THD limit also imposes upper and lower bounds on reactive power generation specified by a given PV power factor (PF) as

$$Q_{PV}^{max} = P_{PV}.tan(cos^{-1} PF) \tag{4.2}$$

where *tan* is the tangent function.

4.4 Voltage Sensitivity Analysis

The purpose of voltage sensitivity analysis is to quantify the relationship between nodal voltage magnitudes ($\boldsymbol{V}$) and angles ($\boldsymbol{\theta}$) with respect to nodal active power ($\boldsymbol{P}$) and reactive power ($\boldsymbol{Q}$) injections that are mathematically coupled by power flow equations [12] as

$$P_i = \sum_{i=1}^{N} |V_i| \cdot |V_j| \cdot |Y_{ij}| \cdot \cos(\theta_{ij} - \delta_i + \delta_j) \tag{4.3}$$

$$Q_i = \sum_{i=1}^{N} |V_i| \cdot |V_j| \cdot |Y_{ij}| \cdot \sin(\theta_{ij} - \delta_i + \delta_j) \tag{4.4}$$

where P_i, Q_i, V_i, δ_i denote active power, reactive power, voltage magnitude, and phase angle at bus *i*, respectively. $Y_{ij}\angle\theta_{ij}$ is admittance of the line from bus *i* to bus *j*.

Sensitivity matrix (S) is derived from partial derivation of $\boldsymbol{P}$ and $\boldsymbol{Q}$ with respect to $\boldsymbol{V}$ and $\boldsymbol{\theta}$ as

$$\begin{bmatrix}\Delta\boldsymbol{V}\\ \Delta\boldsymbol{\theta}\end{bmatrix} = \begin{bmatrix}[S_{VP}] & [S_{VQ}]\\ [S_{\theta P}] & [S_{\theta Q}]\end{bmatrix}\begin{bmatrix}\Delta\boldsymbol{P}\\ \Delta\boldsymbol{Q}\end{bmatrix} \tag{4.5}$$

where S_{VP} and S_{VQ} are sensitivities of bus voltage magnitudes to active and reactive powers, respectively, and $S_{\theta P}$ and $S_{\theta Q}$ are sensitivities of bus angles. In particular, voltage variation in bus *i* due to 1 p.u. reactive power change at bus *j* can be interpreted as S_{VQ}^{ij}.

Voltage sensitivity analysis has been used for applications such as voltage rise prevention via PV inverter reactive power consumption or active power curtailment [8], [12], [27], and voltage variation mitigation at a target bus due to operation of a wind turbine in a microgrid via reactive power support [28]. In this study, voltage sensitivity analysis is used to locally determine PV inverter reactive power due to its efficacy in quantifying power losses and bus voltage variations with respect to changes in PV and load profile.

4.5 Proposed Dynamic Control Strategy

The proposed dynamic reactive power control strategy considers three states of operation and associated goals for each PV unit in which the inverter is allowed to monitor its terminal voltage. The first state (or normal state) is associated with reactive power control in slow PV ramping periods (i.e., sunny or overcast periods in which loss reduction is the main objective). The second state (or fluctuating state) deals with fast ramp-up and ramp-down PV power generation during intermittent cloudy periods in order to smooth the voltage profile throughout the feeder. The third state (or contingency state) is experienced when PV terminal voltage deviates from the normal range since low load with high generation or high load with low generation periods are possible operational scenarios. The objective is to

eliminate or reduce overvoltage or undervoltage in the grid. Figure 4.6 shows voltage evolution through time in normal, fluctuating, and contingency states without reactive power control.

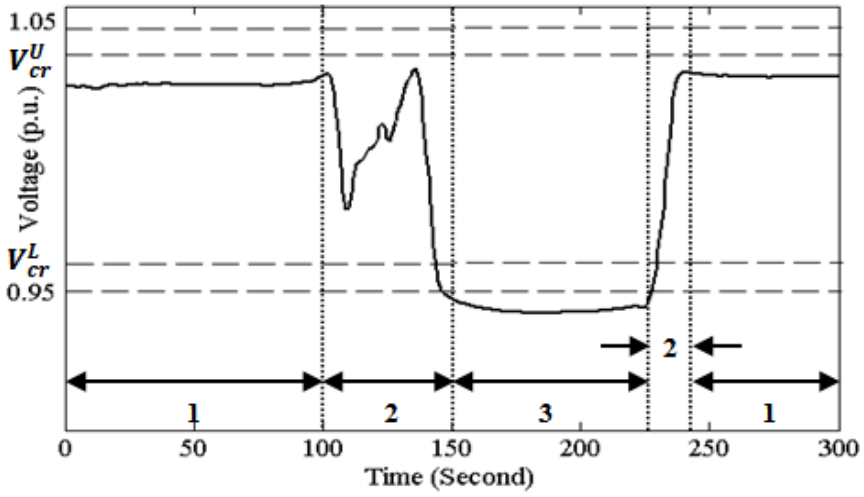

Figure 4.6 Voltage evolution in normal, fluctuating, and contingency states without reactive power control.

4.5.1 Normal State

The normal state includes two control logics based on local voltage. When voltages are within the predefined upper and lower critical voltages (V_{cr}^{L},V_{cr}^{U}), the objective is to provide reactive power for voltage support and power loss reduction in the network. If voltage reaches the upper (V_{cr}^{U}) or lower (V_{cr}^{L}) threshold, the objectives are to provide reactive power support for loss reduction, prevent local overvoltage or undervoltage, and maintain voltages within the normal range. Control strategies are local with no broadcast command needed to switch between actual operation controls. In this dissertation, lower and upper critical voltages were initially set to 0.958 p.u. and 1.042 p.u. around the normal operating voltage range from 0.95 p.u. to 1.05 p.u. as an illustration of the proposed methodology. Two additional ranges of critical voltages were tested to see their effect on the results; small changes in the results were evident, but no significant impact was observed on the control scheme.

Because calculation of exact power losses via local measurements is impossible, deviation of PV bus voltage magnitude from nominal value is considered to be an approximate measure for power losses.

Once the difference between buses' voltages and unity is reduced, the voltage profile will be flatter and thus, the losses will be decreased. Consider a feeder supplying a house through a line with impedance R + jX, the voltage drop at the end of the line with respect to the beginning of the feeder can be approximated as

$$\Delta V = \frac{R.(P_L^i - P_{PV}^i) + X.(Q_L^i - Q_{PV}^i)}{V} \tag{4.6}$$

where P_L^i and Q_L^i are the active and reactive power of load and P_{PV}^i and Q_{PV}^i are the active and reactive power of PV at bus i, respectively, and V is the nominal voltage [29], [30].

In order to achieve zero voltage drop (i.e., ideal voltage regulation), reactive power generation of PV unit i at generic time step k should be

$$Q_{PV}^{i,(k)} = Q_L^{i,(k)} - (R/X).(P_L^{i,(k)} - P_{PV}^{i,(k)}) \quad . \tag{4.7}$$

However, defining a unique R/X ratio for the reactive power control logic in (4.7) is not straightforward due to various network parameters, conductor types (cable or overhead lines), and feeder length. In contrast, voltage sensitivity to active/reactive power variations at each bus can be calculated for each network [12]. Hence, (4.7) can be reformulated as

$$Q_{PV}^{i,(k)} = Q_L^{i,(k)} - \left(\frac{S_{VP}^{ii}}{S_{VQ}^{ii}}\right).(P_L^{i,(k)} - P_{PV}^{i,(k)}) \tag{4.8}$$

where S_{VP}^{ii}, S_{VQ}^{ii} are voltage sensitivity indices at bus i due to 1 p.u. active/reactive power change at bus i, respectively.

Although $Q_{PV}^{i,(k)}$ is calculated in (4.8) at each time step, PV terminal voltage $V_{PV}^{i,(k)}$ is monitored to determine if it is higher than V_{cr}^{U} or lower than V_{cr}^{L}. If so, the PV inverter control overrides the regular reactive power provisioning using Q_{PV}^{i} calculated in (4.8) and a $Q(V)$ droop characteristic [9]

$$Q_{PV}^{i,(k)} = Q_{PV}^{i,(k)} - \begin{cases} \frac{Q_{PV}^{i,(k)} + Q_{max}^{i}}{1.05 - V_{cr}^{U}} \left(V_{PV}^{i,(k)} - V_{cr}^{U}\right) \;\; if \;\; V_{PV}^{i,(k)} \geq V_{cr}^{U} \\ \frac{Q_{PV}^{i,(k)} - Q_{min}^{i}}{V_{cr}^{L} - 0.95} \left(V_{cr}^{L} - V_{PV}^{i,(k)}\right) \;\; if \;\; V_{cr}^{L} \leq V_{PV}^{i,(k)} \end{cases} \tag{4.9}$$

where Q_{max}^{i} and Q_{min}^{i} are maximum and minimum PV inverter reactive power capacities at node *i*. Whenever $V_{PV}^{i}(k) < V_{cr}^{U}$ or $V_{PV}^{i}(k) > V_{cr}^{L}$, the inverter reactive power control (4.9) is switched back to the original control (4.8).

4.5.2 Fluctuating State

Transient cloud movement is the key cause for short-term intermittency in PV output, and PV power variability is reflected in rapid bus voltage or grid power fluctuations. The PV inverter can react to rapid voltage and power changes in a few milliseconds. **Error! Reference source not found.** shows transition from state 1 to state 2 as voltage starts to fluctuate due to sudden PV generation drop around 100 seconds.

Considering the local voltage regulation at bus *i*, voltage variation can be approximated as

$$\Delta V_i = S_{VP}^{ii} . \Delta P_i + S_{VQ}^{ii} . \Delta Q_i \quad . \tag{4.10}$$

For ideal voltage regulation ($\Delta V_i = 0$), the PV inverter can make voltage variation caused by real power fluctuations to be zero by adjusting its reactive power output as

$$\Delta Q_i = -\left(\frac{S_{VP}^{ii}}{S_{VQ}^{ii}}\right) \cdot \Delta P_i \quad . \tag{4.11}$$

The variable reactive power control strategy to mitigate voltage fluctuations can be derived as

$$Q_{PV}^{i,(k)} = Q_{PV}^{i,(k-1)} - \left(\frac{S_{VP}^{ii}}{S_{VQ}^{ii}}\right) \cdot \Delta P_{PV}^{i} \tag{4.12}$$

where ΔP_{PV}^{i} is PV power output variation at bus *i*. Variable reactive power modulation is initiated when PV variation ($\Delta P_{PV}^{i}/dt$) is greater than PV ramp rate threshold (ε).

4.5.3 Contingency State

Whenever voltage violates the normal operating range, the system transitions to voltage deviation state. In this state, the objective is to inject/absorb reactive power so that voltages are pushed back to the normal range. The control includes two control logics to prevent overvoltage or undervoltage situations.

4.5.3.1 Overvoltage Control

A PV unit with terminal voltage of 1.05 p.u. has fully utilized its reactive power adjustment capability and cannot mitigate overvoltage without proceeding to active power curtailment. Furthermore, according to electrical requirements for inverter-based distribution systems [12], [31] the upper operating voltage bound (V_{UB}) is set to 1.058 p.u. In oreder to prevent additional voltage rise, no active power generation is allowed beyond 1.058 p.u. However, for terminal voltage between 1.05 p.u. and 1.058 p.u., the PV inverter curtails active power as shown in **Error! Reference source not found.**(b). More specifically, the PV reactive power setting is frozen to Q_{min}^{i} while the dynamics of PV active power are chosen as

$$P_{PV}^{i,(k)} = P_{PV}^{i,(k)}.\left[1 - \frac{V_{PV}^{i,(k)} - 1.05}{1.058 - 1.05}\right] \quad . \tag{4.13}$$

If overvoltage persists for a predefined period, LTC steps down the tap position in order to achieve voltage regulation within operating voltage range (0.95-1.05 p.u.).

4.5.3.2 Undervoltage Control

Referring to (4.8), the PV inverter provisioned its maximum reactive power if its terminal voltage has reached the lower bound. Typical actions taken to push the voltage back to the normal range include upstream capacitor switching (if any) and LTC/regulator step-up voltage regulation to increase voltage.

4.5.3.3 LTC Operation Control

The primary purpose of an LTC transformer is to keep voltage on the low voltage side of the power transformer within the standard regulatory range. LTC control strategies include [32] setting fixed

voltage at the transformer's low voltage side, using a line-drop compensator, measuring local power flow, and utilizing remote voltage measurements. In this study, the latter strategy is applied based on minimum and maximum voltage measured at the PCC.

The control method initiates a time delay counter (T_t) that counts up when the measured remote voltage is out of standard regulatory bound and counts down to zero when the measured remote voltage is in bound.

$$T_t = \begin{cases} \max(0, T_t - 1) & , if\ V_{min} \leq V_{PV}^{i,(k)} \leq V_{max} \\ T_t + 1 & , otherwise \end{cases} \quad (4.14)$$

The primary purpose of a timer is to provide a time delay (T_D) to prevent unnecessary LTC operations due to temporary voltage fluctuations. Once T_t becomes greater than T_D, a control pulse is sent to the LTC mechanism in order to move the tap up or down by one position.

$$Tap = \begin{cases} Tap + 1 & , if\ V_{max} < V_i(k)\ , T_t > T_D \\ Tap - 1 & , if\ V_i(k) < V_{min}\ , T_t > T_D \end{cases} \quad (4.15)$$

The time delay is set to 50 seconds in this research [32].

4.5.3.4 Coordination between States

A coordinated control is required in order to achieve the desired objectives in each state and mitigate the adverse impact of high penetration of PV on power quality while reducing operation of LTC,. In the proposed coordination scheme, PV active power variations and terminal bus voltage are used to determine the PV inverter operating state. If the current state is 1 and PV power intermittency begins, operational control for state 2 is triggered. While reactive power support continues during PV power fluctuations, the inverter tracks both the voltage at the PCC and PV power variations. If voltage violation occurs for the past 10 seconds and PV power variation $(\Delta P_{PV}^{i}/dt) > \varepsilon$ remains, then PV operational control transitions from state 2 to state 3. If the current state is 3 and PV power fluctuation is detected, the control for state 2 is activated. Meanwhile, voltage at the PCC and PV power variations are monitored. If voltage violation is not present in the past 10 seconds and $(\Delta P_{PV}^{i}/dt) > \varepsilon$, the control in state 2

continues. If $\left(\Delta P_{PV}^{i}/dt\right) < \varepsilon$, operational control transitions from state 2 to state 1. The transition to state 2 is fast in order to cancel out or smooth voltage fluctuations caused by power intermittency of the PV inverters. For transitions from state 2 to states 1 and 3, however, a reactive power ramp rate limiter (ε_Q) is needed to prevent additional voltage fluctuations caused by reactive power swings from state to state transitioning.

$$Q_{PV}^{i}(k) = \begin{cases} Q_{PV}^{i,(k)}, if\ |Q_{PV}^{i,(k)} - Q_{PV}^{i,(k-1)}| < \varepsilon_Q \\ \left(Q_{PV}^{i,(k-1)} + \varepsilon_Q\right)\sigma + Q_{PV}^{i,(k)}(1-\sigma), otherwise \end{cases} \tag{4.16}$$

Because out-of-bound voltage could trigger the LTC operation, a reactive power injection rate (σ) is added to provide a trade-off between smooth reactive power variation and tap changing prevention.

$$\sigma = \frac{T_D - T_t}{T_D} \tag{4.17}$$

The σ value close to 1 represents a situation in which LTC is less likely to operate, so reactive power injection could smoothly change to the desired calculated value ($Q_{PV}^{i}(k)$). As σ approaches 0, the LTC is more likely to operate; therefore, the inverter injects the desired calculated reactive power ($Q_{PV}^{i}(k)$) depending on the state of operation.

Figure 4.7 shows the flowchart for the proposed coordinated reactive power and voltage control scheme for the PV inverter and LTC operation.

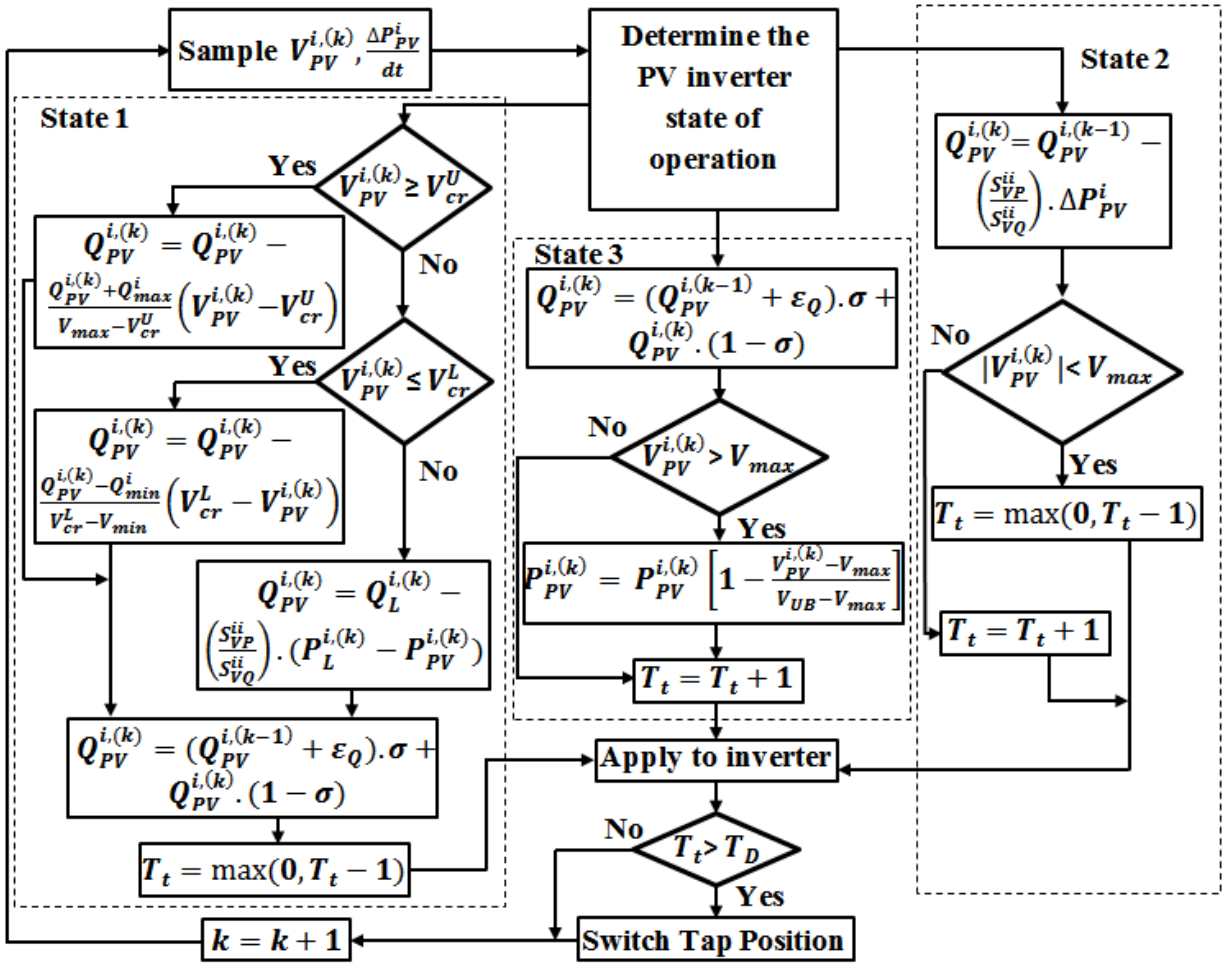

Figure 4.7 Flowchart of the proposed reactive power control strategy.

4.6 Numerical Studies

In order to provide a proof-of-concept, the effect of oversized inverter and the proposed voltage fluctuation mitigation method on a small-scale network was initially investigated in this research. In addition, the full mathematical concept presented in Section 4.5 was applied on the developed test case feeder.

4.6.1 Small-Scale Network Description

The case study is the modified IEEE 37 node test feeder shown in Figure 4.8. The system is a three-phase feeder with multiple single phase, two- and three-phase loads. It is assumed that system load is star-connected and comprised of residential customers on each feeder. The extended pole to pole lines

of primary feeder (from node 32 to 42) is wired with #1 cable. Distances between poles are 250 ft. Each pole distributes energy by a pole mounted transformer to a neighborhood consisting of four homes. It is a single-phase transformer with rating of 25 kVA, 4.8kV-120/240V, X=%2.3, R=%1.6 [86]. Each home is connected to the secondary circuit of single-phase transformer through triplex overhead drop cable 4/0 AAC [87] of length 90 ft.

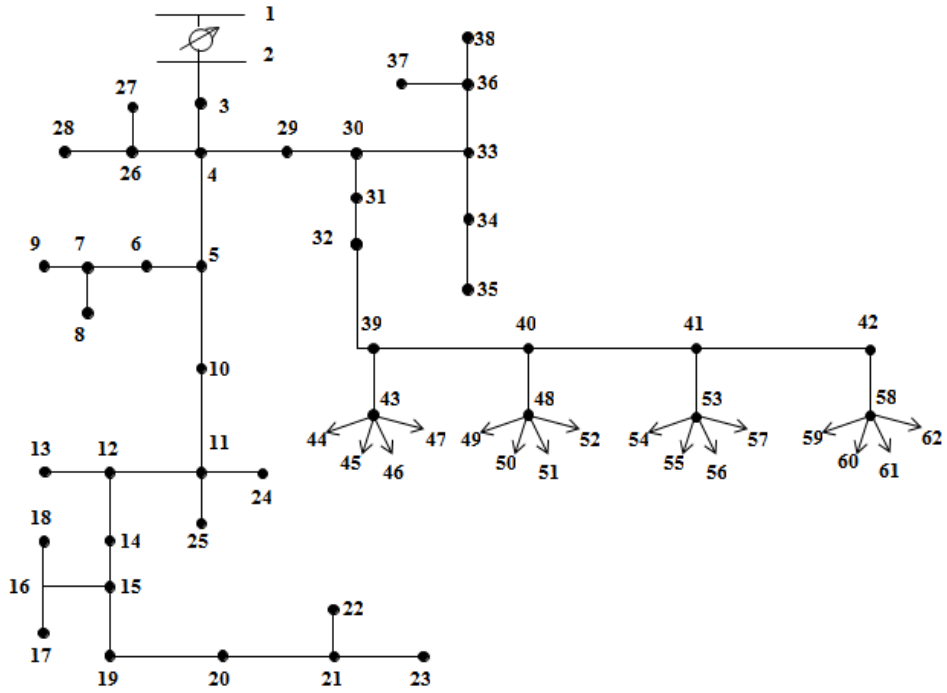

Figure 4.8 Modified IEEE 37 node test feeder.

Home load data were extracted from the eGauge website [89], which provides load data with up to 1-minute resolution. Typical home data is shown in Figure 4.9. Load reactive power is defined in proportion to the real load connected at the same bus with a power factor of 0.9 lagging. The 1-second resolution PV generation is obtained from NREL data measured from a station near Hawaii's Honolulu International Airport on the island of Oahu [34]. Global Horizontal Irradiance is shown in Figure 4.9 which includes both the clear sky and transient cloud movement periods. The assumption was made that the nodes were geographically close in the network such that outputs of PV units follow the same generation pattern. The grid-connected PV/inverter system is considered to inject all real power produced

to the grid; therefore, for simulation, it is represented as negative constant power load. The amount of reactive power is determined by (4.12) subject to constraints imposed by (4.1) and (4.2). Homes with rooftop PV are located at nodes 44, 49, 54, and 59.

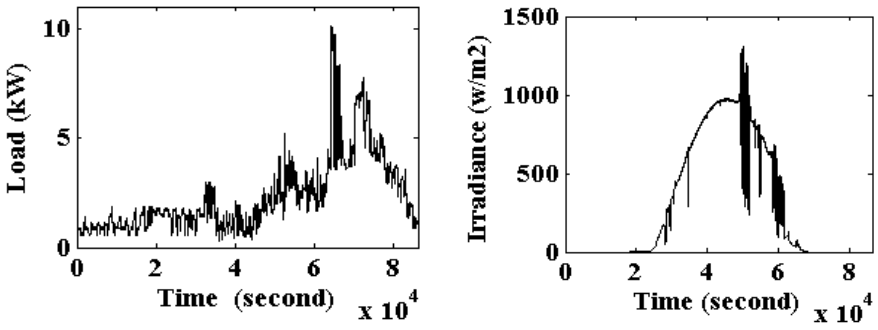

Figure 4.9 Typical home data (left) and global horizontal irradiance (right).

4.6.2 Preliminary Results and Effect of Oversized Inverter

Two numerical examples based on different inverter capacities are studied and compared to the case using old IEEE Std. 1547 for reactive power control of solar PVs (i.e. no reactive power injection at low voltage level). Simulations are done for December 11, 2010, from 11:00 a.m. to 12:00 p.m. The full three-phase model of the network is developed in MATLAB. Inverters are set to provide reactive power up to 0.8 power factor.

Figure 4.10 shows voltages at node 59 with and without proposed control approach while the inverter rating is set to the PV rating. As shown in the figure, significant fluctuations in voltage are damped using the proposed method in comparison to no control method.

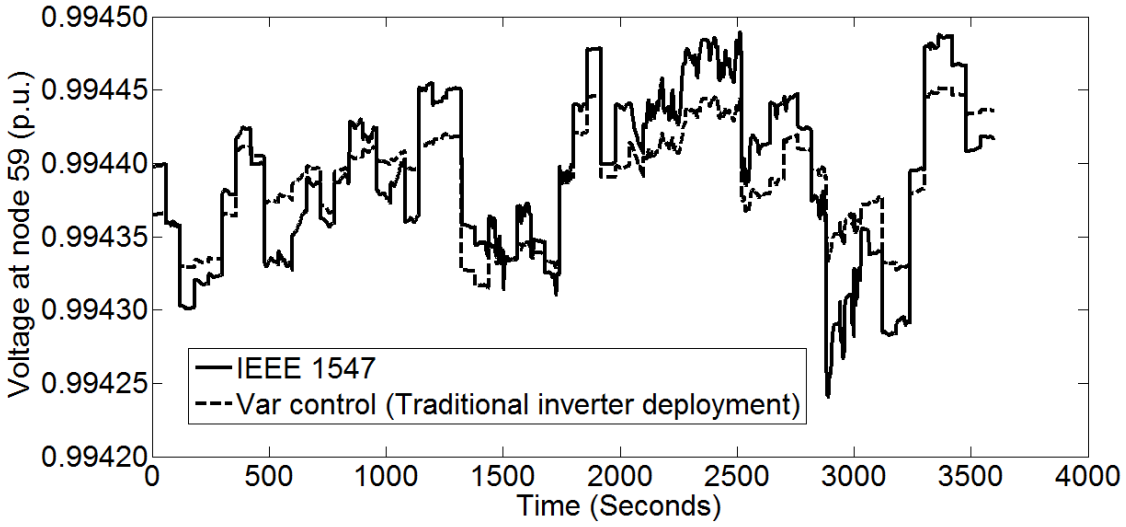

Figure 4.10 Voltages at node 59 using old IEEE Std. 1547 and inverter deployment

A simulation based on inverter oversized by 20% is performed to show the effects of oversized inverter on voltage profile. Voltage at node 59 is depicted in Figure 4.11, demonstrating that voltage variation further decreased due to implementation of the oversized inverter.

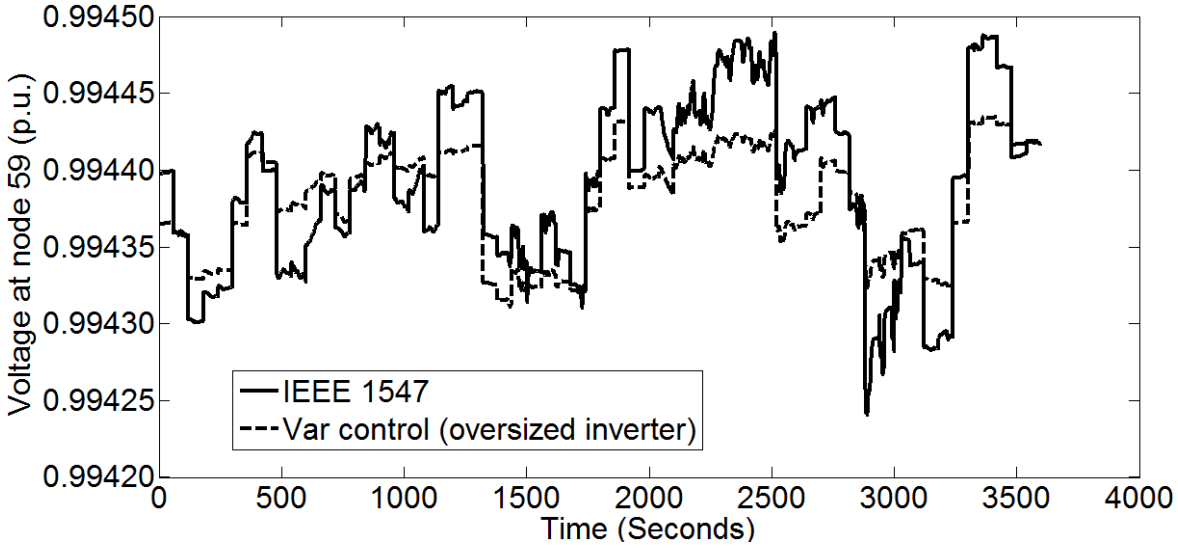

Figure 4.11 Voltages at node 59 using IEEE Std. 1547 and oversized inverter

In order to check the validity and highlight the effects of oversizing the inverter on system voltage, the bus voltage fluctuation index (VFI) is defined as the summation of voltage magnitude change between the current and previous time slice at each bus for the duration of the simulation.

$$VFI = \sum_{k=1}^{M} |V_i(k) - V_i(k-1)| \tag{4.18}$$

where M is the number of time steps of 1 second. For the small system study, M = 3600 was used. The maximum VFI observed over 11 a.m. to 12 p.m using the old IEEE Std. 1547, traditional and oversized inverters are shown in Table 4.1.

Table 4.1 Maximum VFI observed using old IEEE Std. 1547, traditional, and oversized inverter.

Maximum VFI		
IEEE 1547 (No control)	Traditional inverter	20% oversized inverter
0.0037	0.0018	0.0017

Results show that maximum VFI is the highest using the old IEEE Std. 1547 approach and that VFI could be significantly reduced using the proposed var control approach. Maximum VFI decreased by 54% compared to the old IEEE Std. 1547 method using oversized inverters. In order to gain insight into the problem, Figure 4.12(a) and Figure 4.12(b) show Global Horizontal Irradiance from 11:00 a.m. to 12:00 p.m and system voltages at node 59 using traditional and oversized inverter deployment. It can be observed that the voltages in both approaches are the same till around first 1200 seconds. Referring to Figure 4.12(a), it is mainly because the PV active power is less than 80% of P_{max}. As PV operates near its full capacity (beyond 80% of P_{max}), the inverter rating limits the reactive power injection in the traditional deployment approach, while this constraint is not active in the oversized inverter approach,. However, the difference between the two cases is very small.

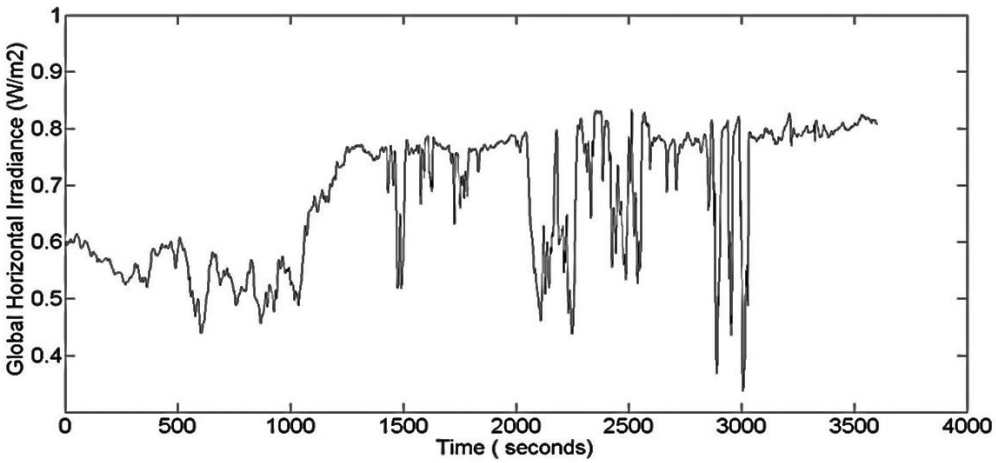

(a)

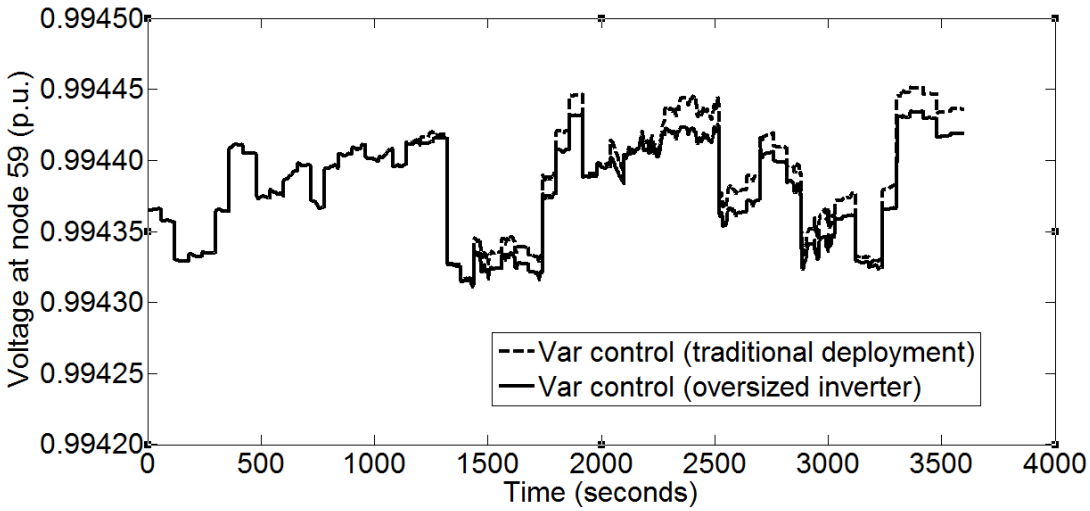

(b)

Figure 4.12 (a) Global Horizontal Irradiance and (b) voltages at node 59 using traditional and oversized inverter deployment.

Overall, results show that while traditional deployment and sizing the inverter to PV capacity outperforms the old IEEE Std. 1547 approach, using oversized inverters and implementing the variable var approach demonstrates further improvements in voltage fluctuation control problem. In order to confirm the efficacy of the proposed approach, the method was tested on a three-phase unbalanced large-scale network in the next subsection.

4.6.3 Large-Scale Network Description

A distribution network based on IEEE 37 node test feeder is developed to investigate performance of the proposed PV inverter operational strategy. Figure 4.8 shows the modified IEEE 37 node test feeder in which the extended network is modeled by lines branching out of primary feeder 32 (i.e., from node 39 to 42). The assumption was made that each distribution transformer distributes power to a neighborhood consisting of four homes. Characteristics of transformers and service drop cables are described in detail in [19]. All nodes in the original IEEE 37 node test feeder are extended using the same analogy.

The modified system consists of 559 nodes and 144, 144, and 160 homes in phase A, B, and C, respectively. PV-enabled homes are selected randomly in each phase with 50% PV penetration per phase. In particular, PV-enabled homes in the extended feeder are located at nodes 44, 46, 52, 55, 56, 57, 59, 60, 61, and 62. LTC tap position ranges from 0.95 to 1.05 with tap step of 0.01. In order to select ε parameter, the PV output power ramp-rate is measured during slow variations. We observed that more than 99% of the ramp-rates were less than 15 W/s. Therefore, ε is set slightly higher than that to 20 W/s. The ε_Q parameter is set to 50% of the var available based on heuristic. If larger values are selected, additional voltage fluctuations could occur due to large reactive power swings because of state-to-state transitioning. Conversely, selecting smaller values could degrade performance of the proposed control strategy in damping voltage fluctuations because only a small capacity of inverter for reactive power injection/absorption will be used. In addition, inverters are assumed to be oversized by 20% and provide reactive power up to 0.8 power factor.

4.6.4 Large-Scale Network Simulation

A three-phase unbalanced power flow was developed in MATLAB in order to implement the proposed scheme. Results from the developed program for the test system with no controls were verified with results obtained from OpenDSS [109]. Because the control time step should be granular enough to

capture dynamic interactions among PV inverters and LTC in various operational states, test results were obtained by sequentially running load flow and implementing the proposed scheme over a period of one day. The proposed control strategy was compared to the following PV control strategies: 1) unity power factor, 2) $cos\varphi(P)$ control, and 3) $Q(V)$ control. Voltage sensitivity coefficients for all nodes with solar PV are presented in descending order in Figure 4.13. Values of Svp ranged from 0.1366 to 0.0759, and values of Svq ranged from 0.0606 to 0.0238. Because the voltage did not exceed the upper limit of 1.042 p.u. in the simulations, overvoltage control mentioned in (4.13) was not triggered.

For illustration, a zoomed-in plot of varying irradiance from Figure 4.9 (b) is used to show results with tap operation in Figure 4.14 to Figure 4.16. Figure 4.14 shows PV active power and reactive power generation for 500 seconds and state transitioning for the PV inverter. Figure 4.15 (a) shows voltage at bus 439 and the tap changer operation with and without the proposed PV inverter reactive power control strategy.

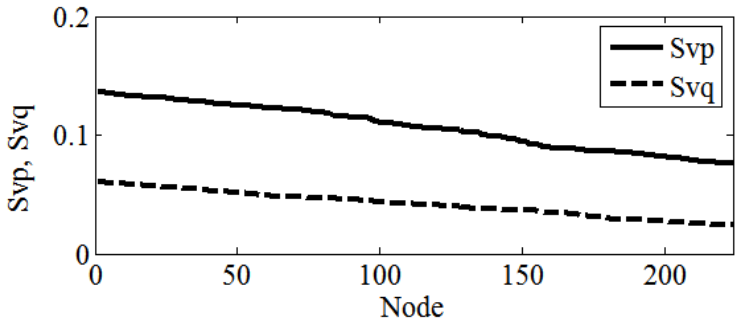

Figure 4.13 Voltage sensitivity coefficients.

The proposed strategy effectively mitigates voltage fluctuations when the PV inverter operates in state 2 and provides voltage support when it operates in state 1. Furthermore, operation in state 3 requires only one tap operation within the zoomed-in study period in order to push voltage into the range, whereas the unity power factor control requires two tap operations.

The proposed reactive power control strategy has also been compared to the $cos\varphi(P)$ and $Q(V)$ control methods, as shown in Figure 4.15 (b) and Figure 4.15 (c). Notice that the $cos\varphi(P)$ method

consumes reactive power in high feed-in power periods and provides no reactive power provisioning for the rest of the simulation time. In fact, the $cos\varphi(P)$ strategy only considers the weather condition (solar irradiance) in order to enforce reactive power support; it simply assumes that grid voltage increases in high solar irradiance periods regardless of load variation. As a result, the control method fails to mitigate voltage fluctuations caused by moving clouds and provides poor performance during high PV generation periods by causing voltage drop, thereby triggering the tap operation more than that of other methods (Figure 4.15 (b) and Figure 4.16).

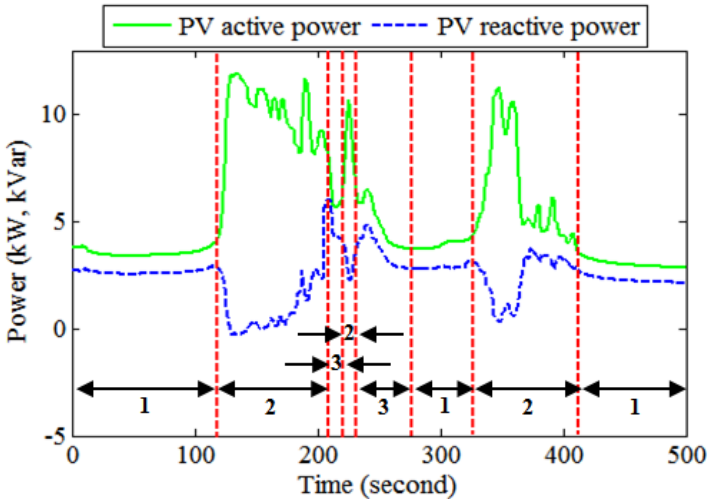

Figure 4.14 PV active power and reactive power generation.

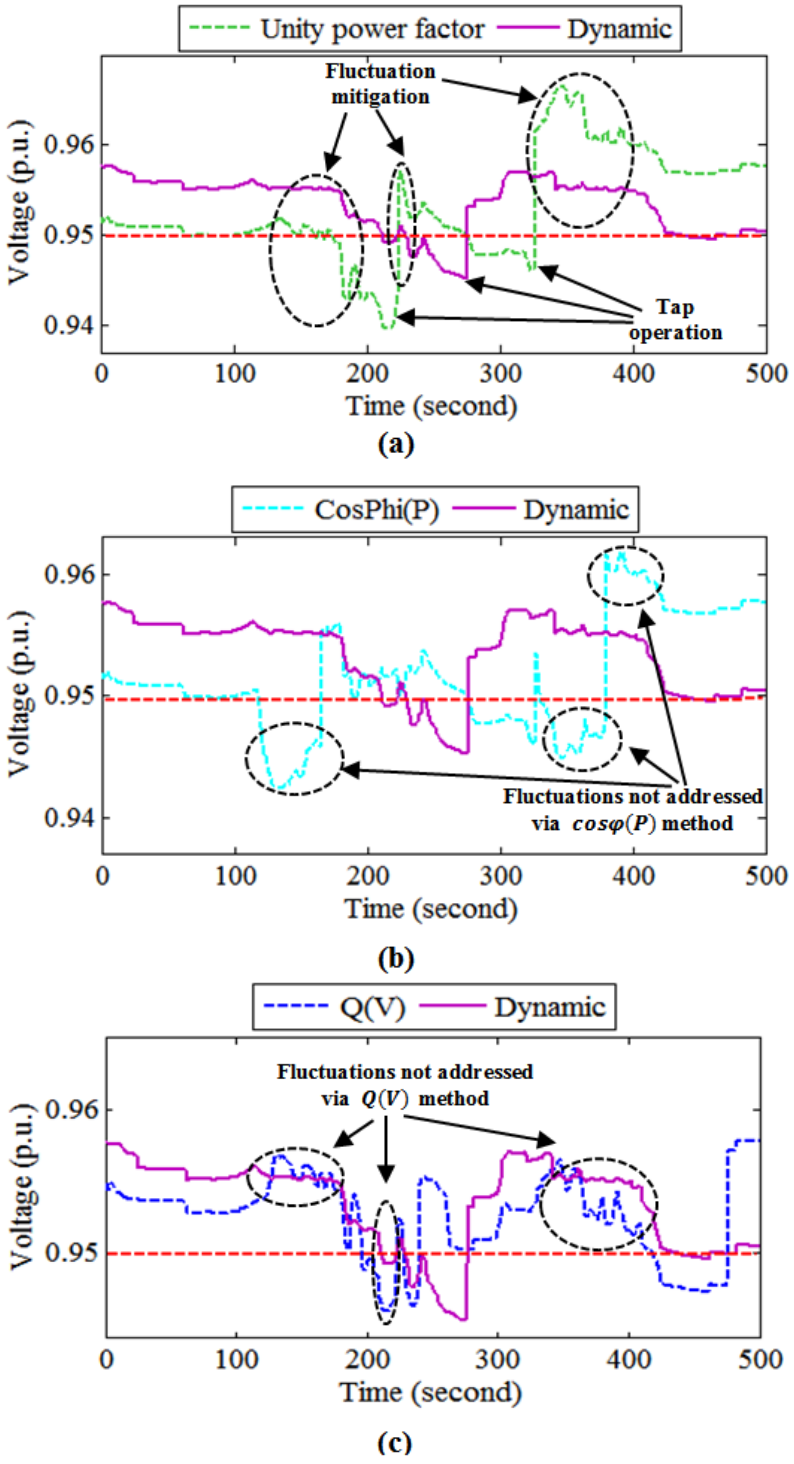

Figure 4.15 Effect of the proposed approach on tap operation and voltage at bus 439. (a) voltage profile with and without the proposed approach, (b) comparison of voltage with the cosφ(P) method, and (c) comparison of voltage with the Q(V) method.

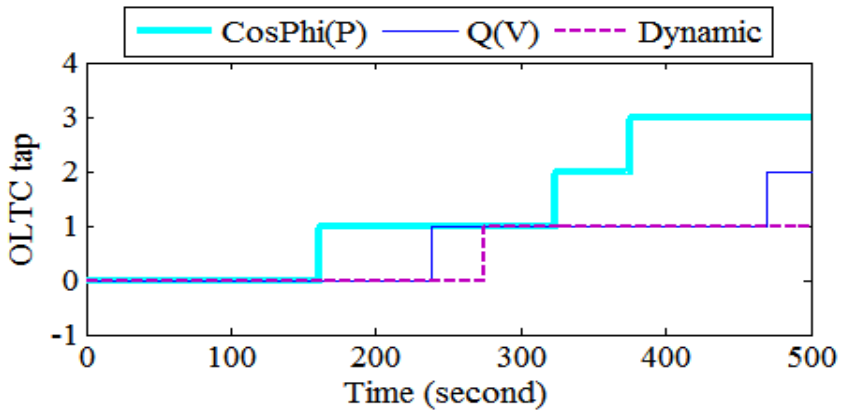

Figure 4.16 Tap operation with cosφ(P), Q(V), and proposed methods.

Although the $Q(V)$ strategy is basically designed to prevent voltage violation, it could not mitigate voltage violation, as shown in Figure 4.15 (c), because only PV inverters with terminals voltages outside the predefined range (i.e., 0.958-1.042) provide reactive power provision in this strategy. Therefore, only some PV inverters provide reactive power support based on their terminal voltage. In addition, the $Q(V)$ strategy could not address voltage fluctuation.

In contrast to the $cos\varphi(P)$ and $Q(V)$ control methods, all PV inverters in the proposed approach contribute via reactive power support in order to achieve the goal associated with their state of operation as determined by solar irradiance variation and terminal voltage. The proposed strategy is a perfect match to react when the PV output is subject to rapid variation due to scattered clouds passing over the system. The proposed approach also offers voltage support during cloud shadows with low PV generation and prevents voltage violation via dynamic reactive power injection. Although the number of LTC operation within the zoomed-in study period is 2 for the unity power factor and $Q(V)$ control strategies and 3 for the $cos\varphi(P)$ control strategy, the tap operation is reduced to 1 for the proposed approach.

4.6.5 Performance Analysis

For quantitative comparison, whole-day simulations using the investigated PV inverter reactive power control methods are summarized in Table 4.2 and Figure 4.17. Performance metrics include

maximum voltage deviation (MVD) from nominal voltage limits, total power losses, and the number of LTC tap operations. In addition, the VFI is calculated using M = 86400 for the large system study.

Table 4.2 Daily power losses, number of LTC operations and MVD via unity power factor, cosφ(P), Q(V), and dynamic Adproaches.

Strategy	MVD (p.u.)	P^{a}_{Loss} (kW)	P^{b}_{Loss} (kW)	P^{c}_{Loss} (kW)	Number of Tap Changing
Unity PF	0.0603	561.2558	314.3696	616.0510	3
cosφ(P)	0.0575	573.8045	319.3013	629.4589	3
Q(V)	0.0551	561.3742	314.3087	615.8080	3
Dynamic	0.0545	548.61383	307.8721	596.5811	2

As shown in Table 4.2, without control (unity power factor method as base case), PV output variations cause significant voltage deviation in bus voltages. In particular, MVD experienced at bus 439 as voltage drop is 0.0603 p.u. and the number of LTC operations are 3.

Application of the $cos\varphi(P)$ method results in 3 tap operations throughout the day, while MVD is 0.0575 p.u. at bus 439. Moreover, power losses in the ABC phases increase 2.24%, 1.57%, and 2.18%, respectively. When the $Q(V)$ control strategy is used, the bus voltage at node 439 exhibits MVD of 0.0551 p.u., and power losses in the ABC phase are slightly decreased by 0.47%, 0.28%, and 0.5% with respect to the base case. Three tap operations are recorded for this strategy. The proposed dynamic approach is the case in which performance metrics show maximum improvement. In the proposed approach, MVD experienced at bus 439 improves from 0.0603 p.u. to 0.0545 p.u.; power losses decreased to 2.5%, 4.06%, and 3.93% in respective phases, and the numbers of LTC operations decrease to 2. Compared to other strategies, power losses decreased because PV generation is matched to load consumption a majority of the time.

Figure 4.17 displays the VFI at selected buses; i.e., PV-enabled homes at bus 439 (connected to phase A) and bus 11 (three phase bus). When the unity power factor method is utilized, VFI at bus 439 is

0.6375 p.u., whereas VFI at bus 11 in ABC phases are 0.4263 p.u., 0.2027 p.u., and 0.2915 p.u., respectively. With the $cos\varphi(P)$ control, VFI at bus 439 and phase A of bus 11 is decreased 18.86% and 13.6%, while VFI is increased by 52.45% and 39.6% at bus 11 of phase B and C, respectively. VFI associated with the $Q(V)$ control in bus 439 (phase A) and 11 (ABC phase) are decreased 4.62%, 4.03%, 1.85%, and 0.03%, respectively. When the proposed strategy is implemented, VFI values at bus 439 (phase A) and 11 (ABC phase) are effectively decreased 45.93%, 50.18%, 11.48%, and 14.82%, respectively.

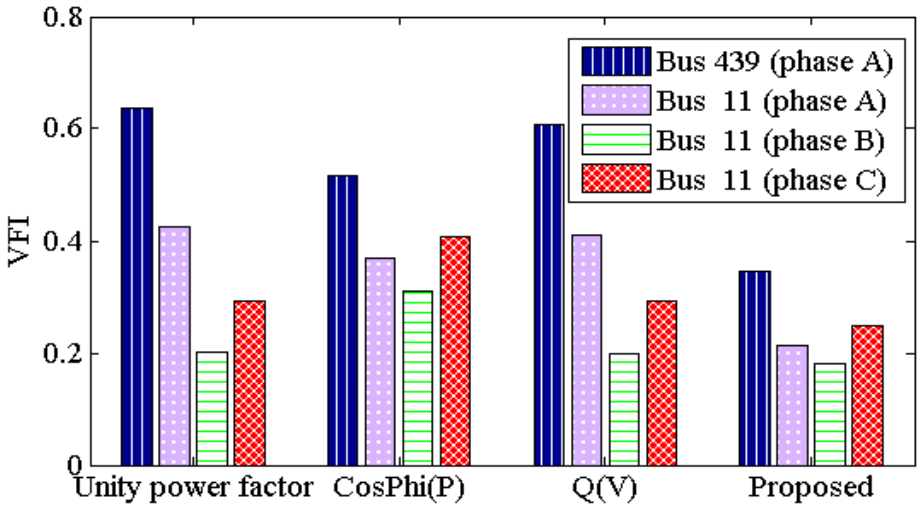

Figure 4.17 VFI at buses 11, 439 via unity power factor, cosφ(P), Q(V) and proposed methods

Results shown above are based on setting upper and lower critical voltages to 1.042 p.u. and 0.958 p.u., respectively. We consider it the base case with total power losses of 1453.067 kW and MVD of 0.0545 p.u. In order to examine the effect of these limits on the results with the proposed dynamic approach, two additional cases are studied; 1) the upper and lower critical voltages are set to 1.034 p.u. and 0.964 p.u., respectively; and 2) the upper and lower critical voltages are set to 1.046 p.u. and 0.954 p.u., respectively. Compared to the base case, no significant change in VFI and no change in the number of tap operations was observed for both Case 1 and Case 2. MVD decreased to 0.0539 p.u. and total power losses increased to 1468.132 kW for Case 1, but in contrast, MVD increased to 0.0549 p.u. and

total power losses decreased to 1449.961 kW for Case 2. However, these changes are very small compared to the base case and do not have significant impact on the control scheme.

4.7 Summary

This chapter presented a dynamic PV inverter reactive power control scheme to facilitate high penetration of rooftop PV in distribution systems under a variety of weather conditions. Three states of operation for PV inverters were proposed using irradiance variation and voltage measurement at the PCC. In the normal state, the scheme was designed to provide loss reduction support while supporting load demand when irradiance changed slowly. In the fluctuating state, reactive power was modulated to mitigate voltage fluctuations caused by transient cloud movement. The control offered reactive power support to mitigate voltage violation defined for the contingency state. A reactive power ramp rate limiter was introduced to prevent additional voltage fluctuations due to reactive power variation caused by switching between the states. A coordination strategy was proposed to switch control between the states and manage interaction between fast PV inverter controllers and slow OLTC for voltage regulation. Numerical tests on a modified IEEE 37 node test feeder demonstrated that the proposed approach is advantageous compared to the unity power factor, the $cos\varphi(P)$, and the $Q(V)$ reactive power control strategies. The proposed approach also improved the operational performance of distribution systems with high rooftop PV penetration. Results demonstrated superior performance of the proposed approach for reducing the number of OLTC operations, decreasing power losses, smoothing out voltage fluctuations, and mitigating voltage violation in the LV grid.

5 Stochastic Multi-Authority Energy Management of Distribution Systems Incorporating DSO and Multi-MGs with Correlated Wind Generators

5.1 Introduction

Power distribution systems are transitioning from a system with single distribution system operator (DSO) to a more integrated flexible network that incorporates multiple microgrids (MGs). With development of MGs, energy management of power distribution systems is becoming a challenging task. DSO and MG may have different owners and schedule renewable and non-renewable DERs based on their own economic rules and policies. However, secure and economic operation of the entire system is necessary. Moreover, renewable DERs such as wind generators (WGs) are essentially intermittent and spatially correlated in the geographical area that encompasses DSO and MGs as these entities are influenced often by the same wind levels.

This chapter presents a novel stochastic framework to investigate the impact of correlated WGs on energy management of DSO and MGs. The proposed framework defines DSO and MG as independent entities with their own regulations and optimization formulation. Since DSO and MG are working in an interconnected system, the proposed framework decomposes the optimization formulation of each entity while accounting for the interconnected operation of DSO and MG via information exchange between the entities. A distributed optimization is developed to solve the optimization problem of each entity and to optimally operate the entire system. In order to decouple the problem formulation in DSO and MGs, a linear approximation is proposed which enables parallel processing of the optimization problems. We study the energy management of DSO and MGs with consideration of uncertainties in both load and wind power generation using the point estimate method (PEM) [84]. Further, an improved point estimate

method (PEM) is proposed to model the uncertainties in load and wind generation and account for the statistical correlations among wind generators. The proposed method is applied to a modified IEEE 69 bus test feeder and the results are validated in terms of efficiency and accuracy. Solar generation is not included in this chapter, but it can be included using an approach similar to that used for WGs.

5.2 Energy Management Model of DSO and MG

Assume that a transmission system operator (TSO) interacts with a power distribution system which is comprised of a DSO and *n* MGs, as shown in Figure 5.1. In order to formulate energy management and coordination among MGs and DSO, a mathematical model of each entity is required. The aim is to organize network models into a bi-level hierarchy in which DSO and MGs are located in upper and lower levels of the hierarchy, representing super-network and sub-networks that are optimized to match targets passed from DSO and responses from MGs [76]. Optimization problems are formulated and solved autonomously for the DSO and the MGs according to resources, physical coupling link, and shared information between individual entities.

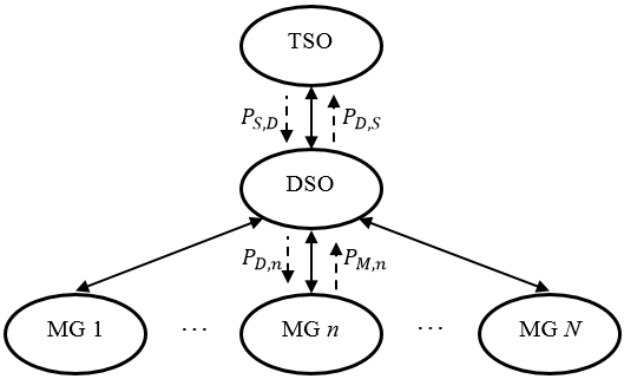

Figure 5.1 Hierarchical physical connection of DSO and MGs.

5.2.1 Optimization Formulation for DSO

Let D indicates the set of nodes in DSO grid and φ_D denotes the set of nodes in D that are connecting border lines between DSO and MGs. Detailed mathematical optimization the DSO is formulated as follows:

$$\min f_D = C_D^T P_D^T - C_T^D P_T^D + \sum_{n\in\varphi}(C_n^M P_n^M - C_n^D P_n^D) + \sum_{i\in D}(C_i^{DG} P_i^{DG} - C_i^L P_i^L) \quad (5.1)$$

s.t.

Power balance constraints on the substation, $\forall j \neq 1$:

$$P_D^T + P_1^{DG} + P_1^{WG} - P_1^L = \sum_j V_1 V_j Y_{1j} \cos(\delta_1 - \delta_j - \theta_{1j}) \quad (5.2)$$

$$Q_D^T + Q_1^{DG} + Q_1^{WG} - Q_1^L = \sum_j V_1 V_j Y_{1j} \sin(\delta_1 - \delta_j - \theta_{1j}) \quad (5.3)$$

$$P_D^T = P_T^D \quad (5.4)$$

$$Q_D^T = Q_T^D \quad (5.5)$$

Voltage magnitude and angle limit for the substation (reference bus):

$$V_1 = 1 \quad (5.6)$$

$$\theta_1 = 0 \quad (5.7)$$

Power balance constraints on buses in the DSO ($\forall i, j \in D$):

$$P_i^{DG} + P_i^{WG} - P_i^L = \sum_j V_i V_j Y_{ij} \cos(\delta_i - \delta_j - \theta_{ij}) \quad (5.8)$$

$$Q_i^{DG} + Q_i^{WG} - Q_i^L = \sum_j V_i V_j Y_{ij} \sin(\delta_i - \delta_j - \theta_{ij}) \quad (5.9)$$

Power balance constraints on buses having borderlines with MG ($\forall n \in \varphi_D$):

$$P_n^M + P_n^{DG} + P_n^{WG} - P_n^L = \sum_{j\notin\varphi_D} V_n V_j Y_{nj} \cos(\delta_n - \delta_j - \theta_{nj}) \quad (5.10)$$

$$Q_n^M + Q_n^{DG} + Q_n^{WG} - Q_n^L = \sum_{j\notin\varphi_D} V_n V_j Y_{nj} \sin(\delta_n - \delta_j - \theta_{nj}) \quad (5.11)$$

$$P_n^D = P_n^M \quad (5.12)$$

$$Q_n^D = Q_n^M \quad (5.13)$$

Other constraints:

$$V_{min,i} \leq V_i \leq V_{max,i} \quad , \forall i \in D, \forall i \in \varphi_D, i \neq 1 \quad (5.14)$$

$$-\pi \leq \theta_i \leq \pi \quad , \forall i \in D, \forall i \in \varphi_D, i \neq 1 \quad (5.15)$$

$$P_{ij}{}^2 + Q_{ij}{}^2 \leq S_{max}^{ij}{}^2 \quad , \forall i, j \in D, \forall i, j \in \varphi_D \quad (5.16)$$

$$P_{min,i}^{DG} \le P_i^{DG} \le P_{max,i}^{DG} \quad ,\forall i \in D, \forall i \in \varphi_D \qquad (5.17)$$

$$Q_i^{DG} = \cos(\tan^{-1} PF) \quad ,\forall i \in D, \forall i \in \varphi_D \qquad (5.18)$$

$$0 \le P_i^{WF} \le P_{max,i}^{WF} \quad ,\forall i \in D, \forall i \in \varphi_D \qquad (5.19)$$

$$Q_i^{WF} = \cos(\tan^{-1} PF) \quad ,\forall i \in D, \forall i \in \varphi_D. \qquad (5.20)$$

The optimization variables of problem (5.1) are local DSO variables, $\bar{\mathbf{x}}_D = [P_i^{DG}, Q_i^{DG}, V_i, \delta_i, P_D^T, Q_D^T, P_T^D, Q_T^D]$ and coupling variables between DSO and MGs, $\mathbf{y} = [P_n^D, Q_n^D, P_n^M, Q_n^M]$, $\forall n$. The objective function (5.1) is the expected cost of DSO operation. The first row in (5.1) represents the cost and revenue of bilateral transactions between TSO and DSO as well as DSO and MGs, respectively. The second row includes the cost of generation from DGs, and revenue of selling power to customers in the DSO grid, respectively. In the above formulation, (5.2)-(5.5) are distribution power flow equations for the substation bus, (5.6) and (5.7) are voltage magnitude and angle limits on the substation (reference bus), and (5.8) and (5.9) are power balance equations for buses in the DSO. Constraints (5.10)-(5.13) are distribution power flow equations for the border lines with MGs and constraints (5.14) and (5.15) are voltage magnitude and angle limit for buses except reference bus. Constraint (5.16) imposes line thermal limits, and (5.17)-(5.20) represent active/reactive power limits of DGs and WGs.

5.2.2 Optimization Formulation for MG

Similarly, let M denotes the set of nodes in MG grid and φ_M defines the set of nodes in M that are connecting border lines between MG and DSO. The optimization problem for the generic MG *n* is formulated as follows:

$$\min f_{MG,n} = C_n^D P_n^D - C_n^M P_n^M + \sum_{i \in M} (C_i^{DG} P_i^{DG} - C_i^L P_i^L) \qquad (5.21)$$

s.t.

Power balance constraints on buses having borderlines with DSO ($\forall n \in \varphi_M$):

$$P_n^M + P_n^{DG} + P_n^{WG} - P_n^L = \sum_{j \notin \varphi_M} V_n V_j Y_{nj} \cos\left(\delta_n - \delta_j - \theta_{nj}\right) \qquad (5.22)$$

$$Q_n^M + Q_n^{DG} + Q_n^{WG} - Q_n^L = \sum_{j \notin \varphi_M} V_n V_j Y_{nj} \sin\left(\delta_n - \delta_j - \theta_{nj}\right) \tag{5.23}$$

$$P_n^D = P_n^M \tag{5.24}$$

$$Q_n^D = Q_n^M \tag{5.25}$$

Power balance constraints on buses in the MG ($\forall i, j \in M$):

$$P_i^{DG} + P_i^{WG} - P_i^L = \sum_j V_i V_j Y_{ij} \cos\left(\delta_i - \delta_j - \theta_{ij}\right) \tag{5.26}$$

$$Q_i^{DG} + Q_i^{WG} - Q_i^L = \sum_j V_i V_j Y_{ij} \sin\left(\delta_i - \delta_j - \theta_{ij}\right) \tag{5.27}$$

Other constraints:

$$V_{min,i} \le V_i \le V_{max,i} \qquad , \forall i \in M, \forall i \in \varphi_M \tag{5.28}$$

$$-\pi \le \theta_i \le \pi \qquad , \forall i \in M, \forall i \in \varphi_M \tag{5.29}$$

$${P_{ij}}^2 + {Q_{ij}}^2 \le {P_{max}^{ij}}^2 \qquad , \forall i, j \in M, \forall i, j \in \varphi_M \tag{5.30}$$

$$P_{min,i}^{DG} \le P_i^{DG} \le S_{max,i}^{DG} \qquad , \forall i \in M, \forall i \in \varphi_M \tag{5.31}$$

$$Q_i^{DG} = \cos(\tan^{-1} PF) \qquad , \forall i \in M, \forall i \in \varphi_M \tag{5.32}$$

$$0 \le P_i^{WF} \le P_{max,i}^{WF} \qquad , \forall i \in M, \forall i \in \varphi_M \tag{5.33}$$

$$Q_i^{WF} = \cos(\tan^{-1} PF) \qquad , \forall i \in M, \forall i \in \varphi_M. \tag{5.34}$$

The optimization variables are local MG variables, $\bar{\mathbf{x}}_{MG,n} = [P_i^{DG}, Q_i^{DG}, V_i, \delta_i]$, and coupling variables between DSO and MG n, $\mathbf{y}_n = [P_n^D, Q_n^D, P_n^M, Q_n^M]$. The first row in (5.21) presents the cost and revenue related to buying and/or selling power from/to DSO. The second row is the cost of generation from DGs, and revenue of selling power to customers in the MG grid, respectively. In the above formulation, (5.22)-(5.25) are distribution power flow equations for border lines with DSO, (5.26) and (5.27) are power balance equations for buses in the MG. Constraints (5.28) and (5.29) are voltage magnitude and angle limit for limits, (5.30) is line thermal limit, and (5.31)-(5.34) are active/reactive power limits of DGs and WGs.

It can be seen that optimization models are coupled through (5.12), (5.13), (5.24) and (5.25) as well as certain terms appearing in both DSO and MG objective functions, which prevents the optimization problems in DSO and MGs to be solved independently.

5.3 Distributed Energy Management Formulation

Future power distribution systems can be envisioned as multiple MGs connected to the grid as shown in Figure 5.2(a). Considering the coupling variables between DSO and generic MG *n*, general optimization for the DSO and MG *n* can be expressed as

$$\begin{aligned} &\min f_D(\bar{\mathbf{x}}_D, \mathbf{y}) \\ s.t.\ &\mathbf{g}(\bar{\mathbf{x}}_D, \mathbf{y}) = 0 \\ &\mathbf{h}(\bar{\mathbf{x}}_D, \mathbf{y}) \le 0 \\ &\mathbf{y} = [\mathbf{y}_1, \mathbf{y}_2, \cdots, \mathbf{y}_N] \end{aligned} \tag{5.35}$$

$$\begin{aligned} &\min f_{MG,n}(\bar{\mathbf{x}}_{MG,n}, \mathbf{y}_n) \\ s.t.\ &\mathbf{g}(\bar{\mathbf{x}}_{MG,n}, \mathbf{y}_n) = 0 \\ &\mathbf{h}(\bar{\mathbf{x}}_{MG,n}, \mathbf{y}_n) \le 0 \end{aligned} \tag{5.36}$$

where **g**, **h** are sets of equality and inequality constraints presented in Section 5.2, , and **y** is the set of coupling variables.

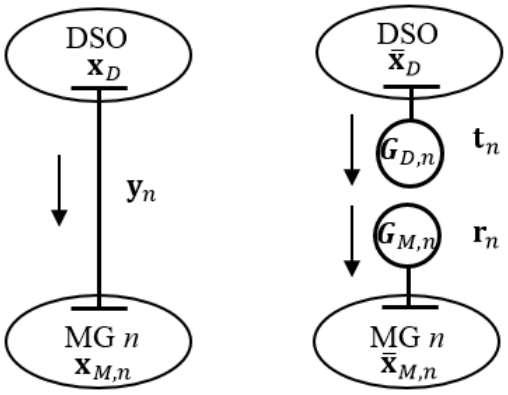

Figure 5.2 (a) Physical connection of DSO and MG, and (b) modeling target and response variables.

Coupling variables prevent problems (5.35) and (5.36) from being solved separately. In order to separate the optimization problems in two entities, the power balance in border lines are considered as

pseudo generators $G_{D,n}$ and $G_{M,n}$ from the perspective of DSO and MG *n*, respectively. Two sets of target ($\mathbf{t}_n = \mathbf{P}_n^D$) and response ($\mathbf{r}_n = \mathbf{P}_n^M$**)** variables are created as copies of $\mathbf{y}_n$**,** representing generated or absorbed active and reactive power from the pseudo generators as shown in Figure 5.2(b). The coupling constraint (5.31) enforces line flow balance on the border lines by matching targets and responses as

$$\mathbf{t}_n - \mathbf{r}_n = \mathbf{0} \ . \tag{5.37}$$

For the purpose of decomposition, the coupling constraint (5.37) is relaxed and moved into the objective functions (5.35) and (5.36) using an augmented Lagrangian penalty function.

$$\min f_D(\tilde{\mathbf{x}}_D) + \sum_{n=1}^{N} \lambda_n(\mathbf{t}_n - \mathbf{r}_n) + \|\mathbf{w}_n \circ (\mathbf{t}_n - \mathbf{r}_n)\|_2^2 \tag{5.38}$$

$$\min f_{MG,n}\left(\tilde{\mathbf{x}}_{MG,n}\right) + \lambda_n(\mathbf{t}_n - \mathbf{r}_n) \ + \|\mathbf{w}_n \circ (\mathbf{t}_n - \mathbf{r}_n)\|_2^2 \tag{5.39}$$

where $\tilde{\mathbf{x}}_D = [\bar{\mathbf{x}}_D, \mathbf{t}_1, \mathbf{r}_1, \dots, \mathbf{t}_N, \mathbf{r}_N]$ and $\tilde{\mathbf{x}}_{MG,n} = \left[\bar{\mathbf{x}}_{MG,n}, \mathbf{t}_n, \mathbf{r}_n\right]$, λ_n and $\mathbf{w}_n$ are Lagrange multiplier and penalty factor associated with the linear and quadratic terms, $\|\cdot\|_2^2$ represents the square of the l_2 norm, and symbol $\circ$ is the Hadamard product indicating component-wise multiplication of two vectors. Authors of [76] showed that inclusion of linear and quadratic penalty terms improves the speed of convergence.

Because $\mathbf{r}_n$ is constant with respect to the optimization problem in DSO and $\mathbf{t}_n$ is constant with respect to the optimization problem in MG *n*, the terms $\lambda_n\mathbf{r}_n$ and $\lambda_n\mathbf{t}_n$ can be removed from the linear terms in (5.38) and (5.39) as solution of the objective function will not be affected by a constant. However, $\mathbf{t}_n$ and $\mathbf{r}_n$ cannot be eliminated from $\|\mathbf{w}_n \circ (\mathbf{t}_n - \mathbf{r}_n)\|_2^2$ due to the cross-product terms $\mathbf{t}_n \circ \mathbf{r}_n$ included in the quadratic penalty terms. Resulting objective functions yield

$$\min f_D(\tilde{\mathbf{x}}_D) + \sum_{n=1}^{N} \lambda_n(\mathbf{t}_n) + \|\mathbf{w}_n \circ (\mathbf{t}_n - \mathbf{r}_n)\|_2^2 \tag{5.40}$$

$$\min f_{MG,n}\left(\tilde{\mathbf{x}}_{MG,n}\right) + \lambda_n(-\mathbf{r}_n) \ + \|\mathbf{w}_n \circ (\mathbf{t}_n - \mathbf{r}_n)\|_2^2 \ \ . \tag{5.41}$$

Once the optimization problem of DSO is solved, targets are communicated to MGs. MGs in turn use the targets assigned from DSO as fixed parameters in their own optimization problem. Once the optimization problems of MGs are solved, responses are provided to the DSO. Information is exchanged based on availability of data through an a priori agreement, for example, every 5 minutes. This process of information exchange is continued until target-response matching is achieved for the whole network. In the next section, solution approaches based on the above energy management model are discussed.

5.4 Solution Methodology

In this section, we first present the solution process based on the sequential computation algorithm. Then we discuss the parallel computation formulation, its implementation and convergence properties.

5.4.1 Sequential Computation Algorithm

The sequential computation method requires consecutive calculation of optimization problems in DSO and MG levels. The following steps illustrate the solution procedure to solve the distributed energy management problem that includes MGs:

Step 1. Set k =0, where k denotes the number of loop iterations. Initialize λ and $\mathbf{w}$ and choose initial values for $\mathbf{t}_n^k$ and $\mathbf{r}_n^k$, $n = 1, \dots, N$.

Step 2. Use response variables sent from MGs, solve the optimization problem (5.40) for DSO, and calculate target variables for MGs.

Step 3. For all MGs, use target variables sent from DSO, solve the optimization problem (5.41) for MG, and calculate response variables for DSO.

Step 4. Check convergence criteria (5.42). If satisfied, the optimal solution is obtained and iteration is stopped; otherwise, go to Step 4.

$$\max(||\mathbf{t}^{k+1} - \mathbf{t}^k||, ||\mathbf{r}^{k+1} - \mathbf{r}^k||) < \sigma \tag{5.42}$$

where σ is consistency deviation termination tolerance.

Step 5. Set $k = k + 1$ and update Lagrange multiplier and penalty factor defined in (5.43) and (5.44) and go to Step 2.

$$\lambda^{k+1} = \lambda^k + 2\mathbf{w}^k \circ \mathbf{w}^k \circ (\mathbf{t}^k - \mathbf{r}^k) \tag{5.43}$$

$$\mathbf{w}^{k+1} = \beta \mathbf{w}^k, \beta \geq 1 \tag{5.44}$$

where (5.43) and (5.44) are linear updating schemes for selecting new Lagrange multiplier and penalty factor for the next iteration. New estimates λ^{k+1} are computed from the old estimates λ^k, weights $\mathbf{w}^k$, and inconsistencies $\mathbf{t}^k - \mathbf{r}^k$. The combination of updating schemes (5.43) and (5.44) is known as the method of multipliers where $\beta \geq 1$ guarantees non-decreasing sequence of penalty factors and convergence to the optimal solution under convexity assumptions

Although the above approach shows stable convergence [76], it prevents optimization problems (5.28) and (5.29) to be solved independently due to non-separable terms in the augmented Lagrangian. When DSO runs its local optimization problem, optimization problems in the MG level are idle and vice versa. As a result, optimization problems in DSO and MGs must be solved sequentially, which is computationally intensive. In the next section, an effective method is proposed to fully separate optimization problems for DSO and MGs. As shown in Section 5.6, the proposed approach significantly improves computational efficiency.

5.4.2 Parallel Computation Formulation

In order to achieve separable consistency constraints and reformulate separated optimization problems for DSO and MGs, the diagonal quadratic approximation (DQA) method [85] is applied to linearize the quadratic terms at each iteration and enable separability and parallel processing of optimization problems for DSO and MGs.

The DQA method addresses non-separable issues via linearization of the cross-product terms $\mathbf{t}_n \circ \mathbf{r}_n$ included in the quadratic penalty term $\|\mathbf{t}_n - \mathbf{r}_n\|_2^2$ in (5.40) and (5.41) around $\mathbf{t}_n^k$ and $\mathbf{r}_n^k$, solutions obtained from the previous iteration, as

$$\|\mathbf{t}_n - \mathbf{r}_n\|_2^2 \cong \|\mathbf{t}_n^k - \mathbf{r}_n\|_2^2 + \|\mathbf{t}_n - \mathbf{r}_n^k\|_2^2 + Constant\,. \tag{5.45}$$

Full mathematical linearization is presented in the Appendix B.1. The constant term in (5.45) can be removed. Moreover, $\mathbf{t}_n^k$ and $\mathbf{r}_n^k$ are constant with respect to the problem of current iteration. Hence, the term $\|\mathbf{t}_n^k - \mathbf{r}_n\|_2^2$ is constant with respect to the optimization problem in DSO, and the term $\|\mathbf{t}_n - \mathbf{r}_n^k\|_2^2$ is constant with respect to the optimization problem in MG. By substituting (5.45) into (5.40) and (5.41) and removing the constant terms with respect to the problem of the current iteration, (5.40) and (5.41) can be rewritten in decomposable form as

$$\min f_D(\tilde{\mathbf{x}}_D) + \sum_{n=1}^{N} \lambda_n \mathbf{t}_n + \|\mathbf{w}_n \circ (\mathbf{t}_n - \mathbf{r}_n^k)\|_2^2 \tag{5.46}$$

$$\min f_{MG,n}\left(\tilde{\mathbf{x}}_{MG,n}\right) + \lambda_n - \mathbf{r}_n + \|\mathbf{w}_n \circ (\mathbf{t}_n^k - \mathbf{r}_n)\|_2^2\,. \tag{5.47}$$

5.4.3 Parallel Computation Algorithm

The proposed DQA-based distributed energy management algorithm consists of the following steps for parallel computation:

Step 1. Set k =0. Initialize λ, **w,** $\mathbf{t}_n^k$ and $\mathbf{r}_n^k$, $n = 1, \ldots, N$.

Step 2. Use $\mathbf{t}_n^k$ and $\mathbf{r}_n^k$ as shared known variables, solve (5.46) and (5.47) for all MGs and DSO in parallel, calculate $\mathbf{t}_n^{k+1}$ and $\mathbf{r}_n^{k+1}$, and obtain

$$\tilde{\mathbf{x}}^{\boldsymbol{k+1}} = \tilde{\mathbf{x}}^k + \tau(\tilde{\mathbf{x}}^{k+1} - \tilde{\mathbf{x}}^k) \tag{5.48}$$

where τ is the step size.

Step 3. Check consistency termination criteria (5.49). If,

$$\max(||\mathbf{t}^{k+1} - \mathbf{t}^k||, ||\mathbf{r}^{k+1} - \mathbf{r}^k||) < \sigma \tag{5.49}$$

stop; otherwise, go to Step 4.

Step 4. Set $k = k + 1$ and update the Lagrange multiplier and penalty factor defined in (5.50) and (5.51). Go to Step 2.

$$\lambda^{k+1} = \lambda^k + \mathbf{w}^k \circ (\mathbf{t}^k - \mathbf{r}^k) \tag{5.50}$$

$$\mathbf{w}^{k+1} = \beta \mathbf{w}^k, \beta \geq 1 \tag{5.51}$$

where τ is the step size.

5.4.4 On Convergence

The proposed decentralized algorithms rely on the ATC that allows us to address optimization problems with hierarchical structure using augmented Lagrange relaxation. The solution of the proposed sequential computation algorithms can be achieved under the assumption that objective and constraint functions are convex [86] and [87]. However, the presented optimization problems (5.1)-(5.20) and (5.121)-(5.34) for DSO and MG are non-convex. To ensure convergence, the problems are converted to convex form via the sequential convex programming (SCP) method (see [88] and our previous work [45]). In standard convex optimization problems, the inequality constraints are convex and the equality constraints are affine. The proposed approach in [45] provides a "near" optimal solution by obtaining affine approximation of nonlinear equality constraints (active and reactive power balance equations) via Taylor series expansion and transforms inequality constraints (such as voltage and DG power constraints) to convex form (see Appendix B.2). We demonstrate the quality of our suboptimal solution by comparing it with the global optimum obtained via branch and bound method [45]. At the cost of very small compromise in optimality, we achieve significantly lower computational complexity and run time.

Optimization problems as shown in (5.40) and (5.41) are not separable due to the quadratic penalty terms. As a result, an iterative process is carried out by sequentially solving (5.40) and (5.41) for finding optimal solution with respect to fixed λ and $\mathbf{w}$. In order to achieve convergence, the Lagrange multipliers must be updated properly. The augmented Lagrangian function allows use of the method of multipliers to update λ and $\mathbf{w}$ given in (5.43) and (5.44). Convergence properties of the method of multipliers applied to the sequential computation algorithm can be found in [86] and [87].

The parallel computation algorithm also provides an optimal solution if the objective functions and constraint functions are convex and the step size τ is sufficiently small [85]. Moreover, σ should be significantly smaller than step size τ in order to prevent premature convergence. Convergence is proven

for the above algorithm with $\sigma = 0$, as stated in [89]. For practical purposes, however, we allow σ to be very small but non-zero.

The step size τ plays an important role in the DQA method. If linearization is at a point that is a poor approximation to the augmented Lagrangian function, convergence is not guaranteed. A small step size can ensure accuracy of the approximation. However, if the step size is too small, convergence will be significantly slowed down. As a result, some trial and error process is required for finding a good value of the step size for practical applications. For the considered case study, we have found empirically that convergence is efficiently attained with the choice of τ close to 1 and σ significantly smaller than τ. However, note that these parameter choices should be tuned up for each system under consideration. The effect of varying termination tolerance on runtime and solution accuracy is presented in Appendix B.3. In the next subsection, we provide a stochastic framework to model the uncertainties based on PEM.

5.5 Stochastic Model Description

The uncertainties in load and wind generation are considered in this research. It is assumed that loads meet normal distribution and wind speed meets Weibull distribution. The output of WG can be obtained through the piecewise-linear relationship between wind speed and wind turbine output [90]. The presented PEM scheme [84] is applied to estimate the operation cost of DSO and MGs with the above two uncertainties. Unlike the MCS method, the PEM is generally simpler and computationally more efficient to deal with complex models. While finding the reasonable number of scenarios in scenario reduction techniques is often challenging and problem-dependent, PEM systematically selects the required number of scenarios.

5.5.1 Background on PEM

Approaches to deal with problems under uncertainty in power system analysis can be classified into three categories [91]: Monte Carlo simulation (MCS), analytical methods, and approximate methods.

MCS [92] has been widely used to model uncertainty and solves a deterministic problem several times using the randomly generated values for uncertain input variables. It is known as the most accurate but computationally the most expensive method. Analytical methods require less computation time at the expense of losing accuracy due to some mathematical assumptions to simplify the problem [93]. Approximate methods provide a trade-off with an approximate description of the statistical properties of output random variables. PEM [94], [95] fits into the family of approximate methods, and overcomes the difficulties associated with the lack of perfect knowledge of the probability functions of stochastic variables, since these functions are approximated using only their first few statistical moments (i.e., mean, variance, skewness, and kurtosis). Therefore, lesser information is needed. Amongst different PEM schemes, we have used *2m+1* PEM scheme which is proved to provide the best solution in terms of accuracy and computational efforts. The accuracy of PEM in handling uncertainties has been successfully examined on complex problems such as feeder reconfiguration [28], optimal storage planning in active distribution systems [96], and optimal operation management of a MG [97], [98].

5.5.2 Original PEM

Mathematically, the deterministic OPF can be expressed as:

$$\mathcal{O} = F(\mathcal{Z}) \tag{5.52}$$

where $\mathcal{Z}$ is the set of input variables representing the network configuration, load and distributed power generation; *F*(.) is the OPF function; $\mathcal{O}$ is the set of output variables (active and reactive power of DGs, bus voltage or line flows). PEM aims at calculating moments of output variables of interest ($\mathcal{O}_h$) through solution of only a few deterministic OPF runs. Considering *m* input random variables in the system representing the load and WG output, (5.52) can be rewritten as:

$$\mathcal{O}_h = F_h(z_1, z_2, \dots, z_m) \tag{5.53}$$

Let $z_l \in \mathcal{Z}$ be a random variable with probability density function (PDF) f_{z_l} and μ_{z_l}, σ_{z_l}, $\alpha_{z_l,3}$, and $\alpha_{z_l,4}$ denote the mean, variance, third and fourth central moments of z_l. For each z_l, three locations $z_{l,r}, r = 1,2,3$, and the corresponding weighting factors $\omega_{l,r}$ are generated as follows

$$z_{l,r} = \mu_{z_l} + \xi_{l,r}\sigma_{z_l} \quad ,r = 1,2,3 \quad (5.54)$$

$$\xi_{l,r} = \alpha_{z_l,3}/2 + (-1)^{3-r}(\alpha_{z_l,4} - 3\alpha_{z_l,3}^2/4)^{1/2} \quad ,r = 1,2 \quad (5.55)$$

$$\omega_{l,r} = (-1)^{3-r}/\left[\xi_{l,r}(\xi_{l,1} - \xi_{l,2})\right] \quad ,r = 1,2 \quad (5.56)$$

$$\xi_{l,r} = 0, \;\; \omega_{l,r} = 1/m - 1/(\alpha_{z_l,4} - \alpha_{z_l,3}^2) \quad ,r = 3 \quad (5.57)$$

where $\xi_{l,r}$ denotes the standard location. For each z_l, an uncertain scenario is generated with location $\xi_{l,r}$, assuming that other variables are set at their mean value. Theoretically, there are $3m$ scenarios. However, (57) indicates that m out of $3m$ scenarios are repeated with zero standard location for the third location ($\xi_{l,r} = 0,, r = 3$) and (54) implies $z_{l,r} = \mu_{z_l}$ for these scenarios. Hence, $2m$+1 scenarios with weighting factor $\omega_s = \omega_{l,r}$ are generated to approximate the results under uncertainty. Once solutions of the $2m$+1 OPFs are obtained using (53), the γth raw moment of $\mathcal{O}_h$ can be calculated as

$$E\left(\mathcal{O}_h^{\gamma}\right) \cong \sum_{l=1}^{m}\sum_{r=1}^{2} \omega_{l,r}\mathcal{O}_h(l,r)^{\gamma} + F_h\left(\mu_{z_1}, \dots, z_{l,r}, \dots, \mu_{z_m}\right)^{\gamma}\sum_{l=1}^{m}\omega_{l,3}. \quad (5.58)$$

The PDF of the output variables can be approximated by Gram-Charlier series approach [99].

5.5.3 Improved PEM

Apart from the turbine technology, the power output of a WG is highly dependent on many factors related to wind itself, such as the wind regime at the site location, the wind penetration level, the correlation between multiple wind farms in the system, etc [100]. Renewable DERs such as WGs, are essentially intermittent and spatially correlated in the geographical area that encompasses DSO and MGs as these entities are influenced often by the same wind levels. Therefore, such a correlation between closely located WGs may have a very significant impact on power flow and subsequently the grid operation [101], [93], [102], [103], and [104]. In fact, neglecting the possible correlation between WGs

would result in conservative performance results in comparison to traditional trading strategies for DSO and MG. It is crucial that electricity system operators understand the patterns of wind to maximize their economic benefits, and the correlations between WGs is one area where a better understanding could lead to reduced system costs. Wind power correlation impact has been considered in many power systems studies including MG modeling [93], electricity markets [102], transient stability [103], and voltage control [104]. Therefore, an improved PEM capable of accounting for statistical correlations among resources is introduced. In particular, the orthogonal transformation based on Cholesky decomposition [101] is used to generate uncorrelated set $\mathcal{U}$ from the correlated set $\mathcal{Z}$ with the corresponding symmetric correlation matrix $\rho_{\mathcal{Z}}$. The following steps describe the improved PEM method to generate the uncorrelated set:

Step 1. Given the correlation matrix $\rho_{\mathcal{Z}}$, obtain the orthogonal matrix $\mathcal{B}$ by Cholesky decomposition using $\rho_{\mathcal{Z}} = LL^T$ and $\mathcal{B} = L^{-1}$.

Step 2. Transform the correlated set $\mathcal{Z}$ into a new set of independent variables $\mathcal{U}$ whose first four central moments satisfy (5.59) and (5.60) (under the assumption that the joint moments of an order higher than two are zero)

$$\mu_{\mathcal{U}} = \mathcal{B}\mu_{\mathcal{Z}}; \qquad \sigma_{\mathcal{U}}^2 = I_m; \tag{5.59}$$

$$\alpha_{u_l,3} = \sum_{l=1}^{m} (b_{l,d})^3 \alpha_{z_l,3} \sigma_{z_l}^3; \quad \alpha_{u_l,4} = \sum_{l=1}^{m} (b_{l,d})^4 \alpha_{z_l,4} \sigma_{z_l}^4 \tag{5.60}$$

where I_m is the m-dimensional identity matrix and $b_{l,d}$ is the lth row and dth column element of $\mathcal{B}$.

Step 3. Use (5.54)–(5.57) to calculate pairs $(u_{l,r}, \omega_{l,r})$ and construct $2m + 1$ independent points in the form $(\mu_{u_1}, \dots, u_{l,r}, \dots, \mu_{u_m})$.

Step 4. Transform the points generated in Step 3 to the original space by $\mathcal{Z} = \mathcal{B}^{-1}\mathcal{U}$.

Step 5. Calculate the deterministic solution for each one of the points generated from Step 4. The hth component of the solution vector yields

$$\mathcal{O}_h(l,r) = F_h\left(\mu_{z_1}, \dots, z_{l,r}, \dots, \mu_{z_m}\right) \qquad l = 1,..m; r = 1,2\,. \quad (5.61)$$

Step 6. Calculate the γth raw moment of $\mathcal{O}_h$ using (5.58).

Step 7. Approximate the PDF of the output variables of interest using Gram-Charlier series approach [105].

In the next subsection, promising results of the proposed method are shown via numerical examples.

5.6 Simulation Results

In this section, stochastic energy management of networked MGs in a distribution system with correlated WGs is presented. The studies have been implemented on an Intel(R) Core(TM) i7, 3.4 GHz personal computer with 8 GB of RAM. The presented study deals with single-period energy management (one-shot simulations), though, it is extendible to multi-period, multi-MG energy management problems.

5.6.1 Network and Parameters Description

The proposed method is tested on the modified IEEE 69-bus test feeder including one DSO and three MGs as shown in Figure 5.3. The network data can be found in [106]. DGs are connected to buses #10, #27, #38, #53, #54, #68 with corresponding capacities of 500 kW, 300 kW, 500 kW, 600 kW, 600 kW, and 50 kW, respectively. DGs are considered to have a fixed power factor of 0.9 lagging. WGs' output powers follow Weibull distribution with mean speed of 7 meters and the shape parameter of 2 [84]. WGs are connected to buses #21, #30, #50 with corresponding mean power of 300 kW, 500 kW, and 600 kW, respectively. Loads are assumed to be normally distributed with means equal to the values provided in Table 1 of [106] and a constant standard deviation (STD) of 5%. Further, loads located within the same entity on buses (16, 21), (38, 39), and (50, 53, 54) are correlated with a correlation coefficient of

0.9. This correlation drops up to 0.5 for loads in different entities. The correlation matrix between the three WGs is considered as follows [107]:

$$\rho_Z = \begin{bmatrix} 1 & 0.8 & 0.7 \\ 0.8 & 1 & 0.6 \\ 0.7 & 0.6 & 1 \end{bmatrix}$$

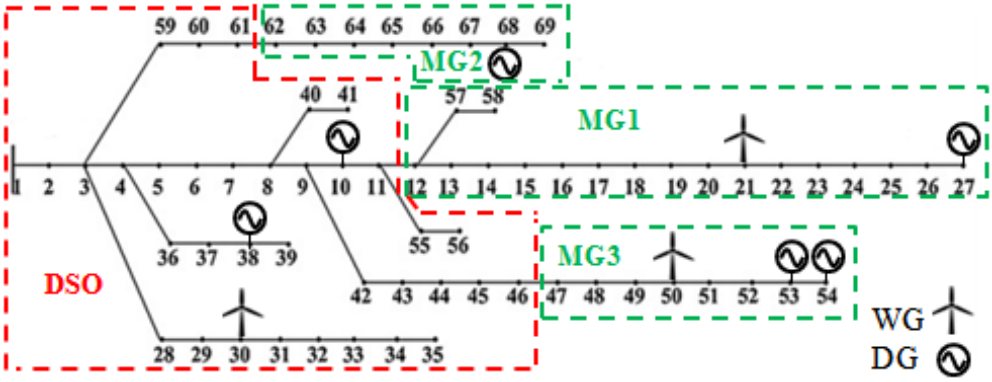

Figure 5.3 Modified IEEE 69 bus test feeder.

Table 5.1 shows the buying and selling electricity prices for DSO and MG [108]. For the sake of simplicity and without loss of generality, we assume that WGs and loads are uncorrelated. Initial values for λ and w were set to 0 and 1, and initial values for σ and τ were set to 10^{-4} and 10^{-3}, respectively. Voltage magnitude and angle of the reference bus are set to 1 and 0, respectively.

Table 5.1 Electricity price ($/kW)

$C_{S,D}$	$C_{D,S}$	$C_{D,n}$	$C_{M,n}$	$C^{D}_{DG,i}$	$C^{D}_{L,i}$	$C^{M}_{DG,i}$	$C^{M}_{L,i}$
0.3	0.32	0.25	0.28	0.1	0.3	0.1	0.3

5.6.2 Deterministic Solution

Table 5.2 shows the optimal generation scheduling of DGs in all entities for sequential and parallel computation approaches. Also, the absolute percentage error (APE) between the two approaches is tabulated. It can be inferred that results from sequential and parallel DQA-based algorithms are comparable with maximum APE of value 1.6%.

Table 5.2 DGS' ACTIVE POWER (KW) FOR SEQUENTIAL AND PARALLELIZED COORDINATION APPROACHES

Entity	Generation	Sequential	Parallelized	APE (%)
DSO	DG1	485.2	488.8	0.74196
	DG2	440.12	436.32	0.863401
MG1	DG3	271.2	273.7	0.92183
MG2	DG4	48	47.2	1.666667
MG3	DG5	548.7	546.5	0.400948
	DG6	577.5	578.6	0.19048

Table 5.3 shows the power exchange between entities and profit per entity using sequential and parallel computation approaches.

Table 5.3 Power exchange and profit per entity from sequential and parallelized coordination approaches

Method	From	To	Power Exchange (kW)	Profit of 'To' Entity ($)
Sequential	TSO	DSO	105	311.35
	DSO	MG1	-68.4	142.872
	DSO	MG2	85.6	13.88
	DSO	MG3	-64.2	403.956
Parallelized	TSO	DSO	104.5	312.791
	DSO	MG1	-71	143.35
	DSO	MG2	86.5	13.735
	DSO	MG3	-63.1	403.758

Figure 5.4(a) and Figure 5.4(b) show the error evolution via sequential and parallelized computation approach in the active power flowing through tie-lines connecting the DSO to MGs. Sequential computation approach converges to a solution after 5 iterations whereas the parallel computation approach converges after 8 iterations.

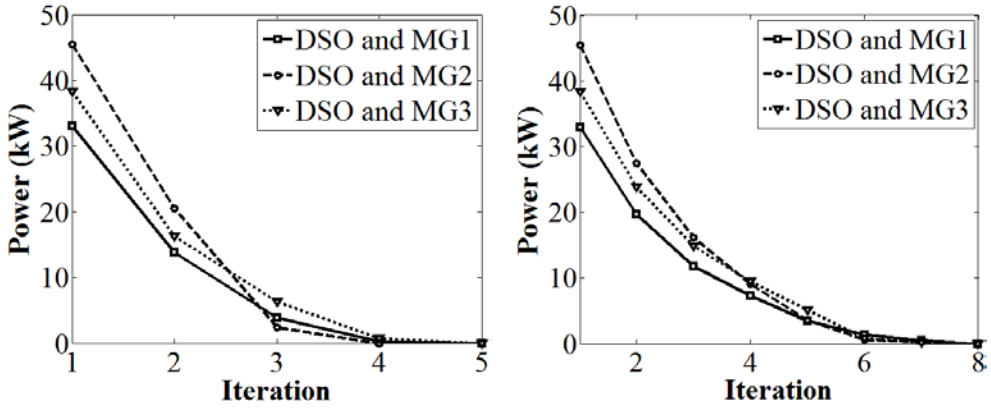

Figure 5.4 Error evolution in tie-line connecting DSO to TSO and MGs. (a) sequential computation approach, and (b) parallel computation approach.

Execution times are 15.12 and 2.39 seconds for sequential and parallel computation approaches, respectively, demonstrating significant reduction in execution time with slight accuracy loss for the parallel approach compared to the sequential approach. Hence, in what follows, we only use the parallel computation method and present the results based on this approach.

5.6.3 Stochastic Solution

In his section, stochastic energy management with and without wind generation correlation is presented. The mean and STD of DGs' active power, power exchange between entities and profit per entity are outlined in Table 5.4 and Table 5.5.

Table 5.4 Mean and STD of DGs' active power (kW) with Uncorrelated and Correlated Wind Generators.

Entity	Gen. Source	Uncorrelated		Correlated	
		Mean	STD	Mean	STD
DSO	DG1	490.9	24.44	491.4	26.98
	DG2	439.11	22.16	439.71	24.03
MG1	DG3	275.6	12.68	278.9	15.31
MG2	DG4	46.5	2.36	44.8	2.89
MG3	DG5	548.6	33.45	550.4	37.64
	DG6	580.4	34.86	582.2	39.03

For the uncorrelated scenario, generation of DG in MG2 has the lowest STD values since there is no uncertain load or generation and MG2 only gets influenced from DSO. This is confirmed from the lowest STD observed in power exchange between DSO and MG2 as presented in Table 5.5. Moreover, the expected profit of MG2 decreased a little bit compared to the deterministic solution. The STD values of generation units in MG3 are the largest due to the fact that MG3 has the largest uncertain load and generation among MGs and the variations of uncertain load and generation directly affects the DGs' generation in MG3. As a result, the largest STD values are achieved for power exchange between DSO and MG3. Further, the mean of generation units increased and the profit of MG3 decreased compared to the deterministic solution.

Table 5.5 Power exchange, profit per entity and total system profit with Uncorrelated and Correlated Wind Generators.

Method	From	To	Power Exchange (kW)		Profit of 'To' Entity ($)	
			Mean	STD	Mean	STD
Uncorrelated	TSO	DSO	105.1	7.08	311.32	18.55
	DSO	MG1	-68.8	5.25	142.54	11.72
	DSO	MG2	87.2	4.94	13.63	1.06
	DSO	MG3	-58.3	7.70	402.02	29.12
Correlated	TSO	DSO	106.3	8.62	308.93	20.02
	DSO	MG1	-72.5	6.36	143.05	12.68
	DSO	MG2	85.4	5.12	14.25	1.12
	DSO	MG3	-65.1	8.82	403.26	33.21

Further, the mean values of generation units in MG1 and DSO have also increased due to uncertainty. It is mainly because DSO and MGs are trying to reduce their operation cost with their cheaper DG units rather buying power from other entities.

Upon comparing the results with and without correlation shown in Table 5.4 and Table 5.5, it is clear that the STD values of output variables increased due to the correlation between WGs. In particular,

the STD of power exchange between DSO and MG2 and MG3 increased the most. Moreover the mean values of generation units in DSO and MG2 and MG3 increased due to the fact that correlated WGs are located in these entities. Overall, the mean profit value in DSO decreased while the mean profit values of MG1, MG2 and MG3 increased due to correlation, though the increment is small. This is mainly because MGs have much larger DG capacities installed to deal with load and generation uncertainties (totally 1550 kW) compared to that of DSO (1000 kW) while load is much higher in the DSO (1966.1 kW) compared to load in individual MGs (502.8 kW, 410 kW, and 923.2 kW for MG1, MG2, and MG3, respectively).

In Table 5.6 performance of the proposed approach is compared to the MCS with 6000 samples in terms of solution accuracy and computation time. In particular, the absolute percentage error in mean (APE_μ) and STD (APE_σ) for the profit per entity is presented. The maximum APE_μ and APE_σ observed are 1.39% and 6%, respectively, which highlights accuracy of the results. Errors associated with the STD values are greater than those corresponding to the means. This is tied to the characteristic of the PEM methods, where the accuracy of estimates gets worse as the order of statistical moments increase [101].

The CPU times for calculating the mean and STD values via PEM and MCS methods are 48.67 and 1.684e3 seconds, respectively. As expected, the proposed method is computationally much more efficient than the MCS.

Table 5.6 Accuracy and Computation Time Comparison.

Entity	APE_μ(%)	APE_σ(%)	CPU Time (s)	
			PEM	MCS
DSO	0.6183	3.2467	48.67	1.684e3
MG1	0.5592	2.3659		
MG2	0.2807	0.4464		
MG3	1.3918	6.0223		

5.6.4 Impact of Correlation Level between WGs

In this section, a sensitivity analysis is conducted to investigate influences of the correlation level between WGs on the profit of DSO and MGs. To this end, the correlation coefficient (ρ) between WGs increases from 0.1 to 1 with incremental steps of 0.1 and impacts on the mean and STD of profit for TSO, and MGs are shown in Figure 5.5(a) to Figure 5.5(d). For a correlation coefficient between 0 to 0.8, the mean profit value of DSO followed a downward trend while the mean profit value of MGs increased. For higher correlation coefficient, the mean profit value of DSO and MGs exhibited the reverse trend. However, mean values are marginally impacted by WG correlation.

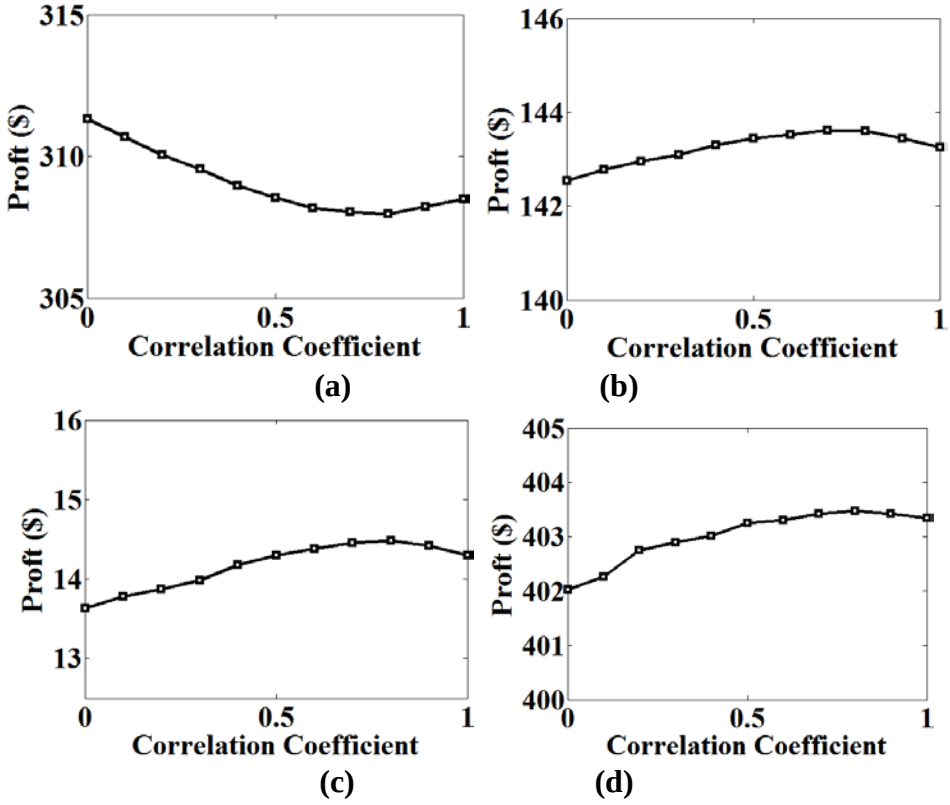

Figure 5.5 Correlation effect on the mean profit value of (a) MG1, (b) MG2, (c) MG3, and (d) MG4

The same study is also conducted to see impact of correlation between WGs on STD of profit values. Figure 5.6(a) to Figure 5.6(d) show the PDF of profit for each entity with consideration of 0.1, 0.5 and 0.9 correlation coefficient between WGs. Observe that as the correlation coefficient between WGs

increases the PDF of profit for MG2 remains very close to the normal distribution with a relatively small change in STD since MG2 has no uncertain load and generation sources. The PDF of profit for MG1 and MG3 shows a different phenomenon with increase in ρ, where the PDF has a "tail" on the right-hand side of the profit's PDF. This right-skewed distribution increased the STD values as confirmed in Table V for $\rho = 0.9$. It can be inferred that with the increase in correlation level among WGs, higher STDs of profit for MG1 and MG3 are achieved, which are the MGs with high level of uncertain load and generation. In general, increase in correlation level among WGs translates into higher STD of profit for DSO and MGs. In particular, the STD of profit for MG1 is influenced the least whereas the STDs of profit for DSO, MG2 and MG3 are significantly affected by WGs correlation.

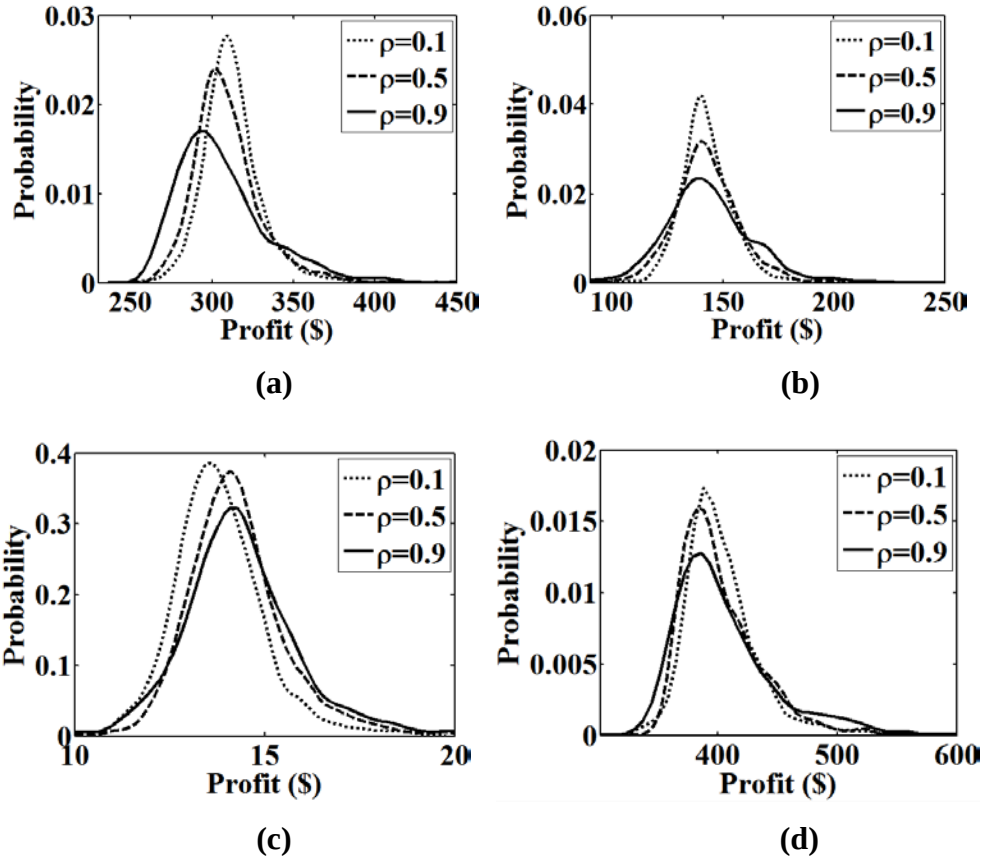

Figure 5.6 Correlation effect on the STD profit value of (a) MG1, (b) MG2, (c) MG3, and (d) MG4.

5.7 Summary

This chapter presents stochastic energy management between DSO and MGs with consideration of correlated WGs. Initially, a bi-level distributed sequential computation algorithm is proposed to characterize interactions between DSO and MGs in a deterministic fashion where each entity pursues its own objective. In addition, a linear approximation is introduced to resolve non-separability issues in the sequential algorithm, originated from the coupling constraints between DSO and MGs. Further, a parallelized computation algorithm is proposed to enable parallel processing of the optimization problems in DSO and MGs. Moreover, a stochastic framework based on 2m+1 PEM is proposed to model the uncertainty in load and wind generation. Finally, an improved PEM is introduced to model the statistical correlations among WGs. A test case of modified IEEE 69 bus system including one DSO and three MGs is studied. Simulation results show that the proposed algorithm presents high computational efficiency and properly handles correlations. The results indicate that the correlation between loads and between WGs have significant impact on the energy management of DSO and MGs. The sensitivity analysis reveals small decrease in the expected profit of entities whereas the STD values of profits increased notably as the correlation between WGs increase.

6 Conclusion and Future Work Direction

This chapter concludes the dissertation and summarizes the future research directions.

6.1 Conclusions

This research develops unique models and methodologies to overcome issues related to high penetration of DERs and development of MGs and to make distribution grid operation, optimization and control more robust against renewable intermittency, scalability, and operation complexity. Compared to the existing literature, the main contributions of this dissertation are as follows:

- Since numerous smart devices, such as smart meters, smart inverters, rooftop solar PVs, battery storage and electric vehicles will be deployed into homes located at the secondary distribution system, in this dissertation, a 559 node three-phase unbalanced test system including primary, lateral, and secondary feeders is developed to serve as a benchmark for studying the issues related to DER integration in large-scale networks.
- In order to address the scalability concern associated with high penetration of DER in large-scale distribution grids, this dissertation proposes a novel distributed optimization based on hierarchical structure of distribution grids. To this end, analytical target cascading (ATC) method, which is tailored to solve hierarchically structured complex problems, is used to decompose the entire distribution network over distinct primary, lateral, and secondary feeder sub-network levels. Since sub-networks are coupled together, a distributed sequential coordination scheme is developed to minimize power losses while considering the operational constraints. Further, a virtual feeder is introduced which separates the coupled sub-networks in decomposed layers, enables parallel processing of optimization problems, reduces computational complexity, and provides faster solution. The method is tested and validated on the developed large-scale network.

- An operational scheme for PV inverter reactive power control to accommodate higher levels and leverage efficient use of rooftop PV penetration in distribution systems is presented. The scheme proposes three states of operation with specific operational goals for the PV inverter based on weather conditions and voltage at the interconnection point, and adapts the reactive power control strategy accordingly. In normal state with slowly changing solar irradiance, the control modulates reactive power to reduce power losses. In fluctuating state with rapidly varying solar irradiance due to intermittent passing clouds, the control dynamically changes the reactive power in order to mitigate voltage fluctuations. In contingency state in which the PV terminal voltage violates the nominal operating range, the control adjusts the PV inverter as reactive power sink or source in order to push the voltage back within the range. This research also proposes a coordination strategy in order to switch control between the states and manage interaction between the fast PV inverter controllers and the slow on-load tap-changer (OLTC) for voltage regulation. The developed large-scale distribution network is used in order to investigate performance of the proposed algorithm.
- A novel stochastic framework to investigate the impact of correlated wind generators (WGs) on energy management of DSO and MGs is also presented. In order to decouple the problem formulation in DSO and MGs, a linear approximation is proposed which enables parallel processing of optimization problems. Further, a stochastic framework based on improved point estimate method (PEM) is proposed to model the uncertainty in load and wind generation and account for the statistical correlations among wind generators. The proposed method is applied to a modified IEEE 69 bus test feeder and the results are validated in terms of efficiency and accuracy.

Based on the research accomplished in this dissertation, some future research directions are highlighted in the next section.

6.2 Future Work Directions

The potential research directions are summarized as follows:

- The proposed distributed OPF for loss minimization in this research considers only reactive power capability of PV inverters and performs single-period (one-shot) simulations. Applicability of the proposed approach in the context of high PV penetration and scalability concerns can be investigated for multi-period formulation with consideration of LTC, capacitor, and inverter operation.
- The dynamic operational scheme is presented for local reactive power provisioning control of single-phases inverters. The study can be further investigated to coordinate between inverters for mutual inferencing and implementing the approach to three-phase inverters.
- Grid-connected mode is assumed in this research. For future research, adopting the scheme for islanded mode can be examined.
- The proposed dynamic inverter operational scheme can be further investigated to include night-time operation.
- Other stochastic programing techniques such as robust optimization can be employed to model the uncertain variables in the stochastic energy management model of DSO and MGs with correlated wind generators.
- This research assumed Weibull distribution for wind speed modeling. The study can further investigate the impact of correlation on energy management of DSO and MGs by considering correlations of wind speeds following different statistical distributions.

- The proposed approach can possibly be extended to include multiple DSOs that interact with a TSO in a multi-period set-up. Future work will carefully study the impact of wind power spillage on DSO-MG energy management.

Bibliography

[1] Edison Tech Center, "'The History of Electrification: The Birth of our Power Grid," *[Online].Available: http://edisontechcenter.org/HistElectPowTrans.html,* 2013.

[2] EPRI Technical Report, *[Online].Available:https://www.smartgrid.gov/files/Estimating_Costs_Benefits_Smart_Grid_Preliminary_Estimate_In_201103.pdf;*, 2011.

[3] International Energy Agency, "'Technology Roadmap Solar Photovoltaic Energy," *[Online].Available:https://www.iea.org/publications/freepublications/publication/TechnologyRoadmapSolarPhotovoltaicEnergy_2014edition.pdf*, 2014.

[4] International Energy Agency, "'Technology Roadmap: Wind energy," *[Online].Available:https://www.iea.org/publications/freepublications/publication/Wind_2013_Roadmap.pdf;*, 2013.

[5] Profiling and Mapping of Intelligent Grid R&D Programs, *EPRI, Palo Alto, CA and EDF R&D, Clamart, France: 2006. 1014600.*

[6] U.S. Department of Energy, Office of Electricity Delivery and Energy Reliability, "'Smart grid research and development, multi-year program plan (MYPP)," *[Online].Available: http://www.oe.energy.gov/DocumentsandMedia/ SG_MYPP.pdf.*, 2010.

[7] Office of Energy Efficiency and Renewable Energy, "'Distributed PV Monitoring," *[Online]. Available:http://www1.eere.energy.gov/solar/pdfs/hpsp_grid_workshop_2012_nicole_epri.pdf;*, 2012.

[8] R.H. Lasseter, "'MicroGrids," *IEEE Power Eng. Soc. Winter Meet.*, vol. 1, 2002, pp. 305-308.

[9] R. Yan and T.K. Saha, "'Voltage Variation Sensitivity Analysis for Unbalanced Distribution Networks Due to Photovoltaic Power Fluctuations," *IEEE Trans. Power Syst.*, vol. 27, no. 2, 2012, pp. 1078-1089.

[10] M. Milligan and B. Kirby, "'Utilizing load response for wind and solar integration and power system reliability," *Wind Power Conference, Dallas, Texas*, 2010.

[11] A.A.S. Algarni and K. Bhattacharya, "'Disco Operation Considering DG Units and Their Goodness Factors," *IEEE Trans. Power Syst.*, vol. 24, no. 4, 2009, pp. 1831-1840.

[12] J. Seuss, M.J. Reno, R.J. Broderick and S. Grijalva, "'Maximum PV size limited by the impact to distribution protection," *Photovoltaic Specialist Conference (PVSC), 2015 IEEE 42nd*, pp. 1-6.

[13] M.A. Cohen and D.S. Callaway, "'Physical Effects of Distributed PV Generation on California's Distribution System," *arxiv.org/pdf/1506.06643*, 2015.

[14] U.S. Energy Information Administration, "'Modeling distributed generation in the buildings sectors," *[Online].Available:https://www.eia.gov/forecasts/aeo/nems/2013/buildings/pdf/distribgen.pdf;*, 2013.
[15] U.S. Energy Information Administration, "'Electricity Distribution Losses (Billion Kilowatthours)," *[Online].Available:http://www.eia.gov/cfapps/ipdbproject/IEDIndex3.cfm?tid=2&pid=2&aid=9;*.
[16] U.S. Energy Information Administration, "'How much electricity is lost in transmission and distribution in the United States?" *[Online].Available:http://www.eia.gov/tools/faqs/faq.cfm?id=105&t=3;*.
[17] U.S. Department of Energy, Office of Electricity Delivery and Energy Reliability, "'City of Glendale Smart Grid Initiative," *https://www.smartgrid.gov/files/City_Glendale_Project_Description_20131209_0.pdf*, 2009.
[18] U.S. Department of Energy, Office of Electricity Delivery and Energy Reliability, "'PECO Smart Future Greater Philadelphia," *[Online]*. *Available:https://www.smartgrid.gov/sites/default/files/pdfs/project_desc/PECO_Project_Description-Final.pdf;*.
[19] U.S. Department of Energy, Office of Electricity Delivery and Energy Reliability, "'Westar Energy, Inc. SmartStar Lawrence Project," *[Online]*. *Available:https://www.smartgrid.gov/sites/default/files/pdfs/project_desc/Westar%20Energy%20Final%20Project%20Description%20-%20reformatted_0.pdf;*, 2009.
[20] A.R. Malekpour, A.R. Malekpour, A. Pahwa and S. Das, "'Inverter-based var control in low voltage distribution systems with rooftop solar PV," *2013 North American Power Symposium (NAPS)*, pp. 1-5.
[21] T. Stetz, F. Marten and M. Braun, "'Improved Low Voltage Grid-Integration of Photovoltaic Systems in Germany," *IEEE Transactions on Sustainable Energy*, vol. 4, no. 2, 2013, pp. 534-542.
[22] A.R. Malekpour, "'Reactive power and voltage control in distribution systems with photovoltaic generation," *2012 North American Power Symposium, NAPS 2012*.
[23] J.W. Smith, W. Sunderman, R. Dugan and B. Seal, "'Smart inverter volt/var control functions for high penetration of PV on distribution systems," *2011 IEEE/PES Power Systems Conference and Exposition*, pp. 1-6.
[24] M. Yang and K. Kim, "'Optimal Power Flow Calculation Structure for Energy Management System in Real-Time," *Computational Intelligence, Modelling and Simulation (CIMSim), 2013 Fifth International Conference on*, 2013, pp. 282-287.

[25] A. Borghetti, "'Using mixed integer programming for the volt/var optimization in distribution feeders," *Electr.Power Syst.Res.*, vol. 98, 2013, pp. 39-50.
[26] T. Senjyu, Y. Miyazato, A. Yona, N. Urasaki and T. Funabashi, "'Optimal Distribution Voltage Control and Coordination With Distributed Generation," *IEEE Trans.Power Del.*, vol. 23, no. 2, 2008, pp. 1236-1242.
[27] A. Cagnano, E. De Tuglie, M. Liserre and R.A. Mastromauro, "'Online Optimal Reactive Power Control Strategy of PV Inverters," *IEEE Trans.Ind.Electron.*, vol. 58, no. 10, 2011, pp. 4549-4558.
[28] A.R. Malekpour and T. Niknam, "'A probabilistic multi-objective daily Volt/Var control at distribution networks including renewable energy sources," *Energy*, vol. 36, no. 5, 2011, pp. 3477-3488.
[29] F. Capitanescu, I. Bilibin and E. Romero Ramos, "'A Comprehensive Centralized Approach for Voltage Constraints Management in Active Distribution Grid," *IEEE Trans.Power Syst.*, vol. 29, no. 2, 2014, pp. 933-942.
[30] P.M.S. Carvalho, P.F. Correia and L.A.F. Ferreira, "'Distributed Reactive Power Generation Control for Voltage Rise Mitigation in Distribution Networks," *IEEE Trans.Power Syst.*, vol. 23, no. 2, 2008, pp. 766-772.
[31] T. Sansawatt, L.F. Ochoa and G.P. Harrison, "'Smart Decentralized Control of DG for Voltage and Thermal Constraint Management," *IEEE Trans.Power Syst.*, vol. 27, no. 3, 2012, pp. 1637-1645.
[32] F.A. Viawan and D. Karlsson, "'Combined Local and Remote Voltage and Reactive Power Control in the Presence of Induction Machine Distributed Generation," *IEEE Trans.Power Syst.*, vol. 22, no. 4, 2007, pp. 2003-2012.
[33] M. Brenna, E. De Berardinis, L. Delli Carpini, F. Foiadelli, P. Paulon, P. Petroni, G. Sapienza, G. Scrosati and D. Zaninelli, "'Automatic Distributed Voltage Control Algorithm in Smart Grids Applications," *IEEE Trans. Smart Grid*, vol. 4, no. 2, 2013, pp. 877-885.
[34] P. Šulc, P. Sulc, S. Backhaus and M. Chertkov, "'Optimal Distributed Control of Reactive Power Via the Alternating Direction Method of Multipliers," *IEEE Trans.Energy Convers.*, vol. 29, no. 4, 2013, pp. 968-977.
[35] E. Dall'Anese, E. DallAnese, S.V. Dhople, B.B. Johnson and G.B. Giannakis, "'Decentralized Optimal Dispatch of Photovoltaic Inverters in Residential Distribution Systems," *IEEE Trans.Energy Convers.*, vol. 29, no. 4, 2014, pp. 957-967.
[36] E. Dall'Anese, G.B. Hao Zhu and Giannakis, "'Distributed Optimal Power Flow for Smart Microgrids," *IEEE Transactions on Smart Grid*, vol. 4, no. 3, 2013, pp. 1464-1475.

[37] T. Alquthami and A.P. Meliopoulos, "'Hierarchical optimization and control of a distribution system," *2013 North American Power Symposium (NAPS)*, pp. 1-6.
[38] A.P. Meliopoulos, G.J. Cokkinides, R. Huang and E. Farantatos, "'Integrated Smart Grid Hierarchical Control," *2012 45th Hawaii International Conference on System Sciences*, pp. 1967-1976.
[39] N. Cai and J. Mitra, "'A multi-level control architecture for master-slave organized microgrids with power electronic interfaces," *Electr.Power Syst.Res.*, vol. 109, 2014, pp. 8-19.
[40] W. Yao, J. Zhao, F. Wen, Y. Xue and G. Ledwich, "'A Hierarchical Decomposition Approach for Coordinated Dispatch of Plug-in Electric Vehicles," *IEEE Trans.Power Syst.*, vol. 28, no. 3, 2013, pp. 2768-2778.
[41] F. Lin, M.P. Polis, C. Wang, H. Le Yi Wang and Zhang, "'Hierarchical control and management of virtual microgrids for vehicle electrification," *2012 IEEE Transportation Electrification Conference and Expo (ITEC)*, pp. 1-6.
[42] S. Weckx, C. Gonzalez and J. Driesen, "'Combined Central and Local Active and Reactive Power Control of PV Inverters," *IEEE Transactions on Sustainable Energy*, vol. 5, no. 3, 2014, pp. 776-784.
[43] S. Paudyal, C.A. Canizares and K. Bhattacharya, "'Optimal Operation of Distribution Feeders in Smart Grids," *IEEE Trans.Ind.Electron.*, vol. 58, no. 10, 2011, pp. 4495-4503.
[44] L.R. Araujo, D.R.R. Penido, S. Carneiro and J.L.R. Pereira, "'A Three-Phase Optimal Power-Flow Algorithm to Mitigate Voltage Unbalance," *IEEE Trans.Power Del.*, vol. 28, no. 4, 2013, pp. 2394-2402.
[45] S. Deshmukh, B. Natarajan and A. Pahwa, "'Voltage/VAR Control in Distribution Networks via Reactive Power Injection Through Distributed Generators," *IEEE Transactions on Smart Grid*, vol. 3, no. 3, 2012, pp. 1226-1234.
[46] "IEEE Standard for Interconnecting Distributed Resources with Electric Power Systems", IEEE Std 1547-2003, .
[47] "IEEE 1547 Standard for Interconnecting Distributed Resources with Electric Power Systems" IEEE Std 1547 Amendment 1-2014, .
[48] VDE-AR-N 4105, "'Generators Connected to the LV Distribution Network—Technical Requirements for the Connection to and Parallel Operation with Low-Voltage Distribution Networks,", VDE Std, 2011.
[49] CEI 0-21, "'Reference Technical Rules for Connecting Active and Passive Users to Networks Low-Voltage Electricity Networks of Energy Providers,", CEI Std, 2011;.

[50] E. Demirok, P.C. González, K.H.B. Frederiksen, D. Sera, P. Rodriguez and R. Teodorescu, '"Local Reactive Power Control Methods for Overvoltage Prevention of Distributed Solar Inverters in Low-Voltage Grids," *IEEE Journal of Photovoltaics*, vol. 1, no. 2, 2011, pp. 174-182.

[51] T. Stetz, K. Diwold, M. Kraiczy, D. Geibel, S. Schmidt and M. Braun, '"Techno-Economic Assessment of Voltage Control Strategies in Low Voltage Grids," *IEEE Transactions on Smart Grid*, vol. 5, no. 4, 2014, pp. 2125-2132.

[52] A. Samadi, R. Eriksson, L. Soder, B.G. Rawn and J.C. Boemer, '"Coordinated Active Power-Dependent Voltage Regulation in Distribution Grids With PV Systems," *IEEE Trans.Power Del.*, vol. 29, no. 3, 2014, pp. 1454-1464.

[53] J.W. Smith, W. Sunderman, R. Dugan and B. Seal, '"Smart inverter volt/var control functions for high penetration of PV on distribution systems," *2011 IEEE/PES Power Systems Conference and Exposition*, pp. 1-6.

[54] P.M.S. Carvalho, P.F. Correia and L.A.F. Ferreira, '"Distributed Reactive Power Generation Control for Voltage Rise Mitigation in Distribution Networks," *IEEE Trans.Power Syst.*, vol. 23, no. 2, 2008, pp. 766-772.

[55] Y. Wang, P. Zhang, W. Li, W. Xiao and A. Abdollahi, '"Online Overvoltage Prevention Control of Photovoltaic Generators in Microgrids," *IEEE Transactions on Smart Grid*, vol. 3, no. 4, 2012, pp. 2071-2078.

[56] R. Tonkoski, L.A.C. Lopes and T.H.M. El-Fouly, '"Coordinated Active Power Curtailment of Grid Connected PV Inverters for Overvoltage Prevention," *IEEE Transactions on Sustainable Energy*, vol. 2, no. 2, 2011, pp. 139-147.

[57] R. Yan, B. Marais and T.K. Saha, '"Impacts of residential photovoltaic power fluctuation on on-load tap changer operation and a solution using DSTATCOM," *Electr.Power Syst.Res.*, vol. 111, 2014, pp. 185-193.

[58] M.J.E. Alam, K.M. Muttaqi and D. Sutanto, '"A Multi-Mode Control Strategy for VAr Support by Solar PV Inverters in Distribution Networks," *IEEE Trans.Power Syst.*, vol. 30, no. 3, 2015, pp. 1316-1326.

[59] [Online].Available:http://www.pv-magazine.com/archive/articles/beitrag/generating-dollars-where-theres-no-sun-_100003490/329/#axzz3yHWclb95, .

[60] M. Yue, M. Yue and X. Wang, '"Dynamic modeling of grid integrated solar and battery energy system for cloud transient impact study," *2013 IEEE Energytech*, pp. 1-6.

[61] E. Abdelkarim, M.M. Aly, M. Abdel-Akher, Z. Ziadi and T. Senjyu, "'Supersession of large penetration photovoltaic power transients using storage batteries," *2013 IEEE 10th International Conference on Power Electronics and Drive Systems (PEDS)*, pp. 78-83.
[62] Industry Guide 2014, "'Inverter, Storage and PV System Technology," *[Online].Available :http://www.pv-system-tech.com/technology/storage-and-energy-management/*.
[63] B. Chen, J. Wang and J. Kim, "'Decentralized Energy Management System for Networked Microgrids in Grid-Connected and Islanded Modes," *IEEE Transactions on Smart Grid*, 2015, pp. 1-1.
[64] A.R. Malekpour and A. Pahwa, "'Radial Test Feeder including primary and secondary distribution network," *North American Power Symposium (NAPS), 2015*, pp. 1-9.
[65] A. Pahwa, S.A. DeLoach, B. Natarajan, S. Das, A.R. Malekpour, S.M. Shafiul Alam and D.M. Case, "'Goal-Based Holonic Multiagent System for Operation of Power Distribution Systems," *IEEE Transactions on Smart Grid*, vol. 6, no. 5, 2015, pp. 2510-2518.
[66] A.R. Malekpour, A. Pahwa and B. Natarajan, "'Distributed volt/var control in unbalanced distribution systems with distributed generation," *IEEE Symposium on Computational Intelligence Applications in Smart Grid*, 2015-January, pp. 1-6.
[67] A.R. Malekpour, A. Pahwa and B. Natarajan, "'Hierarchical Architecture for Integration of Rooftop PV in Smart Distribution Systems
," *IEEE Trans. Smart Grid*, (under revision).
[68] A.R. Malekpour and A. Pahwa, "'A Dynamic Operational Scheme for Residential PV Smart Inverters," *IEEE Trans. Smart Grid*, 2016.
[69] A. R. Malekpour, A. Pahwa, "'Stochastic Energy Management in Distribution Systems incorporating Multi-Microgrids and Correlated Wind Generators," *IEEE Trans. Power Syst.*, Under revision.
[70] T. Hubert and S. Grijalva, "'Realizing smart grid benefits requires energy optimization algorithms at residential level," *ISGT 2011*, pp. 1-8.
[71] H.M. Kim, M. Kokkolaras, L.S. Louca, G.J. Delagrammatikas, N.F. Michelena, Z.S. Filipi, P.Y. Papalambros, J.L. Stein and D.N. Assanis, "'Target cascading in vehicle redesign: A class VI truck study," *Int.J.Veh.Des.*, vol. 29, no. 3, 2002, pp. 199-225.
[72] R. Choudhary, A. Malkawi and P.Y. Papalambros, "'Analytic target cascading in simulation-based building design," *Autom.Constr.*, vol. 14, no. 4, 2005, pp. 551-568.

[73] J.J. Michalek, O. Ceryan, P.Y. Papalambros and Y. Koren, "'Balancing Marketing and Manufacturing Objectives in Product Line Design," *Journal of mechanical design*, vol. 128, no. 6, 2006, pp. 1196-1204.
[74] J.J. Michalek, F.M. Feinberg and P.Y. Papalambros, "'Linking marketing and engineering product design decisions via analytical target cascading," *J.Prod.Innovation Manage.*, vol. 22, no. 1, 2005, pp. 42-62.
[75] A.K. Marvasti, A. Kargarian Marvasti, S. Yong Fu, M. DorMohammadi and Rais-Rohani, "'Optimal Operation of Active Distribution Grids: A System of Systems Framework," *IEEE Transactions on Smart Grid*, vol. 5, no. 3, 2014, pp. 1228-1237.
[76] S. Tosserams, L.F.P. Etman, P.Y. Papalambros and J.E. Rooda, "'An augmented Lagrangian relaxation for analytical target cascading using the alternating direction method of multipliers," *Structural and multidisciplinary optimization*, vol. 31, no. 3, 2006, pp. 176-189.
[77] S. Tosserams, L.F.P. Etman and J.E. Rooda, "'Multi-modality in augmented Lagrangian coordination for distributed optimal design," *Struct.Mutltidiscip.Opt.*, vol. 40, no. 1-6, 2010, pp. 329-352.
[78] B.H. Kim and R. Baldick, "'Coarse-grained distributed optimal power flow," *IEEE Trans.Power Syst.*, vol. 12, no. 2, 1997, pp. 932-939.
[79] R.C. Dugan, M.F. McGranaghan and H.W. Beaty, "'Electrical power systems quality," *New York, NY: McGraw-Hill,| c1996*, vol. 1.
[80] A. Asadinejad and K. Tomsovic, "'Optimal use of incentive and price based demand response to reduce costs and price volatility," *Electr.Power Syst.Res.*, vol. 144, pp. 215-223.
[81] A. Asadinejad, K. Tomsovic and C. Chen, "'Sensitivity of incentive based demand response program to residential customer elasticity,", pp. 1-6.
[82] A. Asadinejad, M.G. Varzaneh, K. Tomsovic, C. Chen and R. Sawhney, "'Residential customers elasticity estimation and clustering based on their contribution at incentive based demand response,", pp. 1-5.
[83] A. Asadinejad and K. Tomsovic, "'Impact of Incentive Based Demand Response on large scale renewable integration,", pp. 1-5.
[84] C. Su, "'Stochastic Evaluation of Voltages in Distribution Networks With Distributed Generation Using Detailed Distribution Operation Models," *IEEE Trans.Power Syst.*, vol. 25, no. 2, 2010, pp. 786-795.

[85] Y. Li, Z. Lu and J.J. Michalek, "'Diagonal Quadratic Approximation for Parallelization of Analytical Target Cascading," *Journal of mechanical design*, vol. 130, no. 5, 2008, pp. 051402.
[86] N. Michelena, "'Convergence properties of analytical target cascading," *AIAA J.*, vol. 41, no. 5, 2003, pp. 897-905.
[87] D.P. Bertsekas, "'Nonlinear programming," *Athena scientific, 2nd edition*, 1999.
[88] S. Boyd and L. Vandenberghe, "Convex optimization,", Cambridge university press, 1st edition, 2004.
[89] A. Ruszczyński, "'On convergence of an augmented Lagrangian decomposition method for sparse convex optimization," *Mathematics of Operations Research*, vol. 20, no. 3, 1995, pp. 634-656.
[90] M. Lydia, A.I. Selvakumar, S.S. Kumar and G.E.P. Kumar, "'Advanced Algorithms for Wind Turbine Power Curve Modeling," *Sustainable Energy, IEEE Transactions on*, vol. 4, no. 3, 2013, pp. 827-835.
[91] Y. Tung and B. Yen, "'Hydrosystems engineering uncertainty analysis,".
[92] R.Y. Rubinstein and D.P. Kroese, "'Simulation and the Monte Carlo method,", 2016.
[93] A.S. Meliopoulos, G.J. Cokkinides and X.Y. Chao, "'A new probabilistic power flow analysis method," *IEEE Trans.Power Syst.*, vol. 5, no. 1, pp. 182-190.
[94] M.E. Harr, "'Probabilistic estimates for multivariate analyses," *Appl.Math.Model.*, vol. 13, no. 5, pp. 313-318.
[95] C.W. Tsai and S. Franceschini, "'Evaluation of probabilistic point estimate methods in uncertainty analysis for environmental engineering applications," *J.Environ.Eng.*, vol. 131, no. 3, pp. 387-395.
[96] P. Li, Z. Zhou and R. Shi, "'Probabilistic optimal operation management of microgrid using point estimate method and improved bat algorithm," *PES General Meeting | Conference & Exposition, 2014 IEEE*, pp. 1-5.
[97] X. Xu, T. Lin and X. Zha, "'Probabilistic analysis of small signal stability of microgrid using point estimate method," *Sustainable Power Generation and Supply, 2009. SUPERGEN '09. International Conference on*, pp. 1-6.
[98] T. Niknam, F. Golestaneh and A. Malekpour, "'Probabilistic energy and operation management of a microgrid containing wind/photovoltaic/fuel cell generation and energy storage devices based on point estimate method and self-adaptive gravitational search algorithm," *Energy*, vol. 43, no. 1, 2012, pp. 427-437.
[99] M.G. Kendall, "'The advanced theory of statistics.", 1946.

[100] W. Wangdee and R. Billinton, "'Considering load-carrying capability and wind speed correlation of WECS in generation adequacy assessment," *IEEE Trans.Energy Convers.*, vol. 21, no. 3, pp. 734-741.
[101] J.M. Morales, L. Baringo, A.J. Conejo and R. Minguez, "'Probabilistic power flow with correlated wind sources," *Generation, Transmission & Distribution, IET*, vol. 4, no. 5, 2010, pp. 641-651.
[102] M. Zugno, J.M. Morales, P. Pinson and H. Madsen, "'Pool strategy of a price-maker wind power producer," *IEEE Trans.Power Syst.*, vol. 28, no. 3, pp. 3440-3450.
[103] S. Xia, X. Luo, K.W. Chan, M. Zhou and G. Li, "'Probabilistic Transient Stability Constrained Optimal Power Flow for Power Systems With Multiple Correlated Uncertain Wind Generations," *IEEE Transactions on Sustainable Energy*, vol. 7, no. 3, pp. 1133-1144.
[104] M. Zare, T. Niknam, R. Azizipanah-Abarghooee and B. Amiri, "'Multi-objective probabilistic reactive power and voltage control with wind site correlations," *Energy*, vol. 66, pp. 810-822.
[105] P. Zhang and S.T. Lee, "'Probabilistic Load Flow Computation Using the Method of Combined Cumulants and Gram-Charlier Expansion," *IEEE Trans.Power Syst.*, vol. 19, no. 1, 2004, pp. 676-682.
[106] M.E. Baran and F.F. Wu, "'Network reconfiguration in distribution systems for loss reduction and load balancing," *IEEE Trans.Power Del.*, vol. 4, no. 2, 1989, pp. 1401-1407.
[107] A. Feijóo, D. Villanueva, J.L. Pazos and R. Sobolewski, "'Simulation of correlated wind speeds: A review," *Renewable & sustainable energy reviews*, vol. 15, no. 6, 2011, pp. 2826-2832.
[108] K. Zou, A.P. Agalgaonkar, K.M. Muttaqi and S. Perera, "'Distribution System Planning With Incorporating DG Reactive Capability and System Uncertainties," *IEEE Transactions on Sustainable Energy*, vol. 3, no. 1, 2012, pp. 112-123.

Appendix A - Developed Test Case Benchmark Data

Table A.1 lists load data of 42 homes. The data are extracted from eGauge website. Phases A, B, and C contains 144, 144, and 160 homes, respectively. Random selection is utilized in order to determine which home type is in which node (receiving node), as shown in Table A.2. Home type 0 indicates no home in that node.

Table A.1 Home type and web link to extract the load data.

Type	Link	Type		Type	Link
1	http://egauge297.egaug.es/	15	http://egauge380.egaug.es/	29	http://egauge676.egaug.es/
2	http://egauge300.egaug.es/	16	http://egauge397.egaug.es/	30	http://egauge705.egaug.es/
3	http://egauge230.egaug.es/	17	http://egauge500.egaug.es/	31	http://egauge56.egaug.es/
4	http://egauge303.egaug.es/	18	http://egauge502.egaug.es/	32	http://egauge46.egaug.es/
5	http://egauge305.egaug.es/	19	http://egauge505.egaug.es/	33	http://egauge38.egaug.es/
6	http://egauge312.egaug.es/	20	http://egauge556.egaug.es/	34	http://egauge61.egaug.es/
7	http://egauge343.egaug.es/	21	http://egauge602.egaug.es/	35	http://egauge62.egaug.es/
8	http://egauge339.egaug.es/	22	http://egauge608.egaug.es/	36	http://egauge73.egaug.es/
9	http://egauge346.egaug.es/	23	http://egauge612.egaug.es/	37	http://egauge169.egaug.es/
10	http://egauge348.egaug.es/	24	http://egauge616.egaug.es/	38	http://egauge89.egaug.es/
11	http://egauge354.egaug.es/	25	http://egauge628.egaug.es/	39	http://egauge117.egaug.es/
12	http://egauge360.egaug.es/	26	http://egauge651.egaug.es/	40	http://egauge104.egaug.es/
13	http://egauge361.egaug.es/	27	http://egauge662.egaug.es/	41	http://egauge141.egaug.es/
14	http://egauge363.egaug.es/	28	http://egauge665.egaug.es/	42	http://egauge142.egaug.es/

Test feeder line segment data are given in Table A.2. Admittance matrices for configurations types 721, 722, 723, and 724 are available in [9]. Configurations types 725, 726, and 727 correspond to feeder laterals, triplex overhead drop cable, and pole-mounted transformer, respectively.

Table A.2 Test feeder line segment and load type data.

From	To	Length (ft.)	Conductor Type	Home Type			From	To	Length (ft.)	Conductor Type	Home Type		
				Phase A	Phase B	Phase C					Phase A	Phase B	Phase C
1	2	1850	721	0	0	0	62	64	1	727	0	0	0
2	3	960	722	0	0	0	64	65	90	726	0	36	0
3	4	1320	722	0	0	0	64	66	90	726	0	6	0
4	5	240	724	0	0	0	64	67	90	726	0	9	0
5	6	280	723	0	0	0	64	68	90	726	0	31	0
6	7	200	724	0	0	0	63	69	1	727	0	0	0
6	8	280	724	0	0	0	69	70	90	726	0	22	0
4	9	600	723	0	0	0	69	71	90	726	0	40	0
9	10	200	723	0	0	0	69	72	90	726	0	30	0
10	11	320	723	0	0	0	69	73	90	726	0	10	0
11	12	320	724	0	0	0	32	74	125	725	0	0	0
11	13	320	723	0	0	0	74	75	250	725	0	0	0
13	14	560	723	0	0	0	75	76	250	725	0	0	0
14	15	520	724	0	0	0	76	77	250	725	0	0	0
15	16	200	724	0	0	0	74	78	1	727	0	0	0
15	17	1280	724	0	0	0	78	79	90	726	0	0	42
14	18	640	723	0	0	0	78	80	90	726	0	0	14
18	19	400	723	0	0	0	78	81	90	726	0	0	42
19	20	400	723	0	0	0	78	82	90	726	0	0	24
20	21	200	724	0	0	0	75	83	1	727	0	0	0
20	22	400	723	0	0	0	83	84	90	726	0	0	31
10	23	600	723	0	0	0	83	85	90	726	0	0	26
10	24	300	721	0	0	0	83	86	90	726	0	0	3
3	25	400	724	0	0	0	83	87	90	726	0	0	29
25	26	240	724	0	0	0	76	88	1	727	0	0	0
25	27	320	724	0	0	0	88	89	90	726	0	0	30
3	28	360	723	0	0	0	88	90	90	726	0	0	2
28	29	520	723	0	0	0	88	91	90	726	0	0	20
29	30	80	724	0	0	0	88	92	90	726	0	0	25
30	31	520	724	0	0	0	77	93	1	727	0	0	0
29	32	800	723	0	0	0	93	94	90	726	0	0	6
32	33	600	723	0	0	0	93	95	90	726	0	0	21
33	34	280	724	0	0	0	93	96	90	726	0	0	31
32	35	920	724	0	0	0	93	97	90	726	0	0	22
35	36	120	724	0	0	0	36	98	125	725	0	0	0
35	37	760	724	0	0	0	98	99	250	725	0	0	0
31	38	125	725	0	0	0	99	100	250	725	0	0	0
38	39	250	725	0	0	0	100	101	250	725	0	0	0
39	40	250	725	0	0	0	101	102	250	725	0	0	0
40	41	250	725	0	0	0	102	103	250	725	0	0	0
38	42	1	727	0	0	0	98	104	1	727	0	0	0
42	43	90	726	19	0	0	104	105	90	726	0	17	28
42	44	90	726	21	0	0	104	106	90	726	0	23	37
42	45	90	726	11	0	0	104	107	90	726	0	26	39
42	46	90	726	27	0	0	104	108	90	726	0	26	21
39	47	1	727	0	0	0	99	109	1	727	0	0	0
47	48	90	726	37	0	0	109	110	90	726	0	26	0
47	49	90	726	9	0	0	109	111	90	726	0	21	0
47	50	90	726	36	0	0	109	112	90	726	0	15	0
47	51	90	726	6	0	0	109	113	90	726	0	6	0
40	52	1	727	0	0	0	100	114	1	727	0	0	0
52	53	90	726	30	0	0	114	115	90	726	0	3	0
52	54	90	726	42	0	0	114	116	90	726	0	15	0
52	55	90	726	3	0	0	114	117	90	726	0	18	0
52	56	90	726	29	0	0	114	118	90	726	0	20	0
41	57	1	727	0	0	0	101	119	1	727	0	0	0
57	58	90	726	40	0	0	119	120	90	726	0	5	0
57	59	90	726	41	0	0	119	121	90	726	0	19	0
57	60	90	726	40	0	0	119	122	90	726	0	36	0
57	61	90	726	5	0	0	119	123	90	726	0	8	0
34	62	125	725	0	0	0	102	124	1	727	0	0	0
62	63	250	725	0	0	0	124	125	90	726	0	34	0

From	To	Length (ft.)	Conductor Type	Home Type			From	To	Length (ft.)	Conductor Type	Home Type		
				Phase A	Phase B	Phase C					Phase A	Phase B	Phase C
124	126	90	726	0	37	0	185	188	90	726	0	0	10
124	127	90	726	0	42	0	185	189	90	726	0	0	25
124	128	90	726	0	11	0	178	190	1	727	0	0	0
103	129	1	727	0	0	0	190	191	90	726	0	0	3
129	130	90	726	0	27	0	190	192	90	726	0	0	32
129	131	90	726	0	28	0	190	193	90	726	0	0	17
129	132	90	726	0	34	0	190	194	90	726	0	0	27
129	133	90	726	0	5	0	179	195	1	727	0	0	0
37	134	125	725	0	0	0	195	196	90	726	0	0	14
134	135	250	725	0	0	0	195	197	90	726	0	0	35
134	136	1	727	0	0	0	195	198	90	726	0	0	5
136	137	90	726	0	5	0	195	199	90	726	0	0	16
136	138	90	726	0	29	0	27	200	125	725	0	0	0
136	139	90	726	0	7	0	200	201	250	725	0	0	0
136	140	90	726	0	12	0	201	202	250	725	0	0	0
135	141	1	727	0	0	0	202	203	250	725	0	0	0
141	142	90	726	0	17	0	200	204	1	727	0	0	0
141	143	90	726	0	10	0	204	205	90	726	28	15	0
141	144	90	726	0	8	0	204	206	90	726	5	36	0
141	145	90	726	0	16	0	204	207	90	726	1	7	0
28	146	125	725	0	0	0	204	208	90	726	10	42	0
146	147	250	725	0	0	0	201	209	1	727	0	0	0
147	148	250	725	0	0	0	209	210	90	726	0	32	0
148	149	250	725	0	0	0	209	211	90	726	0	24	0
146	150	1	727	0	0	0	209	212	90	726	0	2	0
150	151	90	726	0	0	33	209	213	90	726	0	29	0
150	152	90	726	0	0	34	202	214	1	727	0	0	0
150	153	90	726	0	0	1	214	215	90	726	0	13	0
150	154	90	726	0	0	38	214	216	90	726	0	35	0
147	155	1	727	0	0	0	214	217	90	726	0	21	0
155	156	90	726	0	0	39	214	218	90	726	0	24	0
155	157	90	726	0	0	36	203	219	1	727	0	0	0
155	158	90	726	0	0	15	219	220	90	726	0	30	0
155	159	90	726	0	0	27	219	221	90	726	0	31	0
148	160	1	727	0	0	0	219	222	90	726	0	37	0
160	161	90	726	0	0	16	219	223	90	726	0	39	0
160	162	90	726	0	0	7	8	224	125	725	0	0	0
160	163	90	726	0	0	34	224	225	250	725	0	0	0
160	164	90	726	0	0	29	224	226	1	727	0	0	0
149	165	1	727	0	0	0	226	227	90	726	24	0	0
165	166	90	726	0	0	9	226	228	90	726	21	0	0
165	167	90	726	0	0	20	226	229	90	726	38	0	0
165	168	90	726	0	0	41	226	230	90	726	7	0	0
165	169	90	726	0	0	13	225	231	1	727	0	0	0
30	170	125	725	0	0	0	231	232	90	726	24	0	0
170	171	1	727	0	0	0	231	233	90	726	21	0	0
171	172	90	726	31	28	0	231	234	90	726	38	0	0
171	173	90	726	35	38	0	231	235	90	726	7	0	0
171	174	90	726	2	14	0	6	236	125	725	0	0	0
171	175	90	726	7	12	0	236	237	250	725	0	0	0
26	176	125	725	0	0	0	236	238	1	727	0	0	0
176	177	250	725	0	0	0	238	239	90	726	15	0	0
177	178	250	725	0	0	0	238	240	90	726	26	0	0
178	179	250	725	0	0	0	238	241	90	726	31	0	0
176	180	1	727	0	0	0	238	242	90	726	14	0	0
180	181	90	726	0	0	28	237	243	1	727	0	0	0
180	182	90	726	0	0	19	243	244	90	726	27	0	0
180	183	90	726	0	0	13	243	245	90	726	21	0	0
180	184	90	726	0	0	35	243	246	90	726	20	0	0
177	185	1	727	0	0	0	243	247	90	726	32	0	0
185	186	90	726	0	0	5	7	248	125	725	0	0	0
185	187	90	726	0	0	10	248	249	250	725	0	0	0

From	To	Length (ft.)	Conductor Type	Home Type			From	To	Length (ft.)	Conductor Type	Home Type		
				Phase A	Phase B	Phase C					Phase A	Phase B	Phase C
248	250	1	727	0	0	0	310	312	90	726	0	22	0
250	251	90	726	14	25	24	310	313	90	726	0	21	0
250	252	90	726	26	4	9	310	314	90	726	0	16	0
250	253	90	726	42	1	4	299	315	1	727	0	0	0
250	254	90	726	37	19	18	315	316	90	726	0	8	0
249	255	1	727	0	0	0	315	317	90	726	0	15	0
255	256	90	726	23	20	39	315	318	90	726	0	33	0
255	257	90	726	33	29	7	315	319	90	726	0	11	0
255	258	90	726	6	20	18	12	320	125	725	0	0	0
255	259	90	726	33	35	16	320	321	250	725	0	0	0
5	260	125	725	0	0	0	320	322	1	727	0	0	0
260	261	250	725	0	0	0	322	323	90	726	0	0	26
260	262	1	727	0	0	0	322	324	90	726	0	0	10
262	263	90	726	0	0	38	322	325	90	726	0	0	5
262	264	90	726	0	0	8	322	326	90	726	0	0	6
262	265	90	726	0	0	34	321	327	1	727	0	0	0
262	266	90	726	0	0	2	327	328	90	726	0	0	15
261	267	1	727	0	0	0	327	329	90	726	0	0	6
267	268	90	726	0	0	29	327	330	90	726	0	0	12
267	269	90	726	0	0	28	327	331	90	726	0	0	32
267	270	90	726	0	0	25	13	332	125	725	0	0	0
267	271	90	726	0	0	17	332	333	250	725	0	0	0
9	272	125	725	0	0	0	333	334	250	725	0	0	0
272	273	250	725	0	0	0	334	335	250	725	0	0	0
273	274	250	725	0	0	0	332	336	1	727	0	0	0
274	275	250	725	0	0	0	336	337	90	726	10	0	0
272	276	1	727	0	0	0	336	338	90	726	3	0	0
276	277	90	726	0	0	22	336	339	90	726	39	0	0
276	278	90	726	0	0	37	336	340	90	726	3	0	0
276	279	90	726	0	0	23	333	341	1	727	0	0	0
276	280	90	726	0	0	39	341	342	90	726	16	0	0
273	281	1	727	0	0	0	341	343	90	726	39	0	0
281	282	90	726	0	0	24	341	344	90	726	28	0	0
281	283	90	726	0	0	23	341	345	90	726	13	0	0
281	284	90	726	0	0	32	334	346	1	727	0	0	0
281	285	90	726	0	0	3	346	347	90	726	12	0	0
274	286	1	727	0	0	0	346	348	90	726	33	0	0
286	287	90	726	0	0	11	346	349	90	726	36	0	0
286	288	90	726	0	0	19	346	350	90	726	39	0	0
286	289	90	726	0	0	11	335	351	1	727	0	0	0
286	290	90	726	0	0	40	351	352	90	726	23	0	0
275	291	1	727	0	0	0	351	353	90	726	4	0	0
291	292	90	726	0	0	31	351	354	90	726	29	0	0
291	293	90	726	0	0	22	351	355	90	726	18	0	0
291	294	90	726	0	0	33	14	356	125	725	0	0	0
291	295	90	726	0	0	9	356	357	250	725	0	0	0
23	296	125	725	0	0	0	356	358	1	727	0	0	0
296	297	250	725	0	0	0	358	359	90	726	0	0	11
297	298	250	725	0	0	0	358	360	90	726	0	0	36
298	299	250	725	0	0	0	358	361	90	726	0	0	14
296	300	1	727	0	0	0	358	362	90	726	0	0	40
300	301	90	726	0	10	0	357	363	1	727	0	0	0
300	302	90	726	0	31	0	363	364	90	726	0	0	33
300	303	90	726	0	34	0	363	365	90	726	0	0	1
300	304	90	726	0	41	0	363	366	90	726	0	0	9
297	305	1	727	0	0	0	363	367	90	726	0	0	27
305	306	90	726	0	33	0	16	368	125	725	0	0	0
305	307	90	726	0	20	0	368	369	250	725	0	0	0
305	308	90	726	0	41	0	369	370	250	725	0	0	0
305	309	90	726	0	9	0	370	371	250	725	0	0	0
298	310	1	727	0	0	0	368	372	1	727	0	0	0
310	311	90	726	0	23	0	372	373	90	726	0	39	0

From	To	Length (ft.)	Conductor Type	Home Type			From	To	Length (ft.)	Conductor Type	Home Type		
				Phase A	Phase B	Phase C					Phase A	Phase B	Phase C
372	374	90	726	0	11	0	435	436	90	726	13	0	0
372	375	90	726	0	5	0	435	437	90	726	30	0	0
372	376	90	726	0	29	0	435	438	90	726	20	0	0
369	377	1	727	0	0	0	435	439	90	726	25	0	0
377	378	90	726	0	30	0	21	440	125	725	0	0	0
377	379	90	726	0	40	0	440	441	250	725	0	0	0
377	380	90	726	0	17	0	441	442	250	725	0	0	0
377	381	90	726	0	39	0	442	443	250	725	0	0	0
370	382	1	727	0	0	0	440	444	1	727	0	0	0
382	383	90	726	0	4	0	444	445	90	726	0	0	42
382	384	90	726	0	14	0	444	446	90	726	0	0	20
382	385	90	726	0	26	0	444	447	90	726	0	0	42
382	386	90	726	0	1	0	444	448	90	726	0	0	35
371	387	1	727	0	0	0	441	449	1	727	0	0	0
387	388	90	726	0	18	0	449	450	90	726	0	0	35
387	389	90	726	0	18	0	449	451	90	726	0	0	14
387	390	90	726	0	32	0	449	452	90	726	0	0	24
387	391	90	726	0	17	0	449	453	90	726	0	0	32
17	392	125	725	0	0	0	442	454	1	727	0	0	0
392	393	250	725	0	0	0	454	455	90	726	0	0	25
392	394	1	727	0	0	0	454	456	90	726	0	0	17
394	395	90	726	0	42	0	454	457	90	726	0	0	1
394	396	90	726	0	14	0	454	458	90	726	0	0	23
394	397	90	726	0	11	0	443	459	1	727	0	0	0
394	398	90	726	0	9	0	459	460	90	726	0	0	15
393	399	1	727	0	0	0	459	461	90	726	0	0	27
399	400	90	726	0	4	0	459	462	90	726	0	0	30
399	401	90	726	0	38	0	459	463	90	726	0	0	23
399	402	90	726	0	12	0	22	464	125	725	0	0	0
399	403	90	726	0	33	0	464	465	250	725	0	0	0
18	404	125	725	0	0	0	464	466	1	727	0	0	0
404	405	250	725	0	0	0	466	467	90	726	0	0	12
405	406	250	725	0	0	0	466	468	90	726	0	0	18
406	407	250	725	0	0	0	466	469	90	726	0	0	26
407	408	250	725	0	0	0	466	470	90	726	0	0	34
408	409	250	725	0	0	0	465	471	1	727	0	0	0
404	410	1	727	0	0	0	471	472	90	726	0	0	3
410	411	90	726	2	0	0	471	473	90	726	0	0	22
410	412	90	726	20	0	0	471	474	90	726	0	0	2
410	413	90	726	17	0	0	471	475	90	726	0	0	18
410	414	90	726	10	0	0	19	476	125	725	0	0	0
405	415	1	727	0	0	0	476	477	250	725	0	0	0
415	416	90	726	12	0	0	477	478	250	725	0	0	0
415	417	90	726	36	0	0	478	479	250	725	0	0	0
415	418	90	726	11	0	0	479	480	250	725	0	0	0
415	419	90	726	18	0	0	476	481	1	727	0	0	0
406	420	1	727	0	0	0	481	482	90	726	4	0	0
420	421	90	726	14	0	0	481	483	90	726	26	0	0
420	422	90	726	12	0	0	481	484	90	726	40	0	0
420	423	90	726	34	0	0	481	485	90	726	12	0	0
420	424	90	726	25	0	0	477	486	1	727	0	0	0
407	425	1	727	0	0	0	486	487	90	726	33	0	0
425	426	90	726	4	0	0	486	488	90	726	15	0	0
425	427	90	726	18	0	0	486	489	90	726	32	0	0
425	428	90	726	9	0	0	486	490	90	726	2	0	0
425	429	90	726	7	0	0	478	491	1	727	0	0	0
408	430	1	727	0	0	0	491	492	90	726	38	0	0
430	431	90	726	31	0	0	491	493	90	726	22	0	0
430	432	90	726	1	0	0	491	494	90	726	11	0	0
430	433	90	726	28	0	0	491	495	90	726	38	0	0
430	434	90	726	22	0	0	479	496	1	727	0	0	0
409	435	1	727	0	0	0	496	497	90	726	16	0	0

From	To	Length (ft.)	Conductor Type	Home Type		
				Phase A	Phase B	Phase C
496	498	90	726	13	0	0
496	499	90	726	35	0	0
496	500	90	726	19	0	0
480	501	1	727	0	0	0
501	502	90	726	39	0	0
501	503	90	726	17	0	0
501	504	90	726	7	0	0
501	505	90	726	11	0	0
2	506	125	725	0	0	0
506	507	250	725	0	0	0
507	508	250	725	0	0	0
508	509	250	725	0	0	0
506	510	1	727	0	0	0
510	511	90	726	32	32	21
510	512	90	726	6	37	13
510	513	90	726	9	13	19
510	514	90	726	30	10	7
507	515	1	727	0	0	0
515	516	90	726	24	16	21
515	517	90	726	28	33	4
515	518	90	726	36	39	15
515	519	90	726	29	41	16
508	520	1	727	0	0	0
520	521	90	726	21	35	41
520	522	90	726	19	42	1
520	523	90	726	25	3	36
520	524	90	726	37	38	40
509	525	1	727	0	0	0
525	526	90	726	37	3	30
525	527	90	726	8	22	38
525	528	90	726	38	24	33
525	529	90	726	35	8	13
24	530	125	725	0	0	0
530	531	250	725	0	0	0
531	532	250	725	0	0	0
532	533	250	725	0	0	0
533	534	250	725	0	0	0
530	535	1	727	0	0	0
535	536	90	726	14	19	20
535	537	90	726	1	16	12
535	538	90	726	32	21	11
535	539	90	726	24	37	7
531	540	1	727	0	0	0
540	541	90	726	25	40	41
540	542	90	726	15	25	2
540	543	90	726	34	41	26
540	544	90	726	41	38	28
532	545	1	727	0	0	0
545	546	90	726	15	18	36
545	547	90	726	27	13	4
545	548	90	726	34	23	10
545	549	90	726	31	6	8
533	550	1	727	0	0	0
550	551	90	726	23	23	5
550	552	90	726	17	9	19
550	553	90	726	8	25	6
550	554	90	726	10	27	8
534	555	1	727	0	0	0
555	556	90	726	3	3	30
555	557	90	726	20	13	17
555	558	90	726	1	7	37
555	559	90	726	23	34	37

Appendix B - Linearization, convexification, and impact of varying termination tolerance

B.1 Linearization of Quadratic Terms

The quadratic penalty term $\|\mathbf{t}_n - \mathbf{r}_n\|_2^2$ can be presented as

$$\|\mathbf{t}_n - \mathbf{r}_n\|_2^2 = \|\mathbf{t}_n \circ \mathbf{t}_n + \mathbf{r}_n \circ \mathbf{r}_n - 2(\mathbf{t}_n \circ \mathbf{r}_n)\|_1 \quad . \tag{B.1}$$

By applying first order Taylor expansion, linearization at the point $(\mathbf{t}_n^k, \mathbf{r}_n^k)$ gives

$$\begin{aligned} \mathbf{t}_n \circ \mathbf{r}_n &\cong \mathbf{t}_n^k \circ \mathbf{r}_n^k + \mathbf{r}_n^k \circ (\mathbf{t}_n - \mathbf{t}_n^k) + \mathbf{t}_n^k \circ (\mathbf{r}_n - \mathbf{r}_n^k) \\ &= \mathbf{r}_n^k \circ \mathbf{t}_n + \mathbf{t}_n^k \circ \mathbf{r}_n - \mathbf{t}_n^k \circ \mathbf{r}_n^k \quad . \end{aligned} \tag{B.2}$$

Combining (B.1) and (B.2),

$$\begin{aligned} \|\mathbf{t}_n - \mathbf{r}_n\|_2^2 &\cong \|\mathbf{t}_n \circ \mathbf{t}_n + \mathbf{r}_n \circ \mathbf{r}_n - 2(\mathbf{r}_n^k \circ \mathbf{t}_n + \mathbf{t}_n^k \circ \mathbf{r}_n - \mathbf{t}_n^k \circ \mathbf{r}_n^k)\|_1 \\ &= \|\mathbf{t}_n^k \circ \mathbf{t}_n^k + \mathbf{r}_n \circ \mathbf{r}_n - 2(\mathbf{t}_n^k \circ \mathbf{r}_n)\|_1 \; + \\ &\quad \|\mathbf{t}_n \circ \mathbf{t}_n + \mathbf{r}_n^k \circ \mathbf{r}_n^k - 2(\mathbf{t}_n \circ \mathbf{r}_n^k)\|_1 \; + \\ &\quad \|2(\mathbf{t}_n^k \circ \mathbf{r}_n^k) - \mathbf{t}_n^k \circ \mathbf{t}_n^k - \mathbf{r}_n^k \circ \mathbf{r}_n^k\|_1 \\ &= \|\mathbf{t}_n^k - \mathbf{r}_n\|_2^2 + \|\mathbf{t}_n - \mathbf{r}_n^k\|_2^2 + \|\mathbf{t}_n^k - \mathbf{r}_n^k\|_2^2 \end{aligned} \tag{B.3}$$

where the last term in (B.3) is constant with respect to the current iteration.

B.2 Convexification of Nonlinear Equality Constraints

In our formulation, equality constraints (5.2), (5.3) and (5.8)-(5.11) (power balance constraints) are highly nonlinear, thus making the optimization problem of DSO a nonconvex optimization problem. In order to achieve affine equality constraints, the method of first order approximation is applied.

Let (B.4) and (B.5) present the general form of (5.2), (5.3) and (5.8)-(5.11) as follows

$$P_i^G = \sum_j V_i V_j Y_{ij} \cos(\delta_i - \delta_j - \theta_{ij}) + P_i^L \tag{B.4}$$

$$Q_i^G = \sum_j V_i V_j Y_{ij} \sin(\delta_i - \delta_j - \theta_{ij}) + Q_i^L \quad . \tag{B.5}$$

Expressing (B.4) and (B.5) in the form of net power injections at node i yield

$$P_i = \sum_j V_i V_j Y_{ij} \cos(\delta_i - \delta_j - \theta_{ij})$$

$$P_i = P_i^G - P_i^L \tag{B.6}$$

$$Q_i = \sum_j V_i V_j Y_{ij} \sin(\delta_i - \delta_j - \theta_{ij})$$

$$Q_i = Q_i^G - Q_i^L \quad . \tag{B.7}$$

The first step in our reformulation is to find a feasible solution

$$\hat{\mathbf{x}}^0 = \begin{bmatrix} |V_1| \\ \theta_1 \\ |V_2| \\ \theta_2 \\ . \\ . \\ |V_{Nb}| \\ \theta_{Nb} \end{bmatrix} \tag{B.8}$$

where Nb is the total number of buses in the DSO optimization. To obtain a feasible solution interior point algorithm is applied on the original problem which gives a local optimal point. Next, affine approximation of nonlinear equality constraints is attained via Taylor series expansion. The first order Taylor series approximation of power flow equation can be expressed as

$$\hat{P}_i^G = P_i^G(\hat{\mathbf{x}}^0) + \mathbf{J}_i^P(\hat{\mathbf{x}}^0)(\hat{\mathbf{x}} - \hat{\mathbf{x}}^0) \tag{B.9}$$

$$\hat{Q}_i^G = Q_i^G(\hat{\mathbf{x}}^0) + \mathbf{J}_i^Q(\hat{\mathbf{x}}^0)(\hat{\mathbf{x}} - \hat{\mathbf{x}}^0) \tag{B.10}$$

where $\hat{\mathbf{x}} \in \boldsymbol{\Gamma}^0$; $\boldsymbol{\Gamma}^0$ is the trust region with radius ε around the feasible point $\hat{\mathbf{x}}^0$, defined as

$$\boldsymbol{\Gamma}^0 = \{\hat{\mathrm{x}} || \hat{\mathrm{x}} - \hat{\mathrm{x}}^0| \leq \varepsilon\} \quad . \tag{B.11}$$

$\mathbf{J}_i^P$ and $\mathbf{J}_i^Q$ are the Jacobian of power flow equation constraints (B.6) and (B.7) as follows

$$\mathbf{J}_i^P = \left[\frac{\partial P_i}{\partial |V_1|} \quad \frac{\partial P_i}{\partial \theta_1} \quad \cdots \quad \frac{\partial P_i}{\partial |V_{NB}|} \quad \frac{\partial P_i}{\partial \theta_{NB}}\right] \tag{B.12}$$

$$\mathbf{J}_i^Q = \left[\frac{\partial Q_i}{\partial |V_1|} \quad \frac{\partial Q_i}{\partial \theta_1} \quad \cdots \quad \frac{\partial Q_i}{\partial |V_{NB}|} \quad \frac{\partial Q_i}{\partial \theta_{NB}}\right] \quad . \tag{B. 13}$$

(B.9) and (B.10) correspond to the convex affine approximation form of the original nonlinear equations (B.4) and (B.5). Finally, the optimization problem of DSO is solved based on the basic feasible solution (B.8). The new solution is plugged in (B.9) and (B.10) to get a new instance of the optimization problem. The optimization problem of DSO is solved iteratively till the solution converges to an optimal point. In every iteration a new feasible solution is obtained which is better than the previous solution. Similar approach is applied to handle nonlinear equality constraints in the optimization problem of MG

B.3 Effect of Varying Termination Tolerance σ

In order to further quantify performance of the proposed approaches, the effect of varying termination tolerance σ on runtime and solution accuracy of the deterministic solution is measured. The experiments with $\sigma = 10^{-2}, 10^{-3}, 10^{-4}, 10^{-5}$ are illustrated. In particular, Figure B.1 (a) shows the CPU time required to solve the overall problem via sequential and parallel computation approaches for different values of parameter σ. The APE between the two methods is shown in Figure B.1 (b). It is clear that the parallel computation method performs better than the sequential computation method in terms of CPU time while maintaining acceptable solution accuracy.

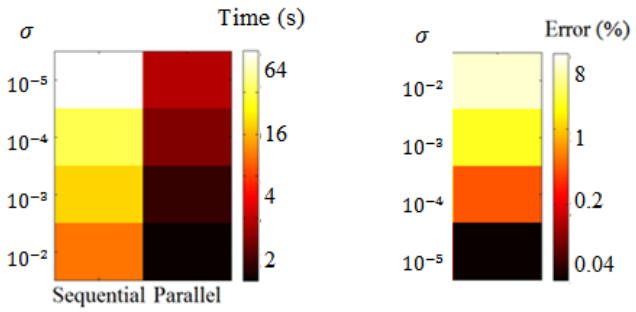

Figure B.1 (a) Required CPU time and (b) APE between sequential and parallel computation approaches